UNIVERSITY OF THE AEGEAN – DEPARTMENT OF GEOGRAPHY
ARISTOTLE UNIVERSITY OF THESSALONIKI – SCHOOL OF GEOLOGY
NATIONAL OBSERVATORY OF ATHENS

ATHANASIOS CHATZIIOANNOU
Geologist A.U.TH.

NEOTECTONIC SETTING AND FAULT MODELLING OF THE NORTHERN THESSALY 2021 EARTHQUAKE SEQUENCE

MASTER'S THESIS

MULTI-INSTITUTIONAL MASTER'S PROGRAM "NATURAL HAZARDS AND DISASTER MITIGATION"

MYTILENE
2023

ΠΑΝΕΠΙΣΤΗΜΙΟ ΑΙΓΑΙΟΥ – ΤΜΗΜΑ ΓΕΩΓΡΑΦΙΑΣ
ΑΡΙΣΤΟΤΕΛΕΙΟ ΠΑΝΕΠΙΣΤΗΜΙΟ ΘΕΣΣΑΛΟΝΙΚΗΣ – ΤΜΗΜΑ ΓΕΩΛΟΓΙΑΣ
ΕΘΝΙΚΟ ΑΣΤΕΡΟΣΚΟΠΕΙΟ ΑΘΗΝΩΝ

ΑΘΑΝΑΣΙΟΣ ΧΑΤΖΗΙΩΑΝΝΟΥ
Γεωλόγος Α.Π.Θ.

ΝΕΟΤΕΚΤΟΝΙΚΟ ΠΕΡΙΒΑΛΛΟΝ ΚΑΙ ΠΡΟΣΟΜΟΙΩΣΗ ΤΟΥ ΡΗΓΜΑΤΟΣ ΤΗΣ ΣΕΙΣΜΙΚΗΣ ΑΚΟΛΟΥΘΙΑΣ ΤΗΣ ΒΟΡΕΙΑΣ ΘΕΣΣΑΛΙΑΣ ΤΟΥ 2021

ΜΕΤΑΠΤΥΧΙΑΚΗ ΔΙΠΛΩΜΑΤΙΚΗ ΕΡΓΑΣΙΑ

ΔΙ-ΙΔΡΥΜΑΤΙΚΟ ΠΡΟΓΡΑΜΜΑ ΜΕΤΑΠΤΥΧΙΑΚΩΝ ΣΠΟΥΔΩΝ 'ΦΥΣΙΚΟΙ ΚΙΝΔΥΝΟΙ ΚΑΙ ΑΝΤΙΜΕΤΩΠΙΣΗ ΚΑΤΑΣΤΡΟΦΩΝ'

ΜΥΤΙΛΗΝΗ
2023

ATHANASIOS CHATZIIOANNOU
GEOLOGIST A.U.TH.

NEOTECTONIC SETTING AND FAULT MODELLING OF THE NORTHERN THESSALY 2021 EARTHQUAKE SEQUENCE

Submitted to the Department of Geography for the MSc Program "Natural Hazards and Disaster Mitigation"

Date of Oral Examination: 20/02/2023

Advisory Committee

Alexandros Chatzipetros, Associate Professor in the School of Geology, A.U.TH. (Supervisor)
Spyros Pavlides, Professor Emeritus in the School of Geology, A.U.TH.
Adamantios Kilias, Professor Emeritus in the School of Geology, A.U.TH.

Neotectonic setting and fault modelling of the Northern Thessaly 2021 earthquake sequence – *Master's Thesis*

Citation:
Chatziioannou A., 2023. – Neotectonic setting and fault modelling of the Northern Thessaly 2021 earthquake sequence. Master's Thesis, Department of Geography, University of the Aegean, 72pp.

Abstract

The Northern Thessaly 2021 earthquake sequence changed the way we see hidden or blind faults. It occurred in Central Greece with three mainshocks of M_w6.3, M_w6.0 and M_w5.6 on 3, 4 and 12 March, respectively. Serious damages were recorded and one indirect death in the villages of the area. The importance of the sequence is due to the highlighting of several features of the broader area's geological and tectonic environment.

This thesis is focused on the modelling of the Zarkos Fault Zone which is a hidden fault that was activated during the Northern Thessaly 2021 earthquake sequence. According to the InSAR images, it is situated in the mountainous area of Zarkos Mountains inside the Pelagonian nappe's Triassic–Jurassic recrystallized carbonates and alternations of Paleozoic gneisses and schists that bear evidence of Alpine deformation. Surfaces of the Zarkos Fault Zone are associated with the Pliocene-Early Pleistocene NE-SW trending extension, while today's active N-S extension has formed the E-W trending normal active faults of the broader area. At the hanging wall, it is maintained by the narrow graben-valley of Titarisios River that is filled with Neogene-Quartenary deposits.

According to our 3D modelling, the Zarkos Fault Zone comprises 4 synthetic fault surfaces of 33.5km total length and ~13km maximum depth, with an average dip of ~55^o towards NE, while the dip of the major surface is at 50^o. Our model results from the combination of the earthquake focuses or hypocentres of Kassaras et al. (2022) relocated catalogue and a detailed 2D mapping. For the mapping, we utilize the available InSAR images along with geological and geomorphological data.

The bidirectional propagation of the earthquake sequence begins with the two mainshocks on the major surface of the Zarkos Fault Zone, while three more synthetic surfaces are activated at its NW and SE tips. A projection of the hypocentres on the average rectangular best-fit plane is used for the detailed analysis of their spatiotemporal evolution and their correlation with our 3D model surfaces.

Examining our 3D model of the Zarkos Fault Zone and correlating it with previous models and suggestions indicates a general agreement, especially with those that are based on the same relocated catalogue, while it supports the theory of the activation of a hidden or blind low-angle fault. The main argument that remains is the dip direction of the surface associated with the 3rd mainshock occurrence on 12 March (M_w5.6), which is demonstrated as antithetic in other works.

Despite the complexity and short-timescale interactions between the multiple fault surfaces of the Zarkos Fault Zone, the Northern Thessaly 2021 earthquake sequence highlights the significant role of the structures inherited from previous deformational phases that are considered inactive. Fault growth is a continuous process resulting in fault zones that may be composed of surfaces originating from several stages of deformation and capable of giving strong earthquakes. A better understanding of these systems that

may be blind, hidden or unmapped is crucial for future seismic hazard assessment studies.

Acknowledgements

The stimulus for this research was my participation in the post-earthquake field survey for the Northern Thessaly 2021 earthquake sequence with the “Earthquake Geology Research Team” of the Aristotle University of Thessaloniki. Thus, I would like to express my deep gratitude to the head of the team, Prof. Alexandros Chatzipetros, Associate Professor in the School of Geology of the Aristotle University of Thessaloniki, for giving me plenty of opportunities like this and for being so supportive and encouraging as my supervisor all this time.

I also want to thank the Professors Emeritus of the School of Geology of the Aristotle University of Thessaloniki, Prof. Spyros Pavlides and Prof. Adamantios Kilias, for participating in my advisory committee and for sharing their knowledge and experience with the younger geologists at every opportunity.

An extremely important step for this research was my Erasmus+ Traineeship at the University College Dublin where I experienced different cultures and new approaches to research, work, and teaching. First of all, I would like to express my gratitude to Prof. John Walsh, for supervising my project and for honouring me with his friendship. Moreover, I would like to thank Dr Stratos Delogkos and Dr Vincent Roche who spent so many hours guiding me and chatting over my work. I am also very grateful to all the amazing people of the Fault Analysis Group and the School of Earth Sciences for their support and the good times we had.

I would like to thank the Erasmus+ program that funded my traineeship, which turned out to be so crucial for my research.

Furthermore, I am deeply indebted to the professors and students at the School of Geology of the Aristotle University of Thessaloniki for their important assistance and advice. For their assistance in the field, I would like to thank the PhD (c) Antriani Varnava and the graduate geologists Lila Vaitsi, Dimitra Perperi, Eirini Mantzoni and Konstantinos Savvidis.

Last but not least, I would like to express my very profound gratitude to my mother Amalia, my family, and my friends for providing me with continuous support and encouragement throughout my years of study and through the process of researching and writing this thesis. Finishing this thesis would be impossible without the support of Mary, whom I deeply thank.

CONTENTS

LIST OF FIGURES

1. INTRODUCTION

Earthquakes have played an important role in the study of the earth system, with continuous technological improvements providing outstanding opportunities for further examination. Morphogenic earthquakes (M>5.5) are those that leave a footprint on the surface of the earth since they are associated with co-seismic surface deformation associated with the seismic source (Pavlides & Caputo, 2004). The study of these earthquakes contributes, inter alia, to the advance of knowledge around the active faults' geometry and their interaction with crustal strain, which is a core component of risk management.

For human society, earthquakes pose a serious threat and therefore are considered natural hazards. Their uncontrollable nature compels society to focus on mitigating their disastrous impact. The field of disaster mitigation comprises multiple practices and scientific fields that work together to reduce society's vulnerability and develop its emergency response. The role of the geoscientist is associated with the risk management process and the increase of society's awareness.

1.1 Project Rationale

3D geomodelling is the most efficient way to analyze and describe complex geological environments and has several industrial applications. Earthquake data in geomodelling may reveal tectonic structures that could only be identified with geophysical methods. A better understanding of an area's tectonic setting is important not only for science but for the industry too, since economically interesting areas may be indicated, such as ore and mineral deposits.

In the case of Northern Thessaly, an earthquake sequence that occurred in March 2021 led to extensive post-event research in the area. It comprised a morphogenic doublet of M_w6.3 and M_w6.0 that was closely monitored by the sentinel-1 satellites and the Greek seismological network. The disaster struck a rural area causing one indirect death and severe damage to hundreds of buildings, mostly old stone-masonry structures built on sedimentary deposits. Nevertheless, it was a demonstration of the effectiveness of the current Greek seismic code (EAK-2000) and the state's disaster management planning.

The 2021 earthquake sequence brought the neotectonic setting of the area into focus, adding new information to the existing knowledge from previous studies. One of its major significances lies in the characteristics of the seismic source, which is associated with a hidden active fault differentiating from the typical active faults of the broader area. Active normal faults in Greece mostly appear at the margins of tectonic basins with rather steep slopes and are covered with sediments, at least on their hanging wall.

Furthermore, the seismic fault's trend is associated with a previous extensional phase (NE-SW), which is different from the active one (N-S). This fact highlights the complexity not only of the area's tectonics but also of the fault system's development.

Therefore, these may lead to a reconsideration of the active faults' characterization in general, adding more parameters to earthquake risk management.

This study examines the geometry of the Zarkos Fault Zone, the seismic source of the 2021 earthquake sequence, utilizing geodetic and seismic data in 2D and 3D environments. It aims to propose a legitimate fault model underpinned by its geological rationality and according to fault geometry and crustal deformation principles. The relationship of the model with the active tectonics of the broader epicentral area is also examined.

1.2 Thesis Outline

The contents of chapters 2-8 are outlined individually below:

Chapter 2. Geological setting: This chapter describes the geological features of the broader study area (Elassona Basin) and the Alpine tectonic evolution of the Zarkos mountains' bedrock where the Zarkos Fault Zone is situated.

Chapter 3. Seismotectonics: In this chapter, general information is displayed about the study area's lithostratigraphy and active tectonic setting, along with a brief description of its seismic history, while it introduces the Northern Thessaly 2021 earthquake sequence.

Chapter 4. Terminology, Data and Methodology: This chapter comprises the basic theoretical terms used in the thesis, along with a brief description of the data and methodology utilized for the construction of the 2D mapping and 3D modelling.

Chapter 5. 2D mapping of the Active Fault Traces: This chapter describes the procedures that were followed and the results of the 2D mapping of the area of interest that is based on the SAR interferometry images combined with the area's geology and geomorphology.

Chapter 6. 3D modelling of the Active Fault Surfaces: This chapter describes the procedures that were followed and the results of the 3D modelling based on the 2D mapping, along with a detailed analysis of the earthquake sequence's propagation on the 3D model.

Chapter 7. Discussion: In this chapter, the interpretation of this thesis about the Zarkos Fault Zone model is discussed in terms of comparison with other published works and correlation with the theoretical principles it should follow.

Chapter 8. Conclusions: This chapter summarises the main conclusions of all the previous chapters and itemizes the crucial views and interpretations that are discussed in this thesis.

2. GEOLOGICAL SETTING

2.1 Alpine Geology

The 2021 earthquake sequence epicentral area is entirely within the Pelagonian zone, according to the geotectonic division of Greece (Figure 2.1). The oldest formation is the crystalline bedrock of Paleozoic age which comprises gneisses, gneiss-schists, amphibolitic schists and quarzites. Granitoid masses intrude sparsely into the bedrock formations in Upper Carboniferous. At the western margin, a Permo-triassic volcano-sedimentary sequence consisting of low metamorphic grade rocks (marbles, phyllites, and sandstones) and intercalated bimodal volcanic products (mafic, intermediate, and felsic rocks), overlies the Pelagonian bedrock and passes into a carbonate cover of Triassic-Jurassic age. Within the study area, a carbonate cover is observed and is divided into the autochthonous "Kranea unit" and a same age's neritic, overthrusting nappe above that (Kilias et al., 1991, 2013; Mountrakis, 1986).

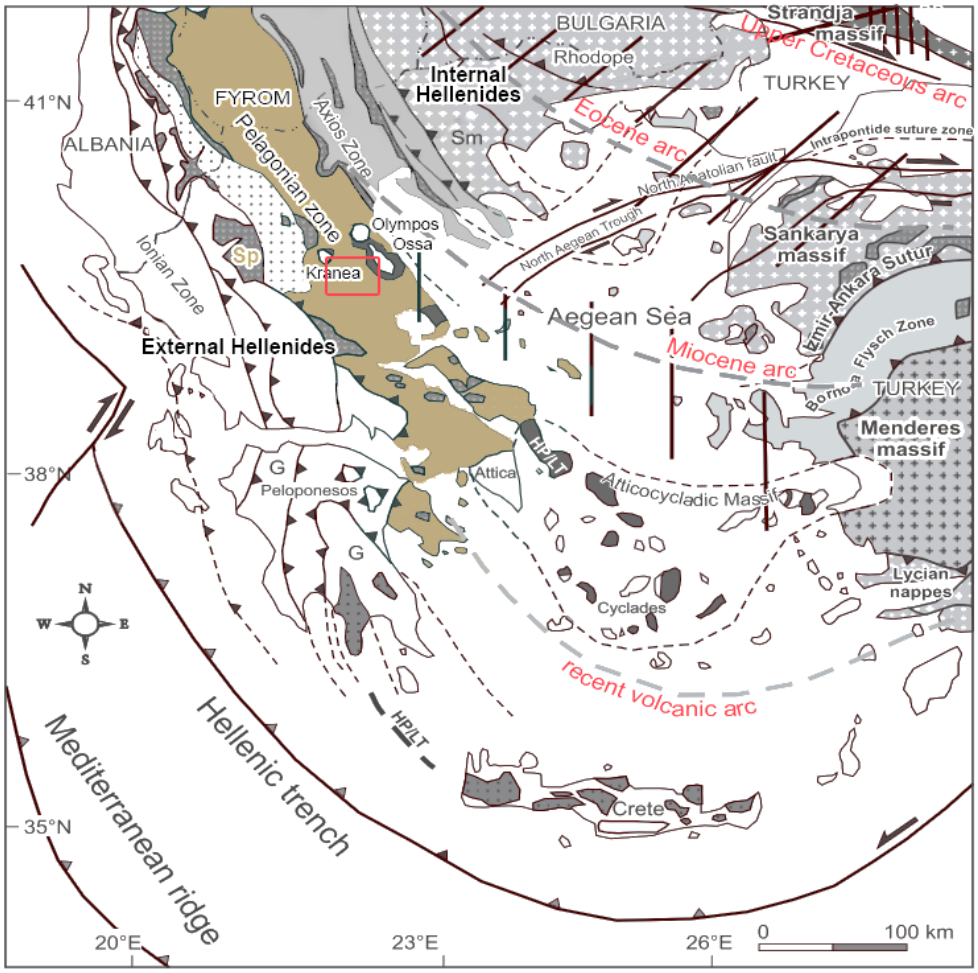

Figure 2.1 *Schematic geotectonic map of the Hellenides with the main structural domains and their continuation to the adjacent orogenic belts. The red rectangle corresponds to the study area (after Kilias et al., 2013).*

2.2 Post-alpine formations

In the area's geological structure there are sedimentary formations associated with the post-Alpine orogen stages overlying unconformably the Pelagonian crystalline bedrock. The older formations are Oligoce-Miocene age molassic formations (sands, clays, marls, sandstones and conglomerates) of the Meso-Hellenic Trough, mainly deposited around Pinios river. Above them, there are Neogene formations that consist of clays, silts, marls, sands, sandstones, conglomerates, breccias, grits and marly limestones, indicating lagoonal or shallow marine environment. The younger formations are a thick layer of Quaternary age sediments (alluvial deposits and fans, littoral deposits, screes and fluvial terraces) associated with a lacustrine to fluvial environment transition (Psilovikos et al., 1989; Caputo et al., 1994; Migiros et al., 2011).

2.3 Tectonic Evolution

The Pelagonian crystalline bedrock bears evidence of multiple deformational episodes considered to accompany metamorphism. Prior to the Alpine orogeny, a compressional event D_1 affects the broader area of study, creating an S_1 schistosity observed in the bedrock (Figure 2.2). It is associated with the Pelagonian overthrust towards SW onto the "Kranea unit" that is subsequently exhumated as a tectonic window. The exhumation takes place during the last stages of the D_1 period, characterized by extensional mylonitic shear zones (D_{SB}) and low-angle faults striking NW-SE.

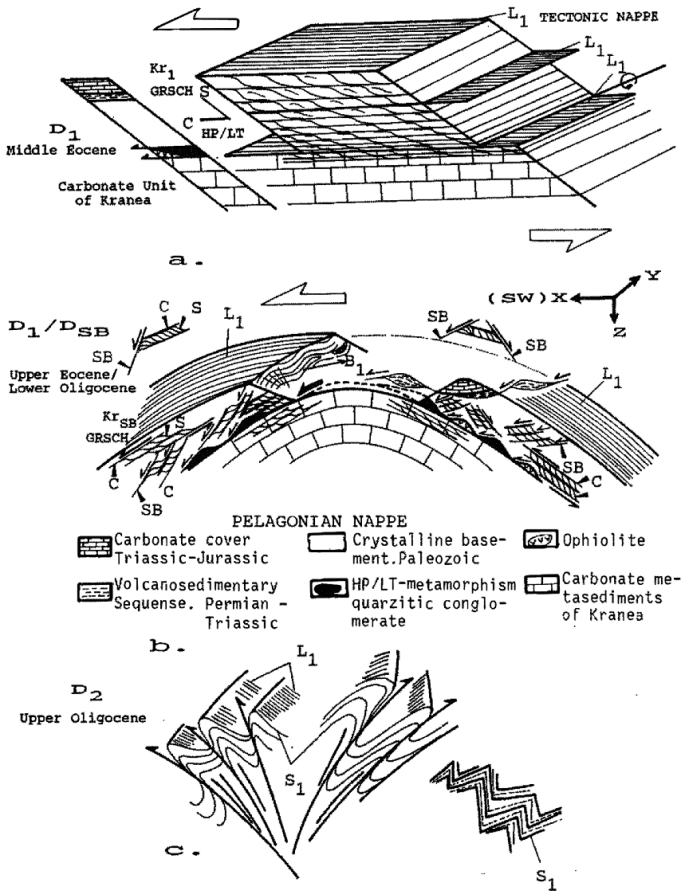

The evolution of the Alpine orogen affected the rock formations of the area in two stages. A compressional event (D2) associated with low-grade metamorphism occurred in Early Cretaceous is responsible for knick folds, shear zones, and thrust

Figure 2.2 *Schematic illustration of the evolutionary stages for the Tertiary deformation in the broader studied region (Kranea area). a) D1 compression and SW-wards nappe stacking, including the HP/LT metamorphic rocks, b) subsequent extension and crustal uplift; kinematic indicators show also a main SW-ward sense of movement during nappe denudation, c) younger D2 compression, conjugate knick folds and SW- or NW-ward directed thrust faults formation (after Kilias et al., 1991).*

faults. The third deformational event (D_3) is extensional and takes place in Early Tertiary developing mylonitic foliation (S_3) along with SW-NE stretching lineation on the rocks of Kranea region (Caputo & Pavlides, 1991; Kilias et al., 1991; Sfeikos et al., 1990).

3. SEISMOTECTONICS

The area of Thessaly is part of the broader back-arc area of the Hellenic arc, in the immediate vicinity of the North Aegean Trough. It is maintained by an almost N-S extensional stress field with low strain rates compared to the surrounding areas (Goldsworthy et al., 2002; Floyd et al., 2010; Pérouse et al., 2012; Sboras et al., 2017; Ferentinos et al., 2018). According to recent detailed analyses on the area's crustal deformation based on GPS geodetic measurements (Lazos et al., 2021), there seems to be a NW-SE oriented strip of crustal dilatation transitioning to compaction towards the western margin, as shown in Figure 3.1.

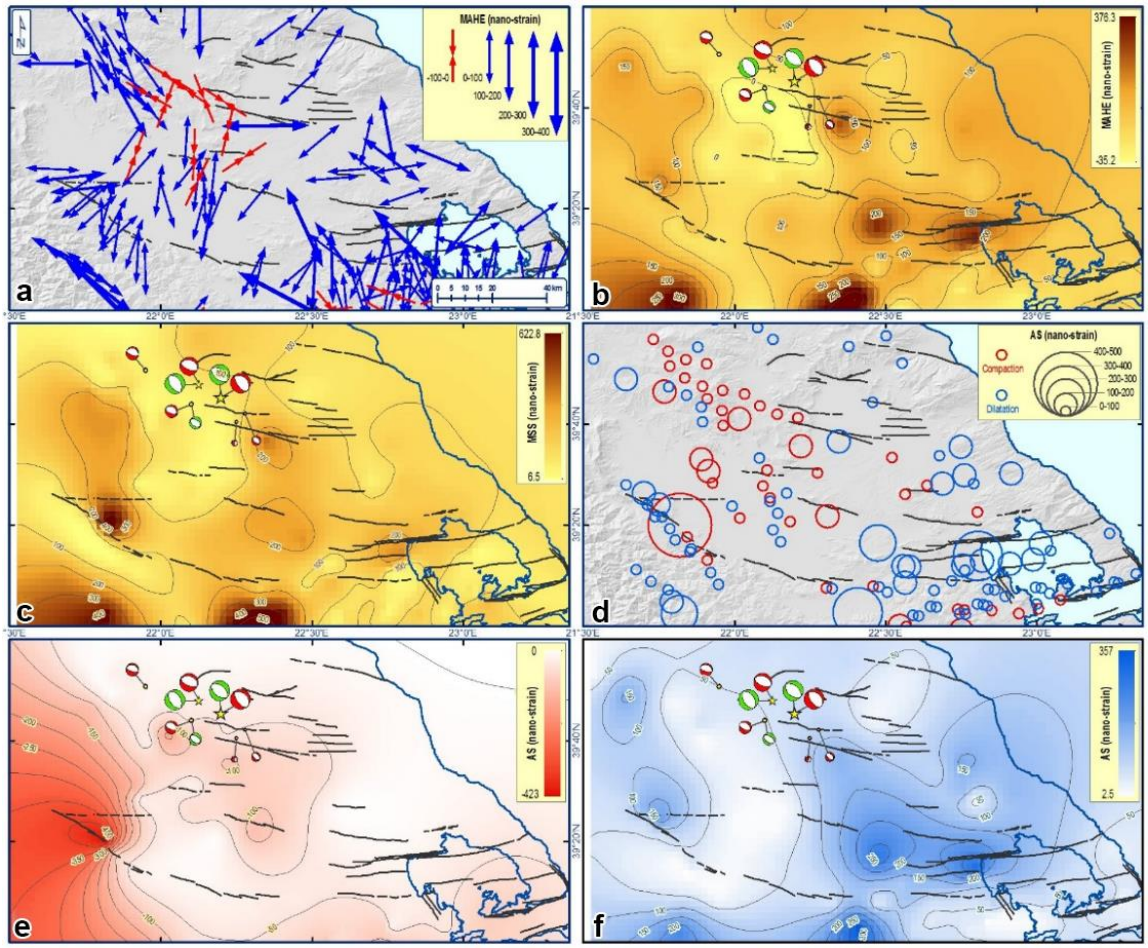

Figure 3.1 *(a, b) Maximum Horizontal Extension (MAHE) on barycentres as vectors (a) and interpolated (b). (c) Maximum Shear Strain (MSS) interpolated. (d, e, f) Area Strain (AS) on barycentres as circles (d) and dilatation and compaction interpolated (e and f, respectively). The used interpolation method is Kriging. The major neotectonic/active faults and the moment tensor solutions (IG-NOA and GFZ) of the 2021 seismic sequence are also shown (after Lazos et al., 2021).*

3.1 Neotectonic setting

The geodynamics of the Eastern Mediterranean region is under the influence of the African slab's southward retreat that led to back-arc extension and the collapse of the Hellenic orogen since the Late Miocene (Jolivet & Brun, 2010; Mercier et al., 1989; Wortel & Spakman, 2000). The slab's retreat and tearing are responsible for the complex neotectonic setting of the broader area along with a significant variation of the moho depth spatial distribution (Makris et al., 2013; Roche et al., 2019).

In the area of Thessaly (Central Greece), where the depth of Moho discontinuity is approximately around 35km (C. Papazachos, 1993; Makris et al., 2013), the neotectonic setting is characterized by the gradual development of fault systems along with a counterclockwise rotation of the extensional field's trend due to the migration of the orogen towards the external zones to the West. In the early post-orogenic phase during Late Miocene, it is dominated by a NE-SW extensional trend corresponding to the NW-SE trending normal faults and lignite-bearing basins in the broader area of Thessaly and Western Macedonia.

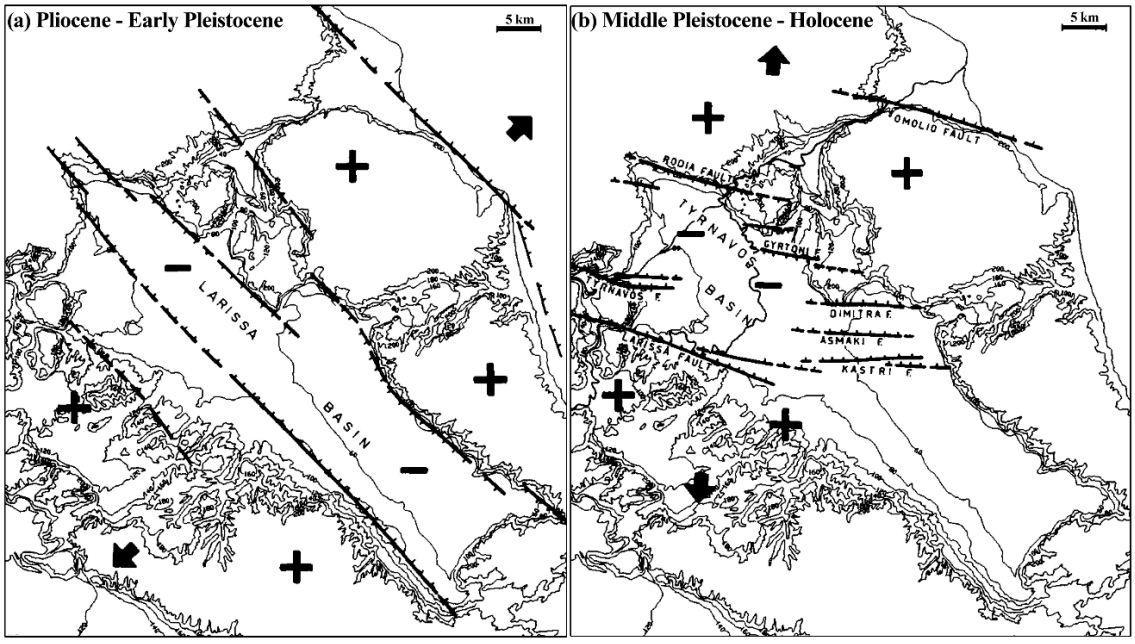

Figure 3.2 *Schematic maps explaining the latest two extensional phases, (a) during Pliocene-Early Pleistocene and (b) Middle Pleistocene-Holocene. Positive and negative signs indicate uplift and subsidence respectively. (Sboras et al. 2022, after Caputo et al. 1994).*

The latest extensional stages resulted in the final shape of the area's sedimentary basins are explained through the example of Larissa Basin, as shown in Figure 3.2. In Middle Pleistocene, the extension in the Aegean area shifts to today's N-S direction due to the influence of the slab roll-back processes and leads to the development of W-E trending fault surfaces (Mercier et al., 1989; Caputo & Pavlides, 1991, 1993; Caputo et al., 1994; Walcott, 1998).

The most developed structures in the broader study area are the sub-parallel striking Tyrnavos and Larisa active faults. They comprise NW-SE trending segments

following the geometry of Titarissios graben-valley and WNW-ESE to W-E as they enter the greater Larissa plain, where their exposed outcrop is buried under sediments. Both of them reach the Alpine bedrock maintaining a general dip towards NE (Caputo et al., 2003, 2004). Further details about them can be found in the Greek Database of Seismogenic Sources - GreDaSS (Caputo et al., 2012).

In addition, the extensional stress regime is responsible for the formation and evolution of multiple tectonic basins in Western Macedonia and Thessaly during the Neogene period. As shown in the map of Figure 3.3, the spatial and morphological relationship of the basins supports their isochronous development. Within the study area, three major basins can be found maintaining a general NW-SE trend bounded by the normal faults. The largest of them is the Larissa plain, associated with the activity of the Larissa and Tyrnavos faults. Along with the Karditsa Plain in the Southwestern part, they are the remains of Quaternary lakes that dried up due to variations of the morphology and watershed (Caputo et al., 2021).

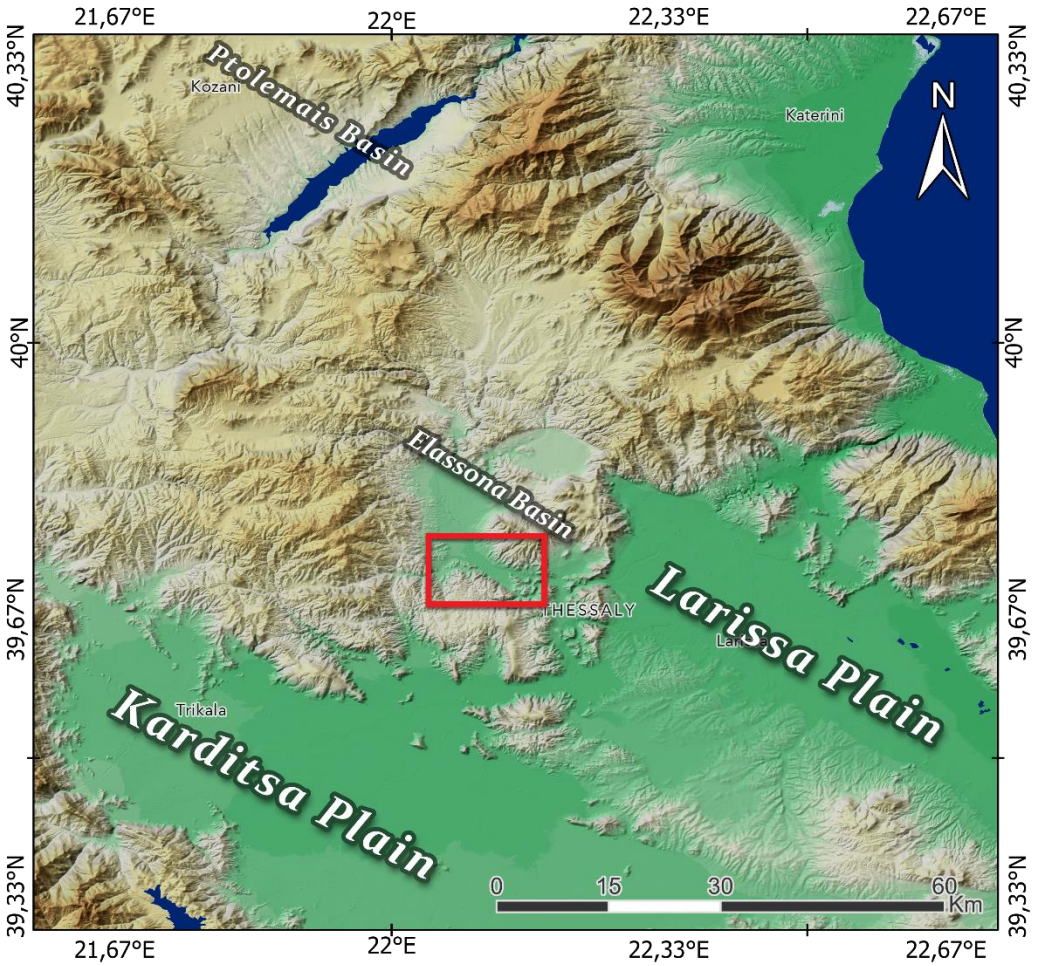

Figure 3.3 *Morphological map of the broader area of Thessaly and Western Macedonia with highlighted the main sedimentary basins. The red rectangle indicates the 2021 epicentral area which is studied in this thesis.*

The third basin and essential for this study is the lignite-bearing Elassona basin which is fully isolated by hill ridges. It is partially formed on the remnants of the Meso-Hellenic Trough system formed in the last stages of the Alpine orogen (Kilias et al., 2017; Vamvaka, 2015). At its Southern part, the Domeniko-Amouri sub-basin, it becomes narrower and connects with Larissa Plain through Titarissios graben-valley. The lignite-bearing sub-basin of Domeniko-Amouri is in the 2021 epicentral area's vicinity.

3.2 Study area's stratigraphy

Since Upper Miocene, the Elassona basin is receiving continuous sedimentation through a possibly low-energy stream network that deposits material on the eroded Alpine bedrock formations. An elaborate description of the stratigraphy provided by IGME due to lignite exploration research in the area is reproduced below (Dimitriou, D.; Giakoupis, 1998). According to the stratigraphic column of Figure 3.4, two basin-wide lithostratigraphic groups can be recognized above the Pelagonian crystalline bedrock:

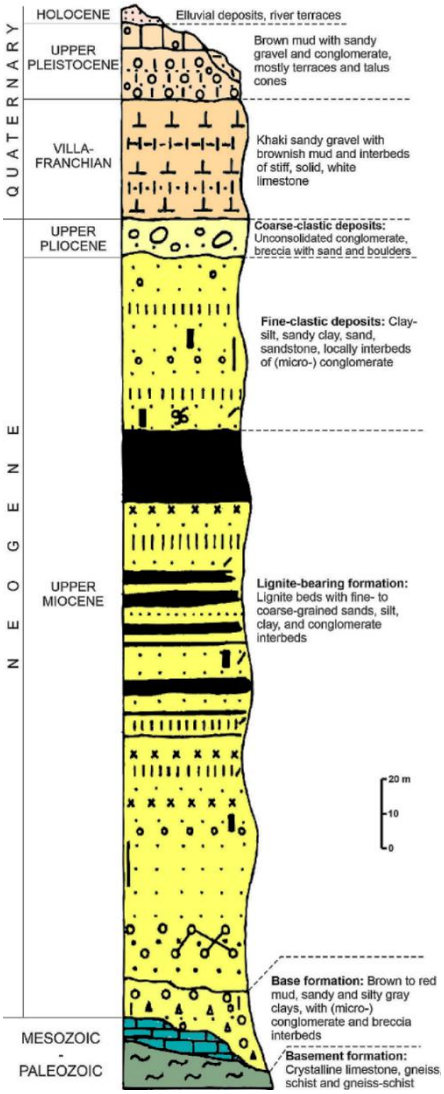

- The lower group is approximately 280 m thick, overlying the crystalline bedrock uncomfortably and consists of 4 stratigraphic formations of Upper Miocene age: 1) A Base formation of alluvial fan deposits (clays, conglomerate and breccia), 2) A grey-green lignite bearing formation that consists of clayey silts, sandy clays, sands, clays, and rarely silts, 3) Clastic deposits of friable siltstones, sandy clays, sands, with local intercalations of conglomerates, and 4) Coarse-clastic deposits of unconsolidated to loose breccia-conglomerate with sands and boulders.
- The upper group is formed during Quartenary and has an approximate thickness of 140m. It corresponds to a variating deposit of brown-khaki gravels and conglomerates intercalated with white limestones. At its upper part, it passes to a thin Holocene age layer of river terrace deposits (IGME, 1987, 1998; Dimitriou, D.; Giakoupis, 1998).

Figure 3.4 *Synthetic stratigraphic column of the Neogene formations of the Elassona Basin, according to the study of IGME (Dimitriou, D.; Giakoupis, 1998; Galanakis et al., 2021).*

3.3 Seismicity of Northern Thessaly

The seismic record of the broader area of Thessaly is rather rich and has begun since antiquity with several references that have survived through time. Moreover, palaeoseismological studies on the area's major faults have revealed all the times that they were activated with a rather high accuracy. As a result, seismic catalogues for historical events are available and therefore can be combined with the instrumental data providing a comprehensive overview of the area's seismicity, as shown in the map of Figure 3.5. The event's colours that appear on the map correspond to the historical events, the instrumental period, and the 2021 earthquake sequence. The modern instrumental period (blue circles in the map) begins in 1965, and since 2008 it maintains a higher accuracy than before due to upgrades on the seismological network.

As derived from the seismicity map of Figure 3.5, which is composed of historical and modern earthquake catalogues (Papazachos & Papazachou, 2003; Caputo et al., 2006; Stucchi et al., 2013; Kassaras et al., 2022; IG-NOA, n.d.), the medium and strong events that are located in the Northern Thessaly area, are mainly before the 20th century. The last reported major event in the Elassona basin occurred in 1901, inducing damages to Verdikoussa village and felt on Corfu island, according to Papaioannou (2021). Therefore, considering the rich historical record and the high recurrence times of the broader areas' faults, ranging from 140 up to 2,500 years according to literature (Pavlides & Caputo, 2004; Chatzipetros et al., 2021; Kourouklas et al., 2021), it is clear that the seismic hazard is extremely high.

The seismic gap of Northern Thessaly is confirmed by Caputo (1995), who compares the neotectonic setting's homogeneity with the seismic record's diversity in Central Greece. The area is dominated by Holocene age faults both in the Northern and Southern sectors, in contrast with the recorded seismicity which is focused on the Southern part. This gap seems to be filled geospatially by the 2021 Northern Thessaly earthquake sequence, as shown in the seismicity map in Figure 3.5.

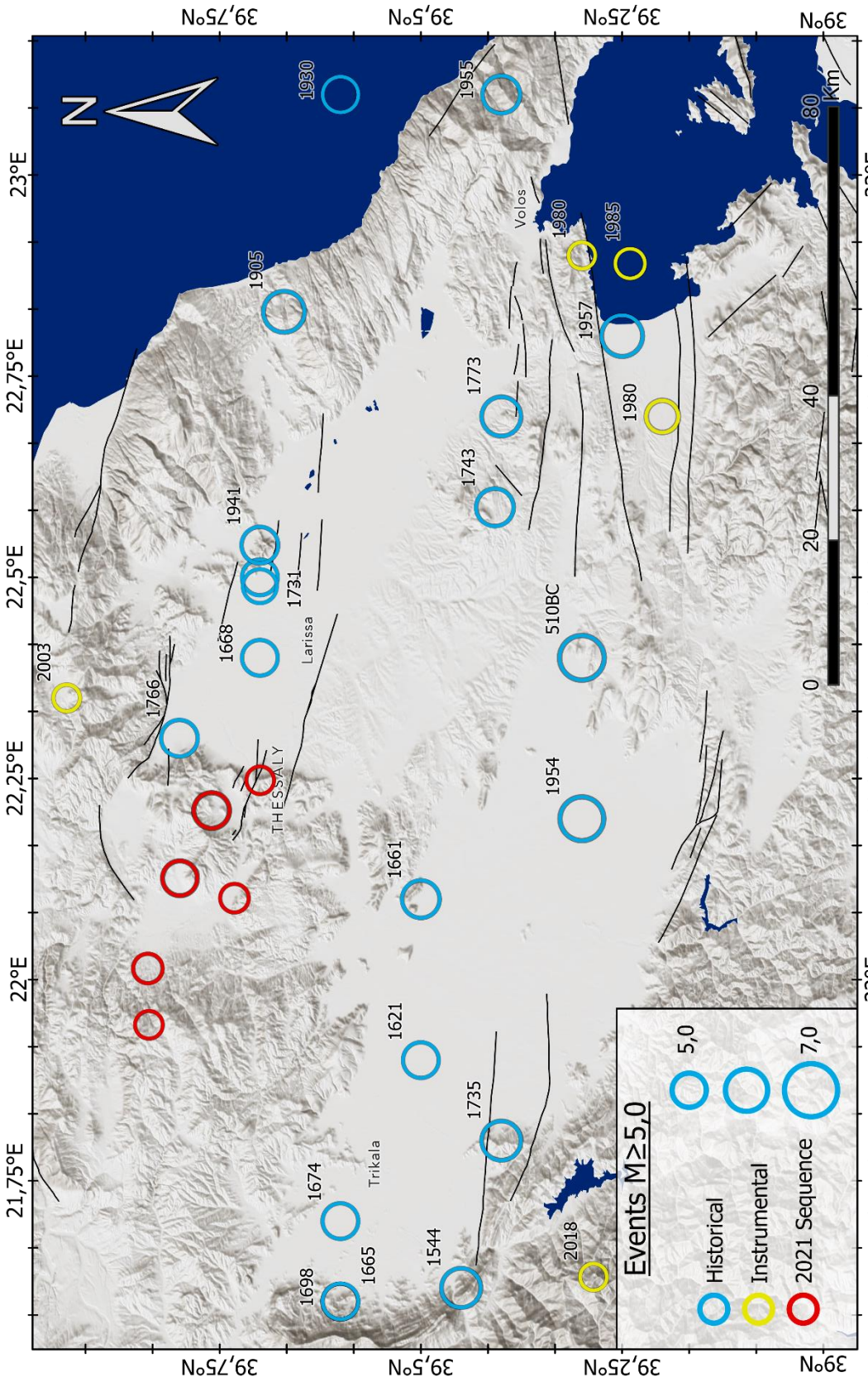

Figure 3.5 *Seismicity map of Thessaly (Central Greece) from 510BC to 2021AD. Blue circles correspond to the historical recorded events (Papazachos & Papazachou, 2003; Caputo et al., 2006; Stucchi et al., 2013), yellow circles correspond to the earthquakes between 1965 and 2018 (IG-NOA) and red circles correspond to the 2021 earthquake sequence relocated catalogue (Kassaras et al., 2022). The black lines correspond to NOA active faults v.4.0 (Ganas, 2020).*

3.4 The 2021 earthquake sequence

On March 3, 2021, an M_w6.3 earthquake occurred in the graben valley of Titarisios river, 10 km West of Tyrnavos town (Figure 3.5). Along with two more mainshocks on March 4 (M_w6.0) and March 12 (M_w5.6) they occurred on a hidden fault system forming the Northern Thessaly 2021 earthquake sequence. However, the beginning of the sequence is considered to be a few days before the first mainshock, on February 20, 2021, while its foreshock sequence is active more than a year later with medium magnitude events (23/08/2022, M_w4.1; 25/01/2023, M_w3.6). According to the focal mechanisms and epicentre distribution of Figure 3.5 the active stress field corresponds to the NE-SW extension of the Late Miocene, which has changed to N-S since the Middle Pleistocene, as described previously.

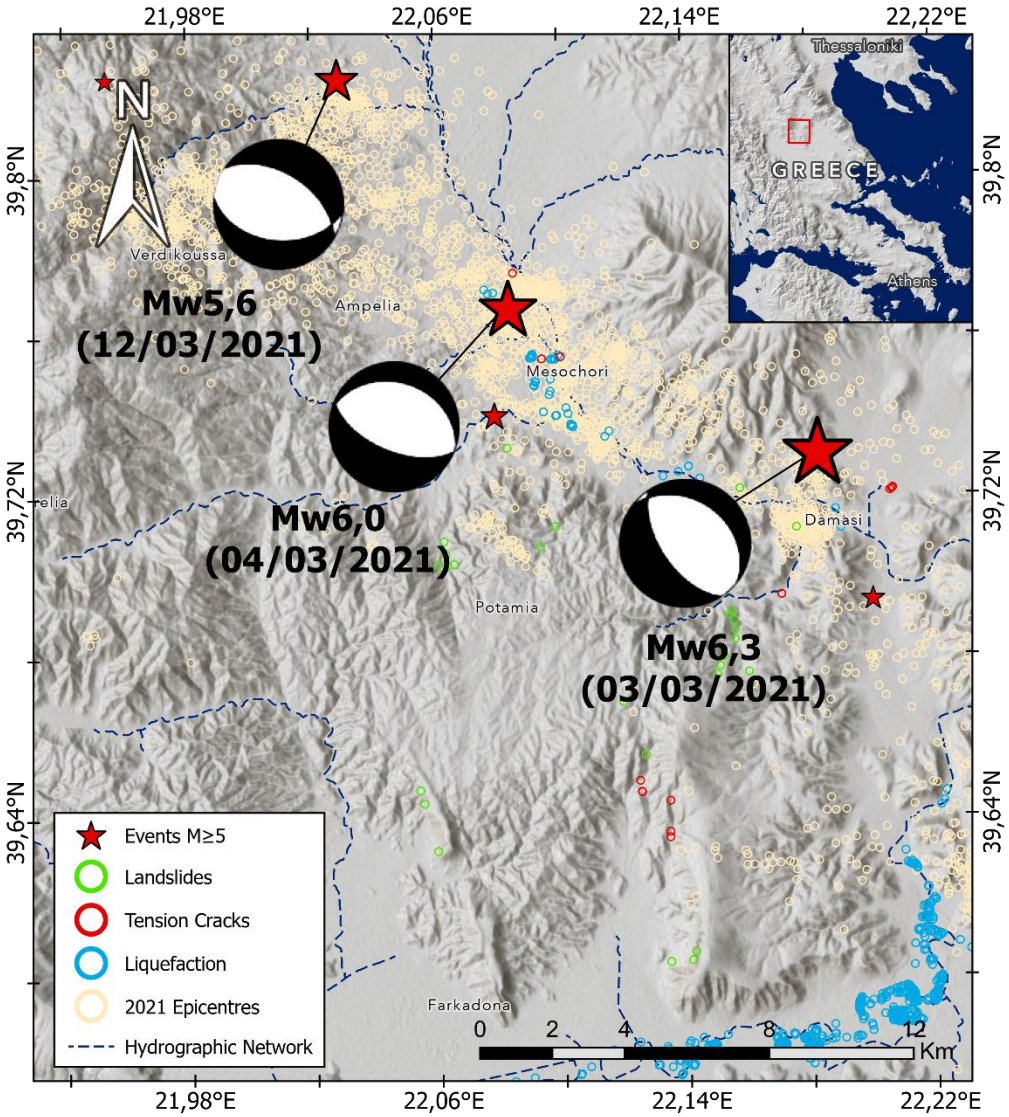

Figure 3.6 *Hillshade map of the N. Thessaly 2021 epicentral area showing the 2021 mainshock focal mechanisms (Ganas et al., 2021), the 2021 sequence relocated epicentres (Kassaras et al., 2021) and the secondary effects. The landslide locations are taken from Ganas et al. (2021) and the liquefaction from Papathanasiou et al. (2022).*

The terms *hidden* or *blind* are to emphasize the seismic fault's shape that does not reach the surface of the earth or does partly. From the field observations, there are not any typical fault scarps that can be directly associated with the seismic fault but the activation of other faults of the area as sympathetic structures is indicated. Along the seismic fault trace as proposed by geodetic and seismic data, there are NW-trending shear zones in the crystalline bedrock, accompanied by co-seismic tension cracks (Figure 3.6). These are kinematically related to the hidden fault denoting the existence of a significant fault zone.

Besides the tension cracks, several primary and secondary effects were reported in the epicentral area. As shown in the map of Figure 3.5 liquefaction is the most common of them, occurring mainly immediately after the first mainshock (M_w6.3) at the riverbanks of Titarissios and Pineios rivers. Surprisingly, the liquefaction areas are more accumulated at the Pineios valley than at Titarisios graben-valley, which corresponds to the 2021 epicentral area (Figure 3.5). Liquefaction phenomena were accompanied by the development of ground fissures and craters, while landslides were also reported nigh to active faults in the broader area (Chatzipetros et al., 2021; Ganas et al., 2021; Valkaniotis et al., 2021; Papathanassiou et al., 2022).

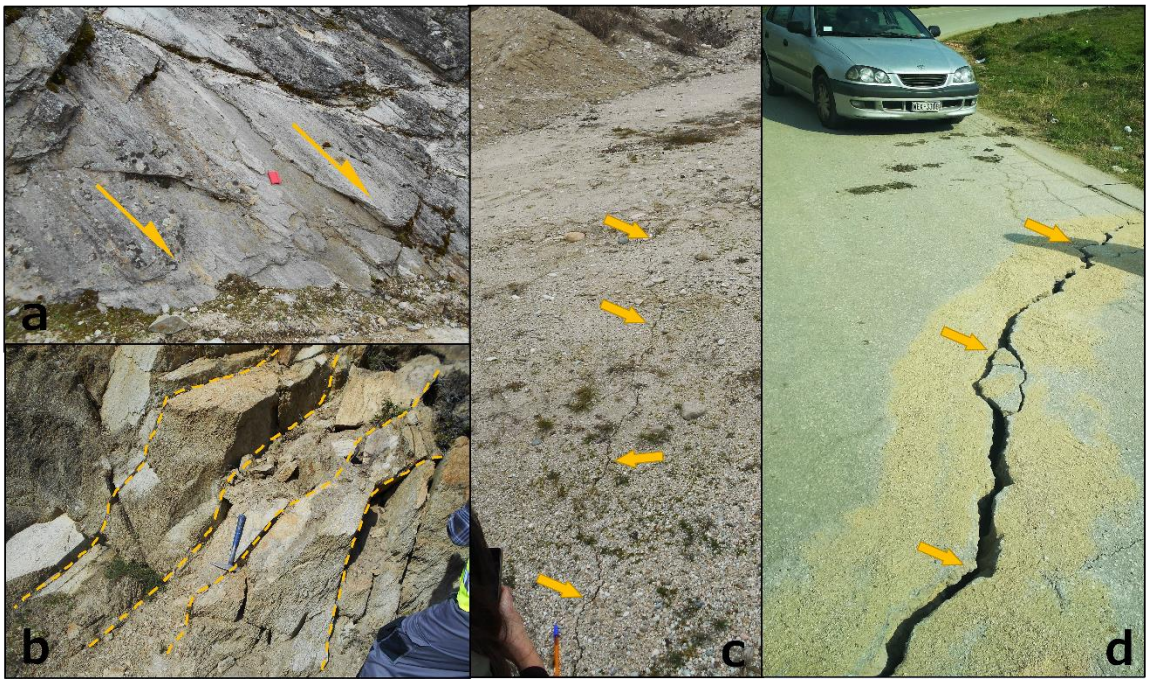

Figure 3.7 *a) Exposed fault surface of the Zarkos Fault Zone in the crystalline bedrock, b) Cataclasite and opening in Paleozoic crystalline bedrock associated with the Zarkos Fault Zone, c) Co-seismic surface fissures in the area of Titarissios Valley, following the inferred strike of the graben, d) Co-seismic rupture on the asphalted road associated with lateral spreading NW of Mesochori village.*

4. TERMINOLOGY, DATA AND METHODOLOGY

4.1 Terminology

Throughout this thesis, various terms are used to describe fault geometry, earthquake magnitude etc. Therefore, a few definitions and schematic illustrations are presented here for the reader's better understanding of the study.

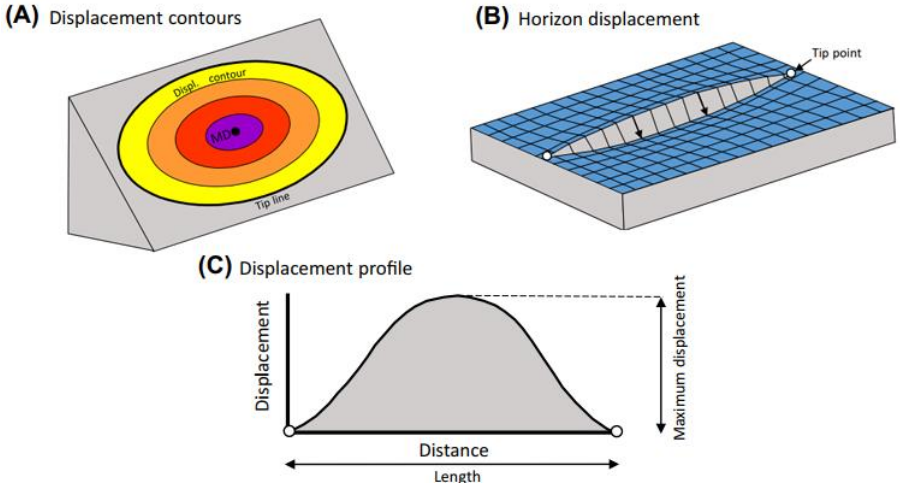

Figure 4.1 *Schematic diagram of the ideal isolated normal fault showing (A) displacement contours on the fault surface, (B) oblique view of a displaced horizon and (C) strike-parallel displacement profile. MD in (A) refers to maximum displacement, arrows on the fault plane in (B) indicate fault slip vectors, and open circles in (B) and (C) show the locations of the fault tips (Nicol et al., 2020).*

Fault displacement is one of the most important parameters for characterizing the fault properties, and can be also used as an indicator of the fault growth history (Anders & Schlische, 1994; Nicol et al., 2020). Displacement is defined as the relative movement between two originally adjected points on the fault's surface (Peacock et al., 2000). Figures 4.1 and 4.2 show the spatial variation of the displacement along a planar fault surface and how it may indicate segmentation boundaries on it.

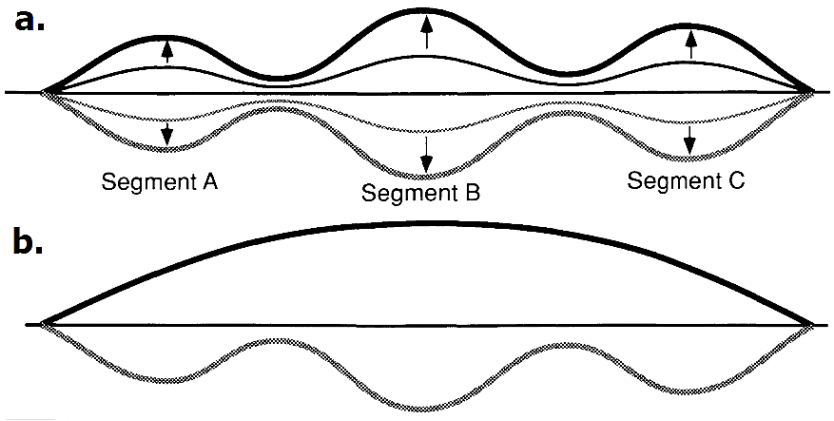

Figure 4.2 *Hypothetical footwall elevation profile (solid) and depth to basement on hanging wall block (shaded) along segmented normal fault system. In (a) it is assumed that the fault segment boundaries are regions of slip deficit, whereas in (b) the boundaries are regions of fault splaying and overlap (Anders & Schlische, 1994).*

Faulting is a long-term dynamic process of nature which results in the creation of complicated structures, consisting of multiple surfaces linked to each other or not, depending on the stage of their growth. The fault surfaces can be isolated, soft-linked or hard-linked based on the fault growth models of Cartwright et al. (1996) and Walsh et al. (2003). The growth of the different linkage models is displayed in Figure 4.3.

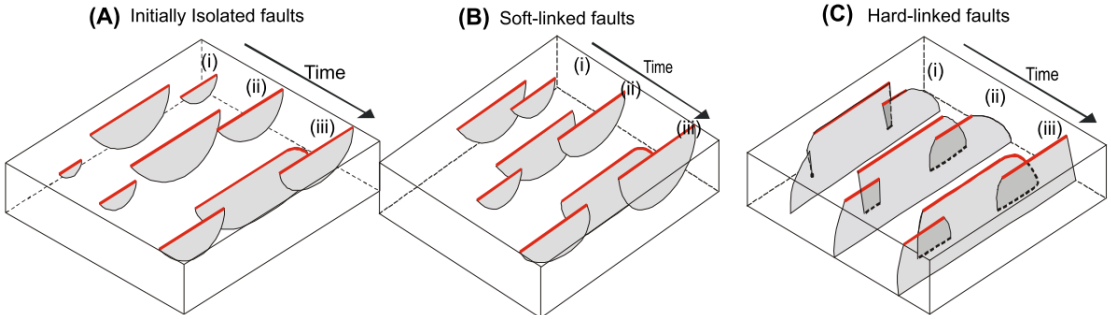

Figure 4.3 *Schematic illustrations of three end-member models for the formation of segmented fault arrays: (A) isolated faults, (B) soft-linked fault segments arising from 3D segmentation or (C) hard-linked segments due to fault surface bifurcation. Each block diagram shows three stages in the growth of a segmented fault array (i-iii). Initially isolated faults (A) require early fault propagation and independence followed by coherent growth, while the soft-linked (B) and hard-linked (C) diagrams both require coherent fault growth from the onset faulting (Nicol et al. 2020, modified from Walsh et al. 2003)*

The in-depth linkage between multiple fault segments that are kinematically related is indicated by *Relay zones* that appear on the earth's surface, as displayed in a normal faulting example of Figure 4.4, according to Childs et al. (2009). The segments' kinematical relationship is declared by the transfer of displacement between them due to the strain that develops within the relay zone.

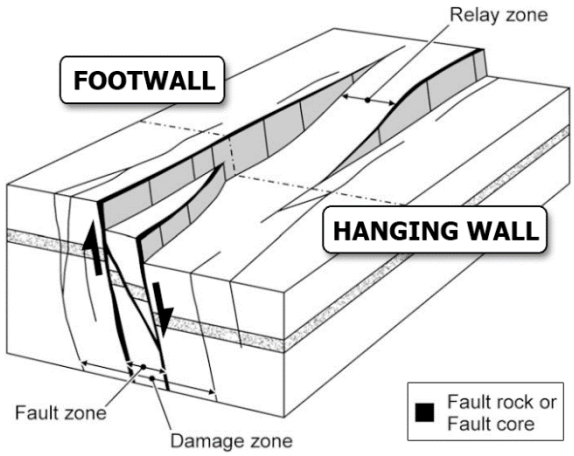

Figure 4.4 *Schematic diagram explaining the terms: fault rock, fault zone and damage zone on a normal fault structure. At the centre of the block diagram (along the dashed line) the bulk of the displacement is accommodated on a single slip-surface and therefore the fault zone thickness is equal to the thickness of the fault rock. Thin lines indicate faults with minor displacements (after Childs et al., 2009).*

The damage zone is the part of the rock that received most of the damage due to the movements of the hanging wall and footwall blocks. Inside its boundaries, there is a smaller zone that corresponds to a system of interacting and linked fault segments, restricted to a narrow band or volume, referred to as a *Fault zone*. This is bounded by thin

layers of *Fault rock* or *Fault core*, which refers to the parts of rock with the weaker mechanical properties (fault gouge, breccia and cataclasite) due to the brittle deformation (Childs et al., 2009; Peacock et al., 2000).

Fault surfaces are where earthquake events occur and therefore their geometry is associated with the energy released due to an earthquake. *Seismic Moment (M_o)* refers to a quantity measured in dimensions of torque that describes the earthquake size in distribution with the geometrical parameters of the seismic source, as follows:

$$M_0 = \mu \times D \times A$$

where M_0 (Nm) is the seismic moment, μ (N/m^2) is the shear modulus of the rocks involved in the earthquake, D (m) is the average slip of the surface due to the earthquake and A (m^2) is the area of the fault surface (Aki, 1966; Bormann et al., 2013). Seismic Moment is the basis of today's most accurate earthquake scale, the Seismic Moment Magnitude (M_w). According to Hanks and Kanamori (1979), the relationship between Seismic Moment (M_0) and M_w is nearly coincident for Local Magnitude (M_l) and Surface Magnitude (M_s) scales: $M = ⅔ \log M_0 - 10.7$, which is uniformly valid for $3.0 \lesssim M_l \lesssim 7.0$, $5.0 \lesssim M_s \lesssim 7.5$, and $M_w \gtrsim 7.5$.

4.2 Data Collection

The rise of the N. Thessaly sequence's international appeal has resulted in a significant amount of data available online. The availability of supplementary material from the already published works is important for the research to keep going on this topic by more researchers.

The data was very important for the fault modelling part, which is a key feature of this study. The 2D modelling was based on correlations between the already known geological data with the morphology, the sequence's InSAR images and collected field data. This research used final InSAR products made of the subtraction of pre and post-event Sentinel images. The main source for the images used here is the supplementary material of De Novellis et al. (2021).

The geological data used for correlations with the new data and the Zarkos Fault Zone 2D interpretation is based on the 1:50.000 geological map series published by IGME. The four map sheets that cover our study area are those of "Gonni", "Farkadon", "Larissa", and "Elasson" (Institute of Geology and Mineral Exploration, 1985a, 1985b, 1987, 1998).

Digital Elevation Models are used in this study for the model presentation and morphometrical analysis. For presentation and design purposes is the SRTM 30 m, while the morphometrical is applied on the Hellenic Cadastre's 2 m resolution DEM (Legal Entity of Public Law Hellenic Cadastre, 2014).

For the second stage of the fault modelling attempted in this study, an accurate relocated seismic catalogue is required. Kassaras et al. (2022) relocated catalogue is used for this purpose. Nevertheless, several available seismic catalogues (relocated or routine)

are also analyzed statistically and used for correlations with other published works (Ganas et al., 2021; IG-NOA, n.d.; Karakostas et al., 2021; Mouslopoulou et al., 2022).

Furthermore, data were obtained from fieldwork at the N. Thessaly 2021 epicentral area that took place in two periods. The first part was during the survey of the Earthquake Geology Research Team immediately after the two mainshocks (03/03/2021 and 04/03/2021). Our main goal then was to map all the secondary effects of the sequence and find evidence that confirm the InSAR images' shown displacement. Although there was not any vertical displacement recorded, a fault scarp along with associated tension cracks was observed in the mountains of Zarkos. All observable surface effects were documented and mapped.

In the Autumn of 2021, a few months after the main sequence, there was a second period of fieldwork in the epicentral area. That was focused on the Vlachogianni Fault, which is not the seismic one but is the most important fault activated within the epicentral area. Based on the hydrographic network and watershed, we tried to find evidence for neotectonic activity and measure possible exposed outcrops of it.

4.3 Morphotectonic analysis

This work part encompasses all the analysis held with the common geoprocessing tools of ArcGIS Pro and the basic statistical analysis of Microsoft Excel. We analyzed the InSAR raster images and extracted displacement contour lines which were the basis for the seismic fault traces' construction.

In order to understand the spatial relationships of the seismic faults a detailed morphometric analysis on a high-resolution Digital Elevation Model was required. Thus, we examined the epicentral area's slope and elevation from the Greek Cadastre's 2 m DEM (Legal Entity of Public Law Hellenic Cadastre, 2014) with the slope gradient tool and multiple cross-sections perpendicular and parallel to the interpreted faults. The combination of a high-resolution input DEM and high-quality software results in intricate models upgrading our research.

For further study and confirmation of the fault system's activity, the hydrological network was extracted from the 2 m resolution DEM, and a quantitative analysis was performed. The SL and AF indexes were calculated for particular sub-watersheds of the stream network, as follows:

A. Drainage basin asymmetry factor (AF):

$$AF = 100 \times {}^{A_r}/_{A_t}$$

where A_r is the size of the area in the right sub-catchment of the main stream and A_t is the whole catchment area.

B. Stream gradient index (SL):

$$SL = \frac{\Delta H}{\Delta L \times L}$$

where ΔH is the altitude difference between two points in the watercourse, ΔL is the length of this stretch and L is the total length of the channel (Hack & Young, 1959; Hack, 1973).

4.4 Fault mapping

A pre-modelling work was necessary to prepare the input data for the 3D modelling associated with the morphotectonic analysis discussed above. It was focused on the interpretation of the Synthetic Aperture Interferometric products from previously published works (Chatzipetros et al., 2021; Ganas et al., 2021; De Novellis et al., 2021; Kontoes et al., 2022). The supplementary data from De Novellis et al. (2021) was used for extracting contour lines and in correlation with the area's slope gradient map they resulted in a set of fault traces illustrated in multiple maps.

The final set of fault traces comprises the main activated faults according to the InSAR data and traces indicated by the morphology that seem to have a kinematical relationship with the activated ones. The secondary faults were important for the 3D modelling process because the earthquake hypocentre clusters did not correspond totally to the InSAR-derived faults and more traces were needed for the model construction.

The 3D model construction was held in the MOVE suite by Petroleum Experts, which is an asset for geological modelling in complex environments. The hypocentres of Kassaras' relocated catalogue were analyzed in 3 dimensions and several clusters were interpreted. The interpretation was based on the propagation of the events and the geometry of their distribution.

The method for a 3D surface building was based on the construction of polygons inside the specific cluster following its general geometry. The polygons were constructed by connecting hypocentre points and afterwards, they were divided into smaller shapes (triangles preferably) for increasing the detail of the final surface. In the last step of the process, an automated surface construction tool of the software based on Kriging interpolation was used, resulting in the final 3D fault surface model. This tool connected the deep-laying surfaces with the fault traces that were projected on the DEM surface for more geologically rational and realistic results. In this part, the DEM of 30m resolution was used and not the 2m resolution because of its easier loading in the 3D environment.

5. 2D MAPPING OF THE ACTIVE FAULT TRACES

The images produced with InSAR analysis are important in identifying the surface changes due to an earthquake, especially in the case of morphogenic earthquakes. This data can indicate new faults, confirm the already mapped ones or both, as in our case.

The different parts of the analysis presented below are not different steps of a straightforward process but are always correlated with each other. The process results in a 2d model which describes the main faults of the 2021 broader epicentral area and their geometrical interrelation.

5.1 Fault mapping using InSAR

The main interpretation of the seismic fault traces is based on the co-seismic displacement derived from the Synthetic Aperture Radar (SAR) interferometry products and the local geomorphological conditions. The zero displacement contour lines (white lines in Figure 5.1a-b) that are extracted from InSAR images (De Novellis et al., 2021) do not correspond necessarily with typical active faults but indicate possible hidden faults or local thresholds of immobility in the subsurface. The fault traces are essential for the 3D model construction, as explained in the next Chapter.

As shown in Figure 5.1, there is a deviation between the displacement fringes that correspond to a mainshock when the period of image extraction increases and the deformation field of more mainshocks is added to the final image. Moreover, there is a deviation in the lower magnitude third event's images resulting from different satellite tracks with negligible time differences (Figure 5.1c-d). Therefore, the zero-displacement contours of the M_w6.3 and M_w6.0 events inspire more confidence in interpreting fault traces than the third mainshock.

The fault traces resulting from the InSAR-derived zero-displacement contour lines are displayed on the gradient slope map of Figure 5.2 in correlation with the area's morphology, forming the basis of this thesis' fault model interpretation. Thus, F1 is the fault trace that corresponds to the main fault surface where the 2021 earthquake doublet occurred. Although F2 corresponds to the zero-displacement contour lines of the InSAR products, its role in the 3D model is secondary, as explained in the next chapter (Chapter 6), while F3 is proven incompatible with the seismic data leading to the interpretation of F4 trace. This trace corresponds to a steep linear slope located at the zero displacement area according to the third mainshock's InSAR images and parallel to the F3 trace.

The main argument of the different interpretations of the specific fault model has to do with the dip direction of the fault that corresponds to the third mainshock of M_w5.6, and although it is further discussed in the next chapters, it needs to be mentioned here too. Therefore, the morphology is analyzed for possible antithetic faults that may correspond to the third mainshock and its related cluster of earthquakes. The only antithetic surface derived from the slope gradient map (Figure 5.3) is incompatible with

both the earthquake cluster and the InSAR displacement contours. Nevertheless, the existence of a small-scale blind conjugate system of normal faults cannot be excluded.

Correlating the InSAR-derived fault traces with the slope gradient and the geology of the epicentral area is crucial since it may provide more fault traces which are important for the 3D modelling. Therefore, several fault traces that seem to be kinematically related to the main four of Figure 5.2 are displayed on the map of Figure 5.3. The yellow-stroked fault traces correspond to the structures that are interpreted from the morphology, while the colour stroke in Figure 5.4 distinguishes the faults used in the 3D model. Fault trace F5 is the morphological extension towards NW of the main fault F1, while F6 corresponds to a semi-parallel structure that possibly has developed a linkage to the main fault. Finally, F7 is a small structure linked to F4 that is associated with the third mainshock of M_w5.6, as explained in the 3D modelling chapter.

Furthermore, in Figure 5.4 there are displayed a few rose diagrams grouping spatially the fieldwork measurements of co-seismic surface tension cracks at the epicentral area. Regardless of their association with liquefaction or not, their strike is in general agreement with the main directions of the area's active faults. Interesting here is the secondary axis (NNE-SSW) developed in the cracks of area a2 at Titarisios River graben-valley, which is different from the main trend (NNW-SSE), probably associated with the local topography. the NW-SE direction of the area's main structures, while tension cracks near Tyrnavos Fault follow its E-W direction. A second axis is also observed in the rose diagram of the a3 area, which is highlighted with blue colour due to its special nature. It corresponds to the displacement vector (ENE-WSW) which is different from the crack's main trend (NW-SE) and is associated with the local average direction of extension.

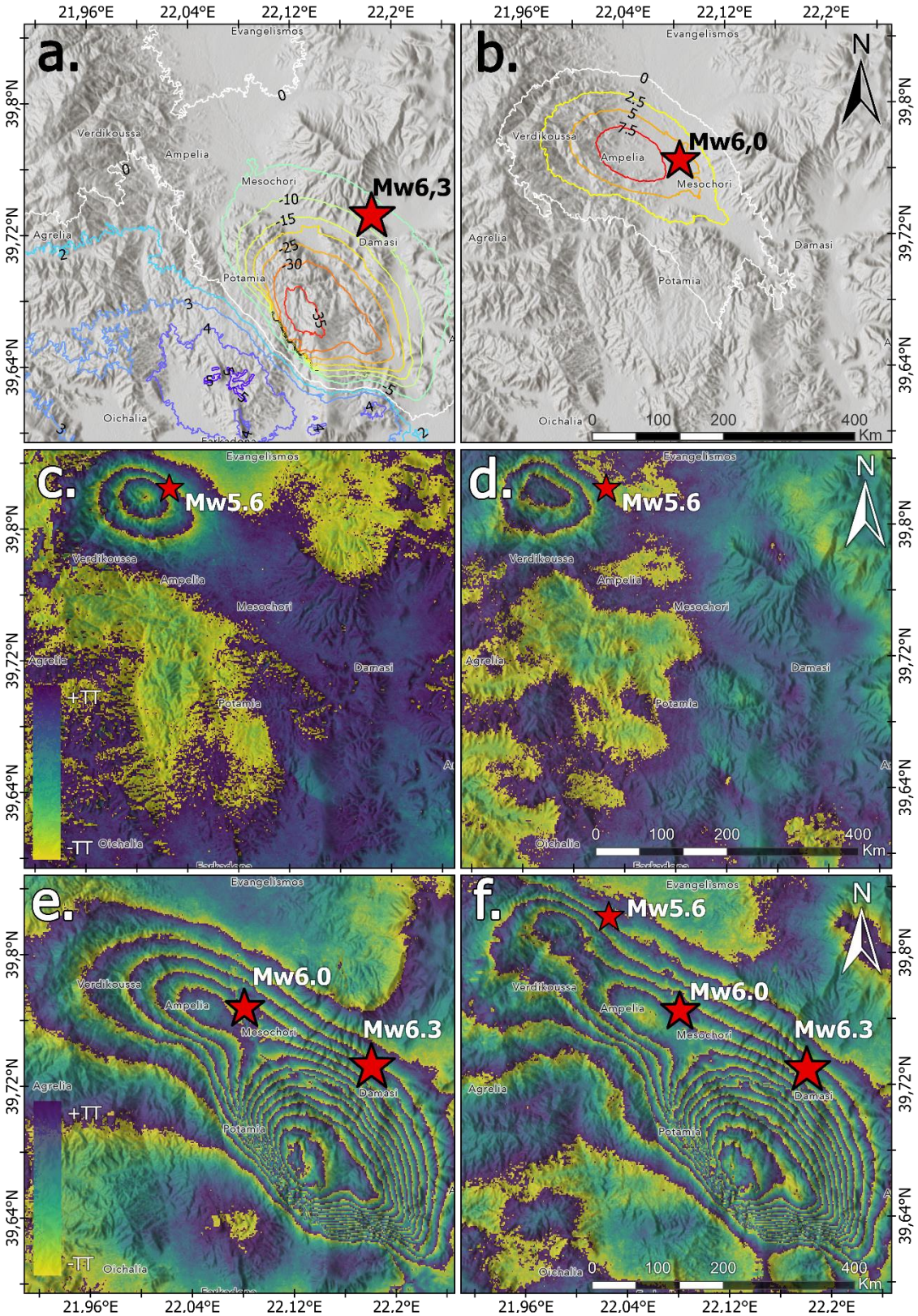

Figure 5.1 *Spatial distribution of Northern Thessaly 2021 sequence's co-seismic displacement from SAR interferometric products (De Novellis et al. 2021). a), b) Interferograms illustrating the deformation field of Mw5.6 event of 12/03 from c) a descending and d) an ascending satellite track. e), f) Interferograms illustrating the total deformation field of e) Mw6.3 and Mw6.0 mainshocks and f) all the three mainshocks (Mw6.3, Mw6.0, Mw5.6).*

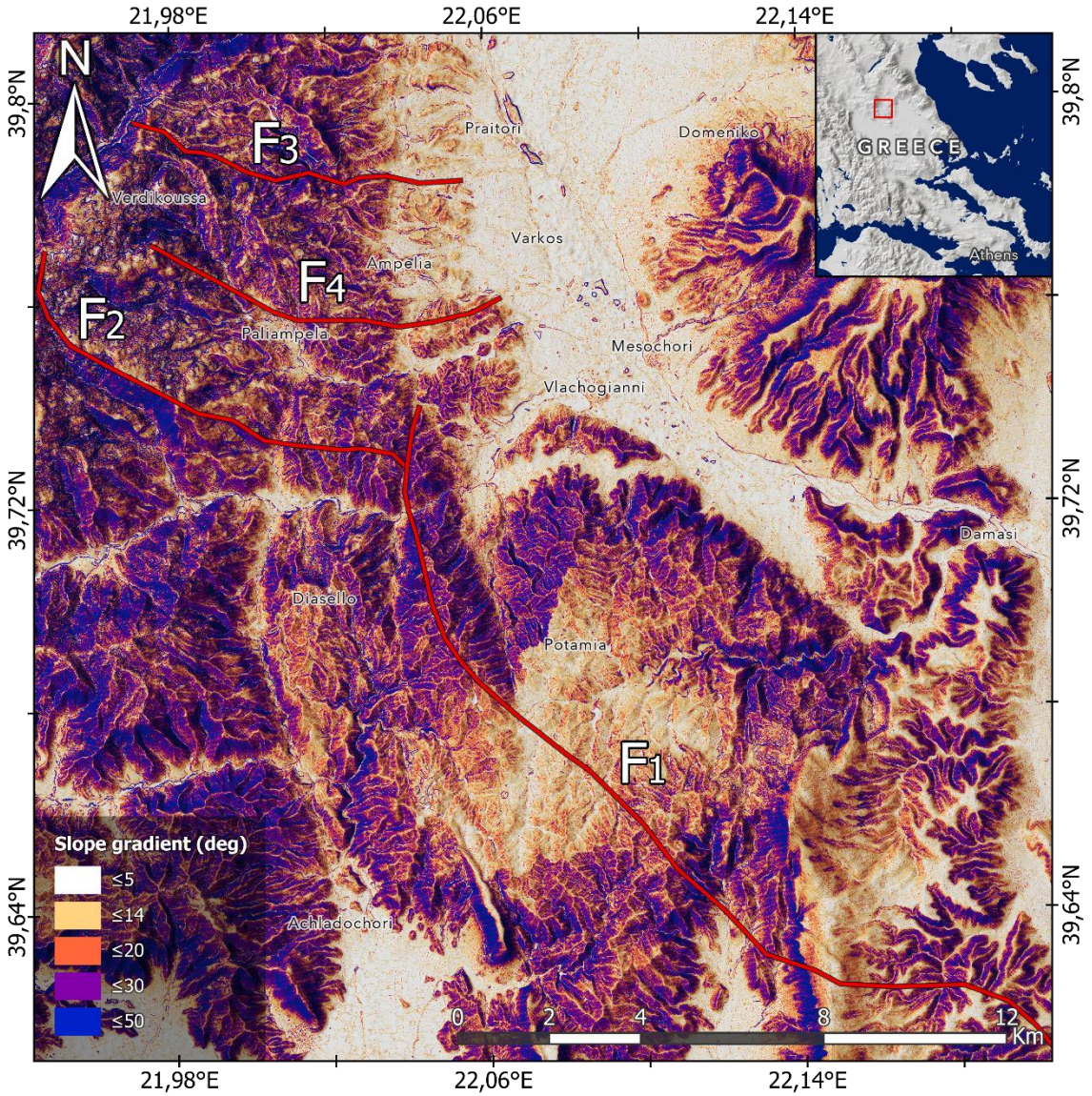

Figure 5.2 *Slope gradient map of the Northern Thessaly 2021 epicentral area based on the Hellenic Cadastre's 2m resolution DEM (Legal Entity of Public Law Hellenic Cadastre, 2014). Red solid lines correspond to the fault trace interpretations from the InSAR images. F1 is the fault trace derived from the first mainshock associated zero-desplacement contour lines interpreted as the main seismic fault of the sequence, F2 is a segment of the F1 fault revealed from deformation field of the second mainshock (zero-displacement contour lines), F3 is the fault trace derived from the zero-displacement contour lines of the third mainshock (descending satellite track), F4 is a fault trace kinematically related to F3 as derived from the slope gradient and the InSAR images associated also with the third mainshock.*

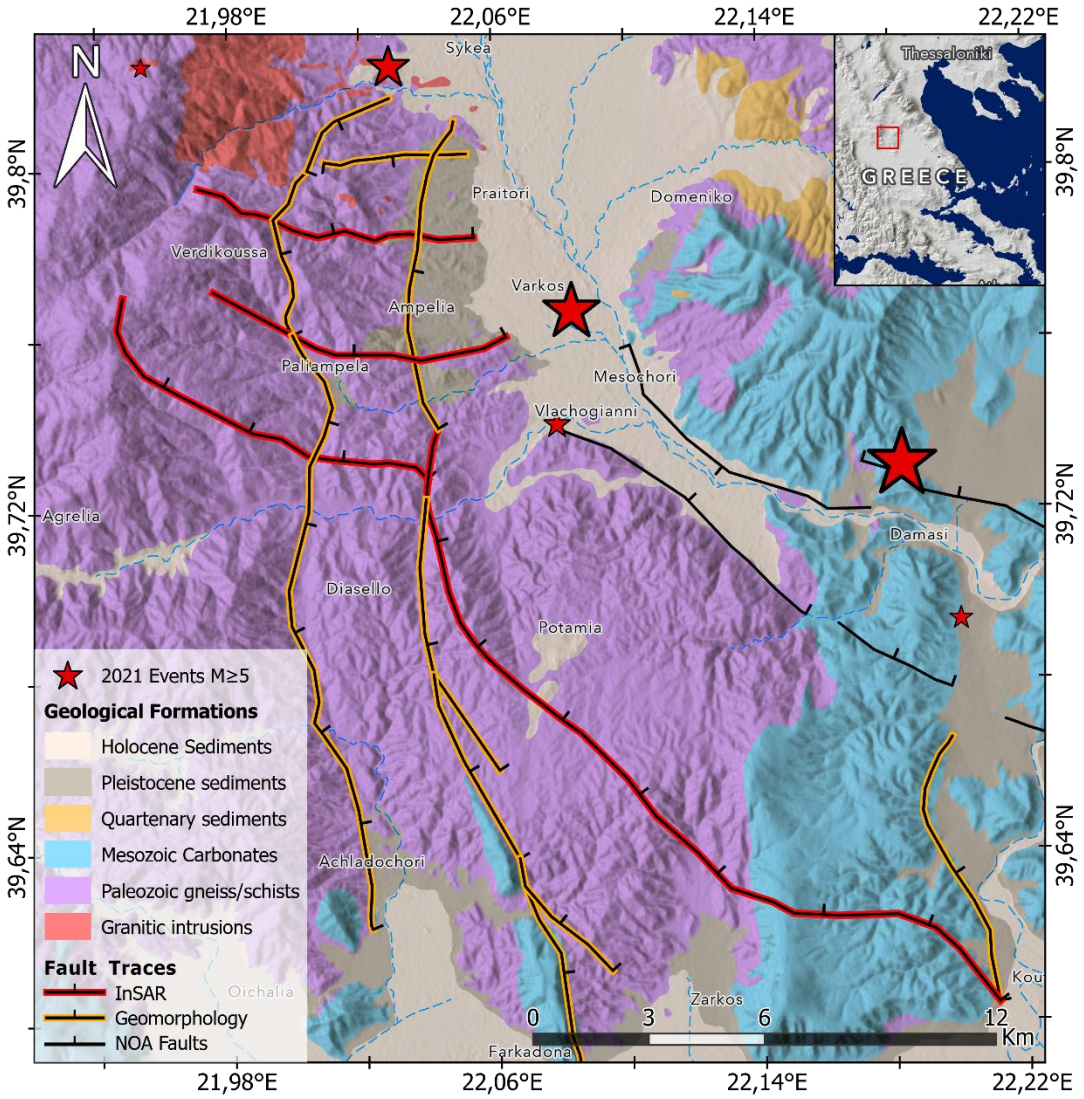

Figure 5.3 *Simplified geological map of the Northern Thessaly 2021 epicentral area showing the 2D interpretation of Zarkos Fault System along with dip direction indicators. The colour stroked lines correspond to the main activated fault surfaces of Zarkos Fault System (red colour) and to secondary parts of the system (yellow colour) displayed in the 3D model*

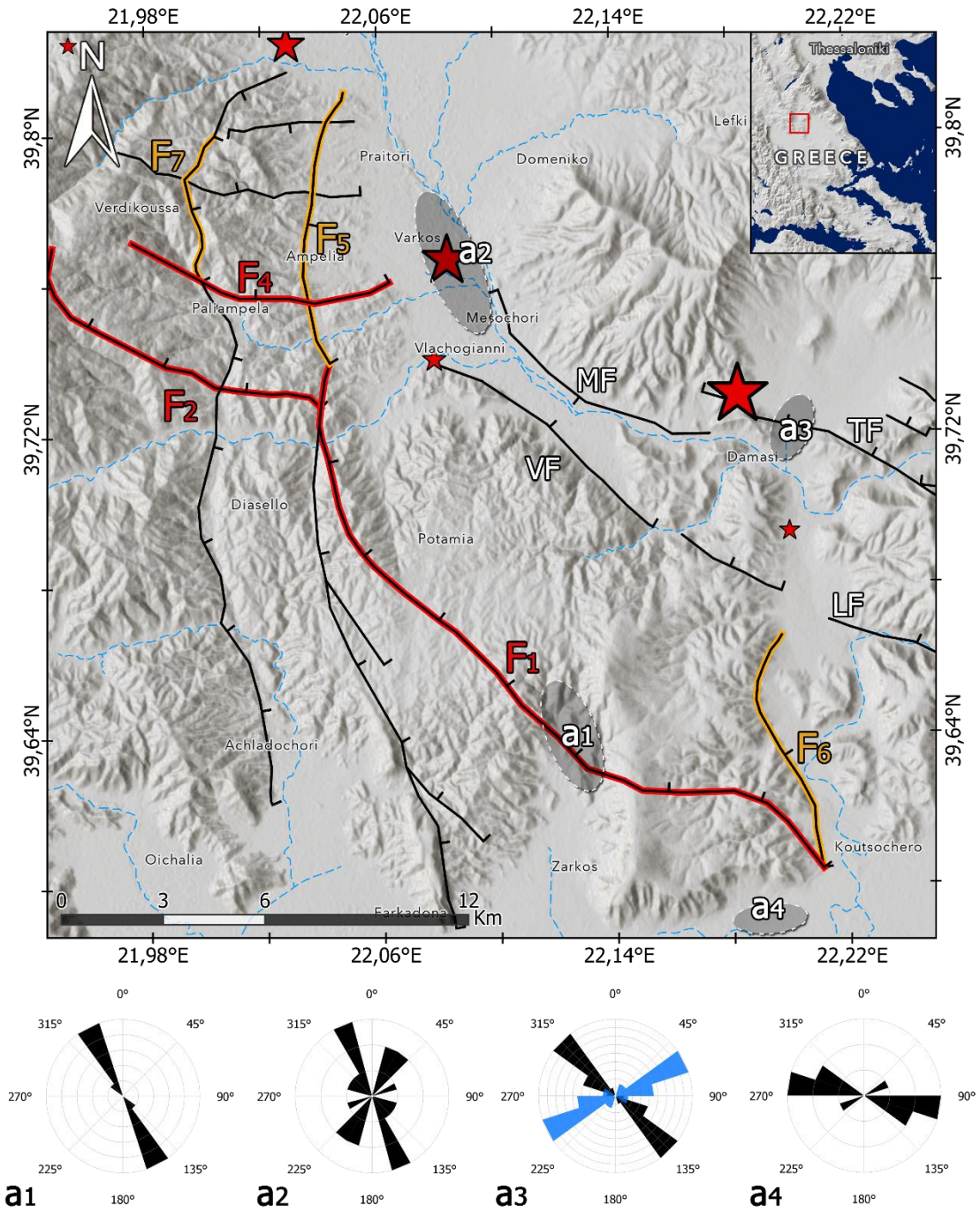

Figure 5.4 *Hillshade map of the Northern Thessaly 2021 epicentral area showing the 2D interpretation of Zarkos Fault System along with dip direction indicators. The colour stroked lines correspond to the main activated fault surfaces of Zarkos Fault System (red colour) and to secondary parts of the system (yellow colour) displayed in the 3D model.: F1, F2 and F4 are explaind in Figure 5.2, F5 is the morphological extension of F1, F6 is a morphology-derived fault trace linked to F1 and F7 is also a morphology-derived fault trace. The other fault acronyms correspond to Vlachogianni Fault (VF), Mesochori Fault (VF), Larisa Fault (LF), Tyrnavos Fault (TF) and Elassona Fault (EF). The dashed ellipses are spatial groups of field measurements of co-seismic surface cracks corresponding with the rose diagrams below the map: a1) Tension cracks on the mountains of Zarkos with a NNW strike associated with the seismic fault, a2) Tension and liquefaction cracks at the Titarisios graben-valley with two main striking axes: a NNW corresponding to the graben's direction and a NNE that is associated with the local topography, a3) Tension cracks on asphalted roads with a NW strike (black in rose diagram) corresponding to Tyrnavos Fault and an ENE displacement vector (blue in rose diagram) associated with the direction of extension, a4) Liquefaction cracks in Piniada valley with a ENE strike that corresponds to the valley's direction.*

5.2 Morphometric analysis

Understanding the area's morphology is essential for the fault modelling procedure. Specific features or patterns of the morphology are analyzed for the quantification of an area's neotectonic activity, may indicate unmapped faults, and contribute to the investigation of inaccessible areas. In this case, morphometric analysis is used for the confirmation and enhancement of the interpreted fault traces and thus further the founding of our final 3D model.

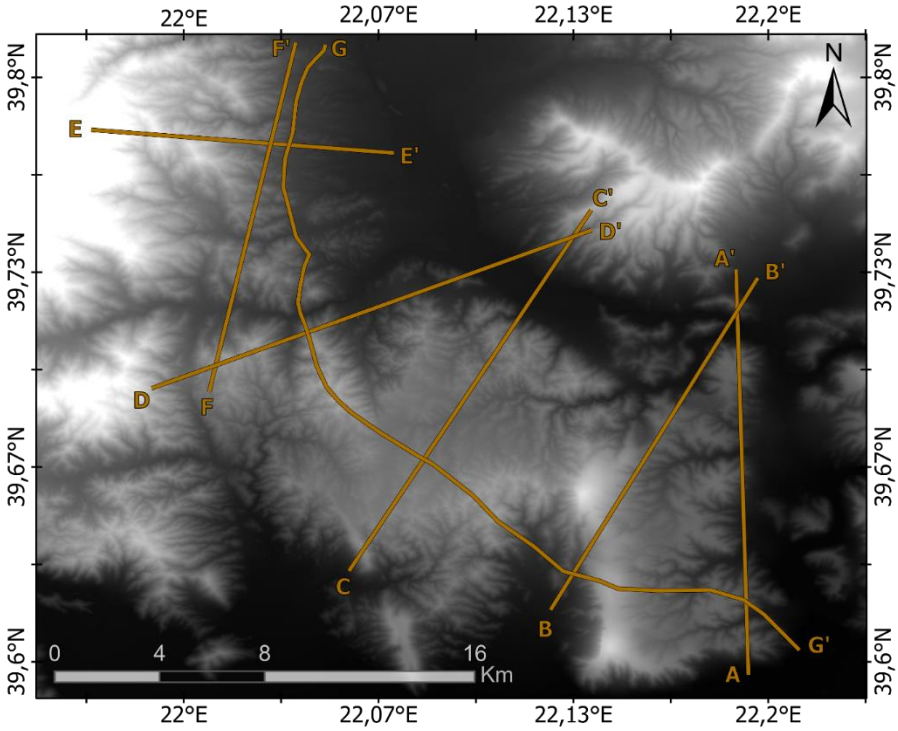

Figure 5.5 *DEM intensity image mosaic showing elevations of the N. Thessaly 2021 epicentral area with profile lines. High elevations correspond to white colour tones, while low elevations to black.*

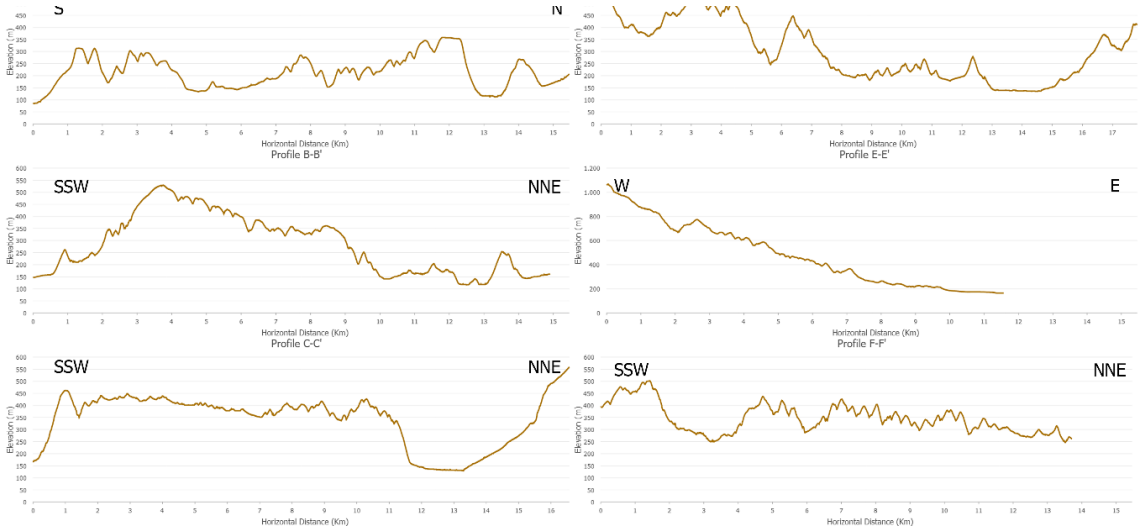

Figure 5.6 *Six elevation profiles perpendicular to the Zarkos Fault Zone (AA', BB', CC', DD', EE', FF').*

Multiple elevation profiles are constructed on the 2m resolution DEM-intensity image mosaic of the epicentral area (Figure 5.5), as demonstrated in Figure 5.6. Transversely to the lineation of the morphology and the interpreted fault trace system, the profiles do not show any new significant breaks on the topography but confirm the main faults of our 2d model. In particular, profiles A-A', B-B', C-C', and D-D' locate the faults of Vlachogianni and Mesochori that bound Titarisios graben valley and show smaller breaks near the Zarkos Fault Zone. All the profiles show a general close to a horizontal elevation which ends with a steep break when it reaches the basin, except the E-E' profile which corresponds to a much smoother transversion between the mountainous area and the lower plateau.

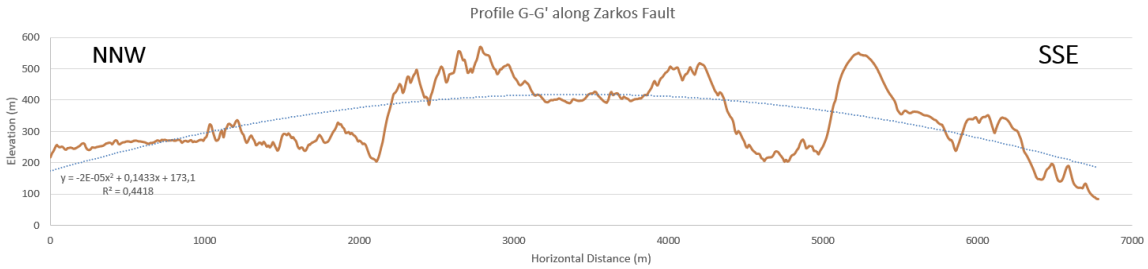

Figure 5.7 *Elevation profile along the footwall of Zarkos Fault (GG'). The blue dashed line corresponds to the best fit curve.*

The elevation profile GG' in Figure 5.7 corresponds to the main seismic fault trace of the Zarkos Fault Zone (F1 in Figures 5.2, 5.4) along with its morphological extension (F5 in Figure 5.4). The along-strike elevation pattern indicates three main fault segments of equal length: one symmetrical at the centre (2000m< x <4700m) and two asymmetrical at the flanks. The flank segments are of lower elevation on average which shows a decrease towards the fault's ends, especially the SE segment (5000m< x <7000m). Although the NW segment's elevation (0m< x <2000m) is mainly flat without any significant high peaks, it shows a general smoothening towards the end tip.

The general elliptical shape of the Zarkos Fault that flattens at the centre and dies out towards the end-tips is typical active fault's footwall geometry at basinal margins (Anders & Schlische, 1994). Notable is that the highest elevations are slightly off-centre, while the tips that indicate the segment boundaries are rather steep. According to the proportional relationship between footwall elevation and displacement, it is assumed that these elevation patterns may be an indication of the displacement history and the growth of the fault segments (Schwartz & Coppersmith, 1984). A displacement profile with similar patterns would be of a typical extensional fault array (Cowie & Roberts, 2001).

5.3 Watershed analysis

As described in previous chapters of this thesis, the Northern Thessaly 2021 epicentral area is in the Southern part of the Domeniko-Amourio basin, a sub-basin of the large Elassona basin and thus an examination of the drainage network is essential.

Although the earthquake sequence of 2021 itself is irrefutable proof of the area's neotectonic activity, a brief analysis of the morphotectonic indices in correlation with our 2D mapping is rather interesting and useful for this and future research on similar areas.

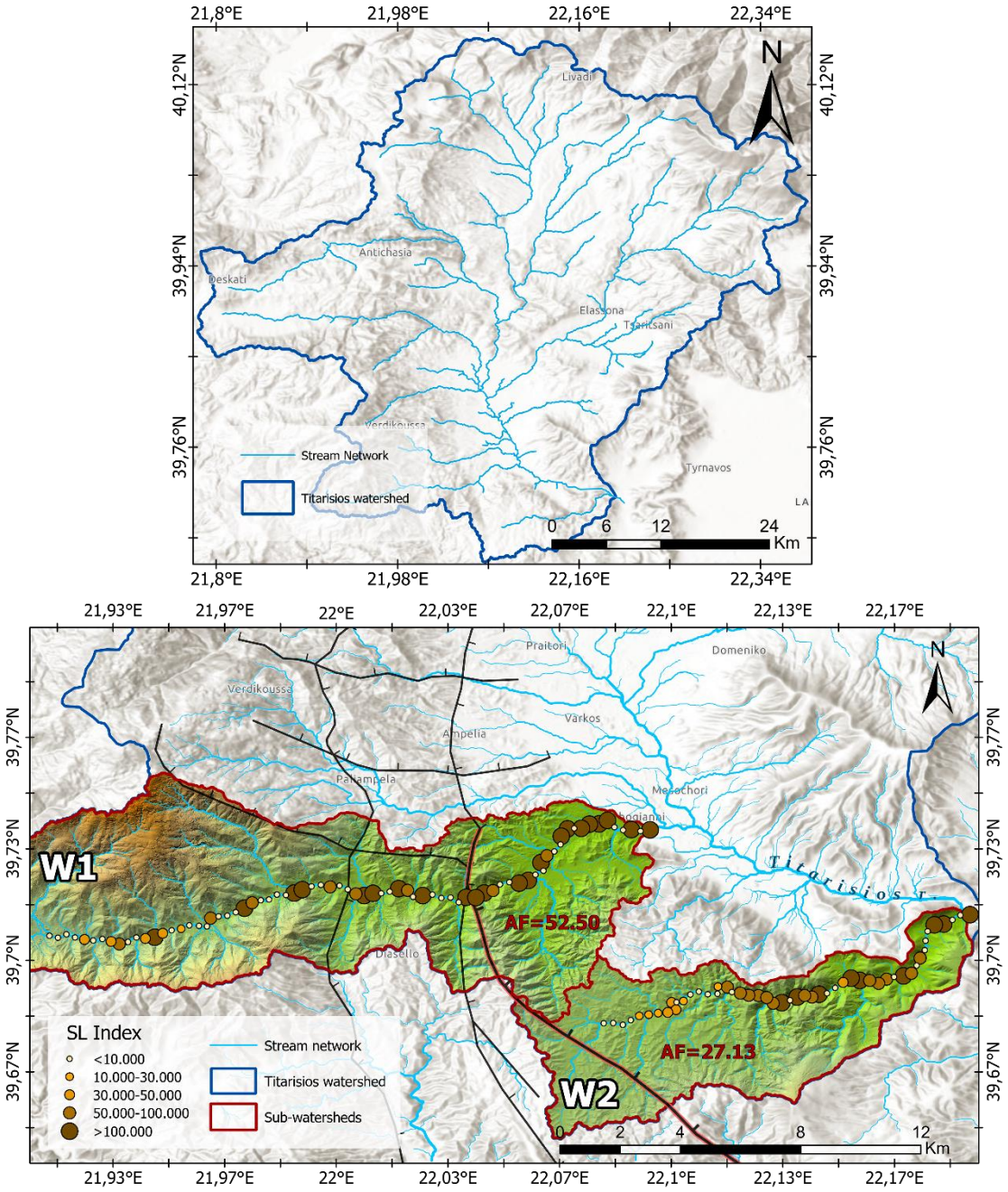

Figure 5.8 *Maps showing the Titarisios watershed in the broader area of Elassona (blue solid line) and the two largest sub-watersheds of the Domeniko-Amourio Basin (red solid line). In the nether map, the two sub-watersheds are displayed along with the Zarkos Fault Zone and the SL index values are distributed as coloured circles along the 6th order (Strahler) streams.*

As shown in Figure 5.8, the analysis was focused on the Southern part of the Titarisios watershed which envelops the whole Elassona basin. The two sub-watersheds that cross the activated part of the Zarkos Fault Zone in the 2021 epicentral area are

examined for any anomalies associated with the fault zone, but the results do not show anything significant. Nevertheless, a few remarks can be made about the drainage system and watershed geometry.

The drainage system of Titarisios River shows a general symmetrical development with an N-S direction that changes to E-W when reaching the Domeniko-Amourio basin and the 2021 epicentral area. However, this steep shift cannot be associated directly with the Zarkos Fault Zone, but with the small faults that bound the graben-valley of Titarisios River (Vlachogianni and Mesochori Faults). This almost 90^{o} bend of the main stream is observed twice at the Pineios River before it connects with Titarisios River at the Thessalian plain. Although the Titarisios watershed seems parallel to the Zarkos Fault Zone, they intersect with each other at the activated part of the Fault Zone as shown in the bottom map of Figure 5.8.

Moreover, there seems to be a small-scale influence on the boundaries of sub-watershed w1 by the Zarkos Fault Zone, as shown in Figure 5.8. The mainly elongated E-W shape narrows steeply in multiple positions in a symmetrical way. This shape pattern is rather intense for the w1 sub-watershed which decreases in width the most when crossing the middle segment of the Zarkos Faut Zone as stated in the profile GG' (Figure 5.7). This is also observed for the Titarisios watershed boundaries and at a smaller degree for the w2 sub-watershed, indicating probably a multiphase tectonic uplift (Baker, 1977; Pazzaglia et al., 1998; Burbank & Anderson, 2013).

The possible influence of the Zarkos Fault Zone on the stream network is analyzed by applying the Stream gradient Index (SL). This is calculated for the main streams of the two sub-watersheds, considering the stream flow, as shown in the bottom map of Figure 5.8. In sub-watershed w1 the SL higher values seem to have a more intense distribution at the hanging wall part than at the footwall of the Zarkos Fault Zone. The changes of the SL distribution here are rather smooth indicating a tectonic uplift maintained of pace and not of sudden episodes. On the other hand, the w2 main stream shows a clear aggregation of low values (SL<50.000) at the beginning of 1/3 of its total length changes suddenly to high values intensely distributed. The anomalies of the SL distribution here may be related to tectonic disturbance or lithological changes (Lifton & Chase, 1992; Troiani & Della Seta, 2008).

6. 3D MODELLING OF THE ACTIVE FAULT SURFACES

After establishing the main aspects of the fault traces' geometry on the 2D maps, we can focus now on the main scope of the thesis which is the seismic fault surfaces' 3D modelling. Although the fault traces do not have the typical surficial expression and thus are considered subsurface structures, their role in the 3D modelling process is crucial. The third dimension added to the faults dataset depends on the accuracy of our previous interpretation and its connection with the seismic data.

This model is developed on the hypocentre cloud of Kassaras et al. (2022) relocated seismic catalogue, which has been used by other researchers and thus there will be a basis for correlation in the discussion chapter. The large number of events (3504) that cover a three-month period and the onset of the earthquake sequence on February 12 are the most important features of the catalogue, distinguishing it from the other catalogues.

6.1 Zarkos Fault Zone model

The fault modelling procedure here is manual and consists of two parts: 1) the analysis of the hypocentres in three dimensions and 2) the construction of the model. The clustering of the events was a parallel process that resulted from the interpretations of their propagation and geometrical features derived from their 3D distribution.

6.1.1 Hypocentre analysis

The 3D modelling process begins with the analysis of the hypocentre point cloud which results in a shape that facilitates interpretations of it. After plotting the earthquake hypocentre cloud in the 3D environment of the PetEx MOVE suite, the outlier values that do not seem to have any direct relation to the main cloud are removed manually. The process continues to the outer layer of the cloud where the points are thinly scattered resulting in a more cohesive point cloud with a clear shape, as shown in Figure 6.1. The shape is important since it can show evidence of the fault surfaces' geometry without going any further.

A lower threshold is set to M2.5 after some experimentation filtering the hypocentre cloud from small events that are useless at the moment. The shape is important since it can show evidence of the fault surfaces' geometry without going any further. In this case, the shape of the point cloud indicates a large fault surface at its SE part which later is interpreted as corresponding to the main seismic fault surface of the Zarkos Fault Zone.

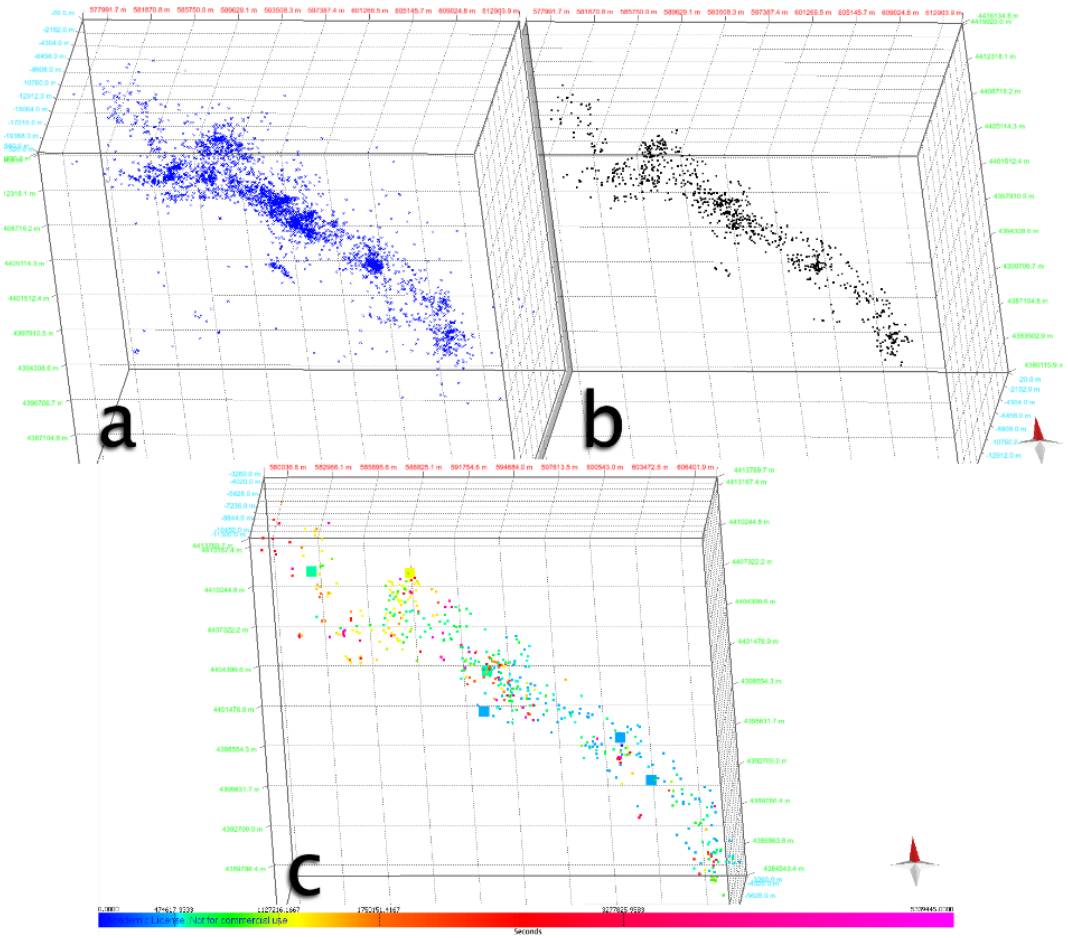

Figure 6.1 *The relocated hypocentre cloud distribution (Kassaras et al., 2022) in the 3-dimensional environment of PetEx MOVE suite for: a) All the events of the catalogue, b) the events M≥2.5 and filtered from outliers, c) the filtered events coloured on a rainbow palette based on their time (dark blue corresponds to the values close to zero seconds).*

Another important feature of the general cloud's shape is the slight curving of its NW half towards the North. The events' propagation confirms this curve begins to form after the formation of the first surface that includes the 2 mainshocks of 3 and 4 March. Moreover, between the end of the first surface's formation and the beginning of the curve, there is a low-depth extension of the cloud at its SE tail. These result in the interpretation of the first two clusters of the hypocentre cloud.

The seismic propagation after the curve and towards NNW is dominated by an almost chaotic distribution, difficult to be interpreted as previously. Since the time and geometry-based analysis cannot go any further, for this part of the modelling, priority is given to the fault surface construction for creating a guideline for the continuation of the clustering process. The clusters that appear in Figure 6.2 are edited and re-evaluated during the construction of the 3D model to achieve this final form and for the NNW part (cluster 4) Kassaras clustering was used as a guide since the manual process we follow is not efficient there.

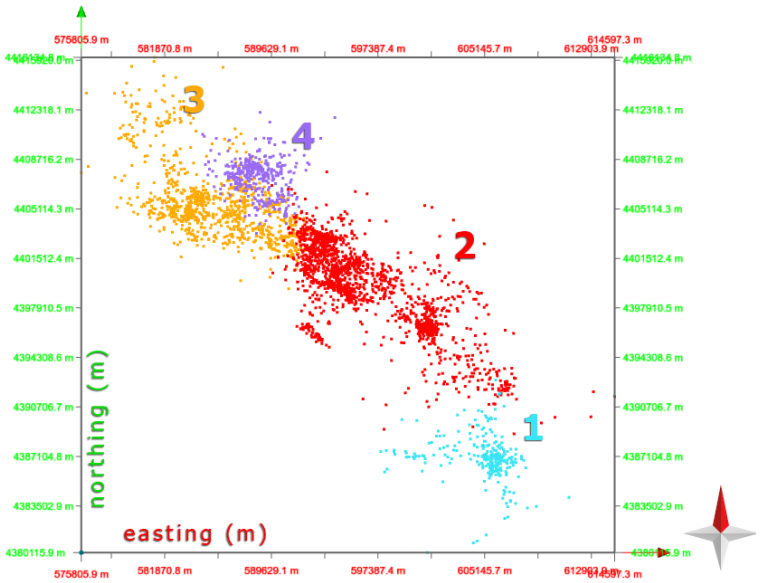

Figure 6.2 *Map view of the Zarkos Fault Zone 3-dimensional model with the scattered hypocentres, coloured according to this thesis' clustering.*

6.1.2 Model construction

The hypocentre cloud analysis results in a better understanding of the clusters' geometry. In the next step of the analysis, each cluster is examined and several polygons are fitted inside it in a way that follows their general geometry. The polygon building is based on the hypocentres, so the polygons' peaks and junctions coincide with them. In Figure 6.3, the example of the basic polygons for cluster 1 is displayed in the 3D environment. The final fault surface is built with Kriging interpolation from the polygons

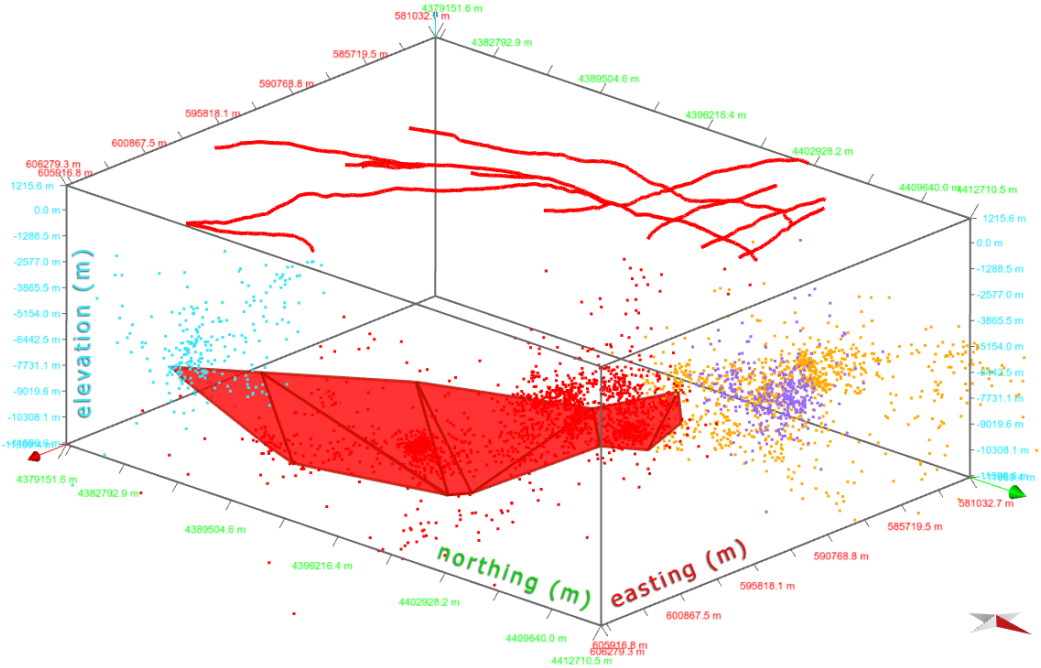

Figure 6.3 *Perspective and view of the clustered hypocentres distribution in 3 dimensions with the basic polygons constructed for the first cluster. The red lines on top represent the fault traces of the Zarkos Fault Zone.*

and the fault traces, as shown in Figure 6.4. The polygons are divided into triangles to add more detail to the model and assist in the better function of the Kriging tool. The fault traces in the final 3D model are projected on the DEM (SRTM) surface for a more realistic result.

The surface construction for the main cluster is crucial for the continuation of the clustering at the complex NW part of the hypocentre cloud because it holds the two events $M_w \geq 6.0$ and therefore it is the main surface of the Zarkos Fault Zone. Correlating this surface with the cloud's shape and especially the higher magnitude events' distribution and propagation, new geometrical patterns appear. The key element here is that the hypocentres propagate following the main surface and then curve towards the North.

All the above resulted in a structure that consists of a large surface with an inwards curve. Smaller surfaces are attached to it and extend the system towards NW, while the extension is combined with an approximate shortening of its height.

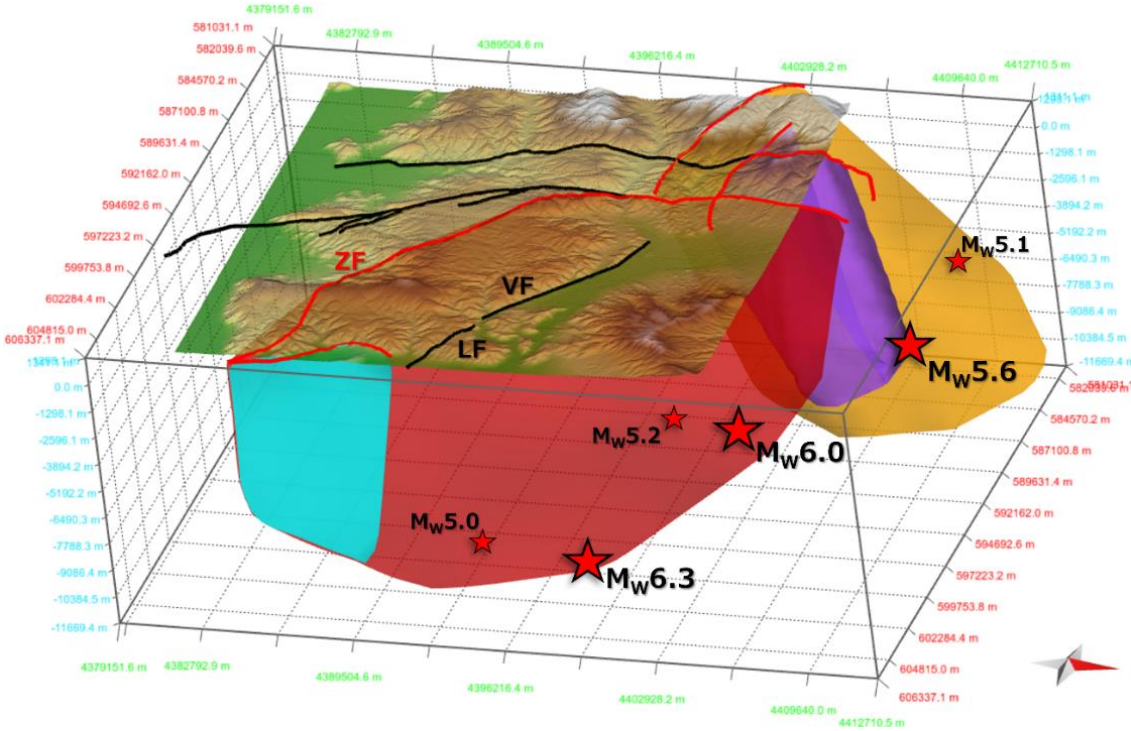

Figure 6.4 *Perspective view of the 3-dimensional model of the Zarkos Fault Zone's surfaces activated during the N. Thessaly 2021 earthquake sequence, and their connection with the earth-surface traces. Red stars correspond to the 2021 sequence's main events (Mw≥5.0) and the earth's surface is represented from the SRTM 30m DEM by USGS.*

6.1.3 Results

According to the previously described analysis, the 3D interpretation of the Zarkos Fault Zone comprises 4 main synthetic planes activated during the 2021 earthquake sequence. Furthermore, a good correlation is observed between the 3D surfaces and the traces of the 2D mapping, suggesting the activation of 10 synthetic

possible faults and 3 antithetic. This is observed from the map view of Figure 6.5 where their spatial relationship is rather clear. Notable here is the 2D coverage of the fault surfaces expanding underneath the Southern part of the Domeniko-Amourio basin and Titarisios graben-valley maintaining a straight-line boundary. This fact strengthens the idea that all the fault surfaces are connected to one large surface, probably below the depth of 10-13km.

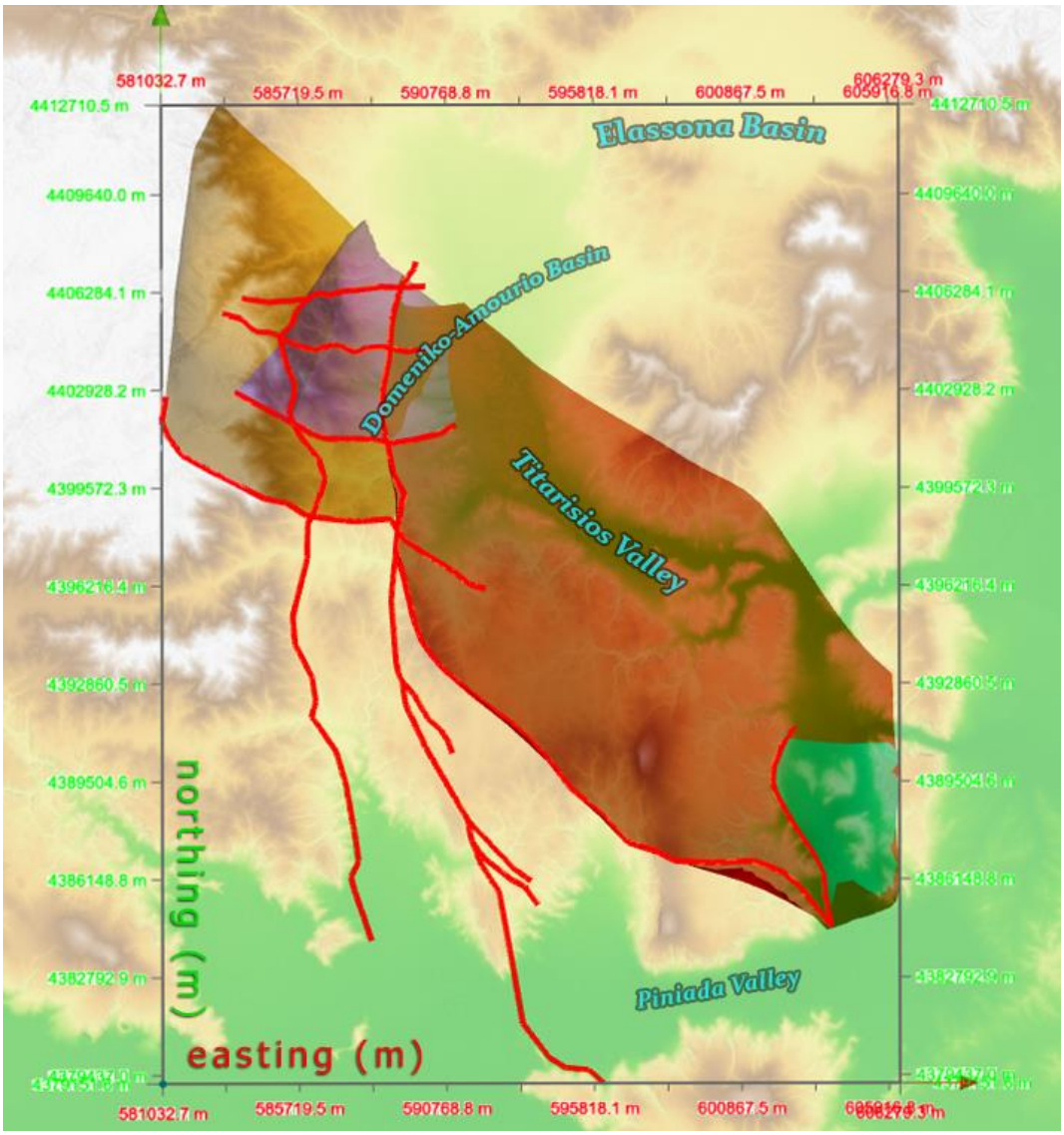

Figure 6.5 *Map view of the Zarkos Fault Zone 3D mode below the transparent area's 30m resolution DEM (SRTM). The red lines correspond to the main fault traces derived from the 2D mapping.*

According to our 3D model's interpretation, the sequence's first 2 mainshocks (M_w 6.3 and M_w 6.0) occurred on a large surface which dips 50^o towards NE. The main surface is 32 km long and 13 km high, while it is steeper in its higher parts. Another two surfaces activated on its edges following the sequence's propagation, as described in detail in the next subsection of the chapter, while the third mainshock corresponds to a new surface at the system's NW tail.

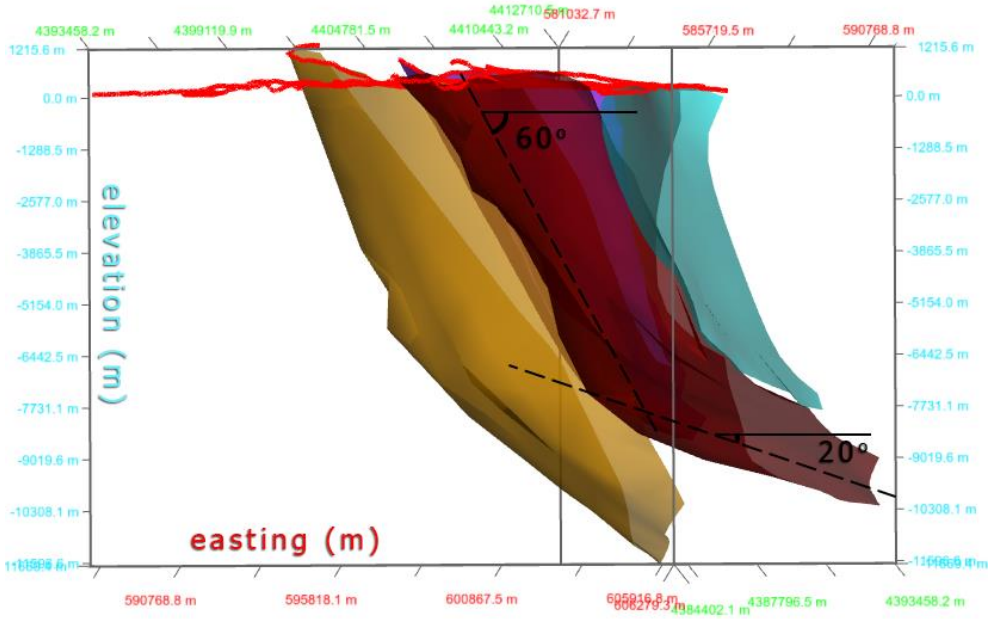

Figure 6.6 *Side view of the Zarkos Fault Zone from the NE side focusing on the geometry of the main fault surface with red colour. The surface is maintained by two parts based on their average angles: the upper part of ~60º angle and the lower of ~20º.*

Another significant feature of the fault surfaces is their clear listric geometry (Williams & Vann, 1987). Figure 6.6 focuses on the main fault surface (No.1 in Figure 6.7) from a side view, showing the angle developed on the surface separating an upper part of a rather steep slope (~60º) where the displacement occurs, and a lower part characterized of a lower angle (~20º). This intense anomaly of the main fault surface is probably associated with the fact that most of the earthquakes occurred on it, confirming the interpretation as the main fault that activated in the 2021 earthquake sequence.

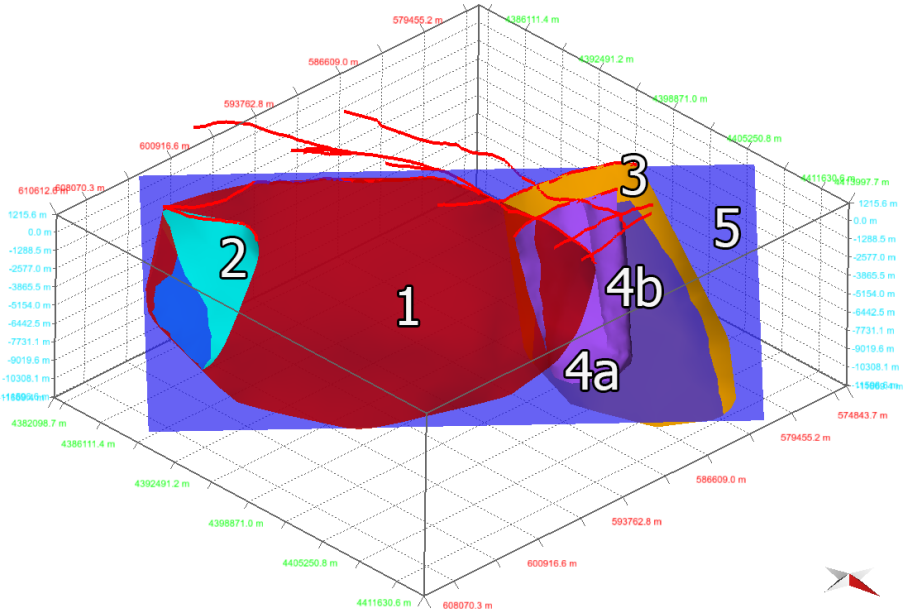

Figure 6.7 *Explanatory image of the 3-dimensional model of Zarkos Fault Zone with the surfaces numbered respectively to their relative activation time (1-4b) along with an average rectangular best-fit plane (5).*

Furthermore, this is an example of how the accuracy of the seismic catalogue may be reflected in the 3D modelling.

Surface	Area(m^2)	Strike(^{o})	Dip(^{o})	Dip Dir. (^{o})	Length(km)	Depth(km)
1	361*10^6	319	50	049	32	11
2	51*10^6	342	65	072	7,6	8
3	190*10^6	311	54	041	10	13
4a	64*10^6	288	58	018	8,1	9,5
4b	36*10^6	010	77	100	4,7	9
5	590*10^6	308	47	039	49,2	12

Table 6.1 *Analytic table of the geometrical characteristics for all the the modelled fault surfaces that are shown in Figure 6.7. The length corresponds to the fault trace length on the earth-surface.*

The whole system has a maximum depth of 13 km and covers a total area of 702 km^2, as calculated from the detailed data in Table 6.1. Although the 3-dimensional model's surfaces are characterized by significant anomalies, their general geometry calculated with the MOVE suite's tools seems rather interesting. Our results are in general agreement with the published focal mechanisms for the main seismic fault surface, giving a mean strike of 317^o (319^o here) and a mean dip of 45^o (50^o here) (Chatzipetros et al., 2021; Ganas et al., 2021).

6.2 Earthquake evolution

The simple 3-dimensional model demonstrated above is useful for the study of the spatiotemporal evolution of the N. Thessaly 2021 earthquake sequence. Unlike the 2-dimensional models, which show only a general propagation of the sequence towards NW, this model can explain it in further detail, based on the fault surfaces relative times of activation and give insights into the segments' interaction with each other.

In particular, the earthquake sequence begins with the occurrence of two strong events of M_w 6.3 and M_w 6.0 on the main fault segment with a primary propagation towards NW. Subsequently, that changes to the opposite direction activating a smaller fault surface without any large events which is a synthetic branch of the main segment at its SE edge. Another two moderate magnitude events occur on the main segment and the sequence propagates again towards NW.

The new synthetic segments that activate at the NW edge of the main surface seem to have a relay-ramp relationship with it. Each of them corresponds with a moderate earthquake of M_w 5.2 and M_w 5.6 (3rd mainshock) while the sequence again propagates bidirectionally.

Studying further these short-timescale interactions between the multiple fault slip surfaces, basic analysis is performed on the earthquake focuses or hypocentres, projecting them on the average rectangle fault surface of the whole system. As shown in Figure 6.8, their density is concentrated inside the fault segments' boundaries that are also projected on the planar surface. The density hotspots seem to follow the general geometry of the faults and the coloured boundaries roughly cross the areas in between them.

Moreover, to distinguish the small-scale interactions between the segments, a simplistic approach of isochrone theory is followed. In this procedure, contour lines are constructed, enclosing all the hypocentres under a specific time threshold. These contour lines confirm the previously mentioned bidirectional propagation of the sequence, and their shapes correlate with the fault segments' boundaries, as shown in Figure 6.9.

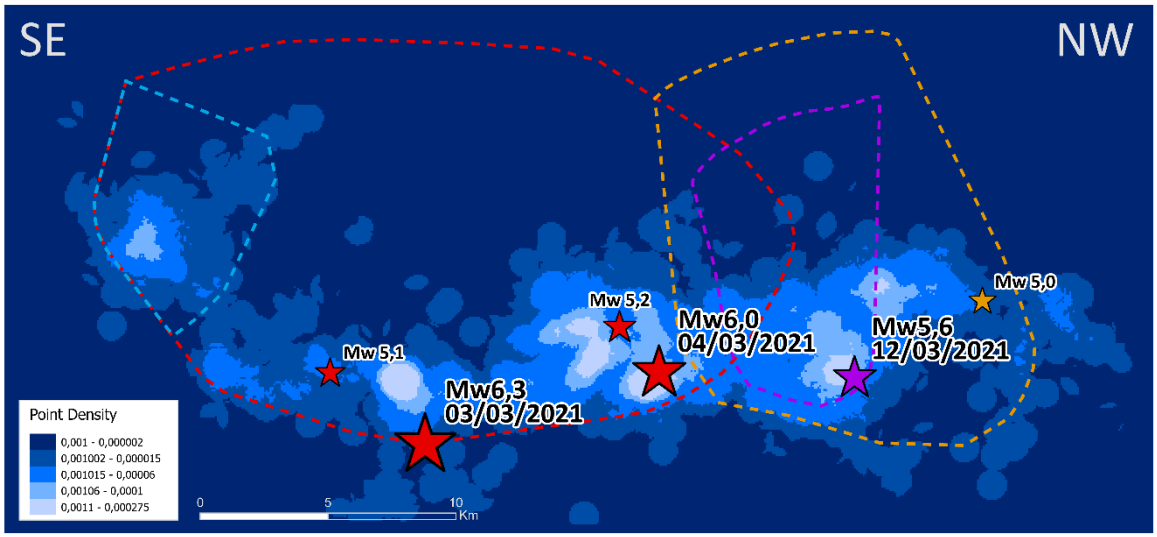

Figure 6.8 *Spatial distribution of the relocated hypocentre's density on the best-fit rectangular plane (No.5 in Figure 6.7). The dashed lines correspond to the boundaries of the 3d model's surfaces projected on the rectangular plane, respectively to their colours in Figures 6.4 and 6.7. The stars correspond to the events M≥5.0 coloured respectively to the surfaces where they occurred.*

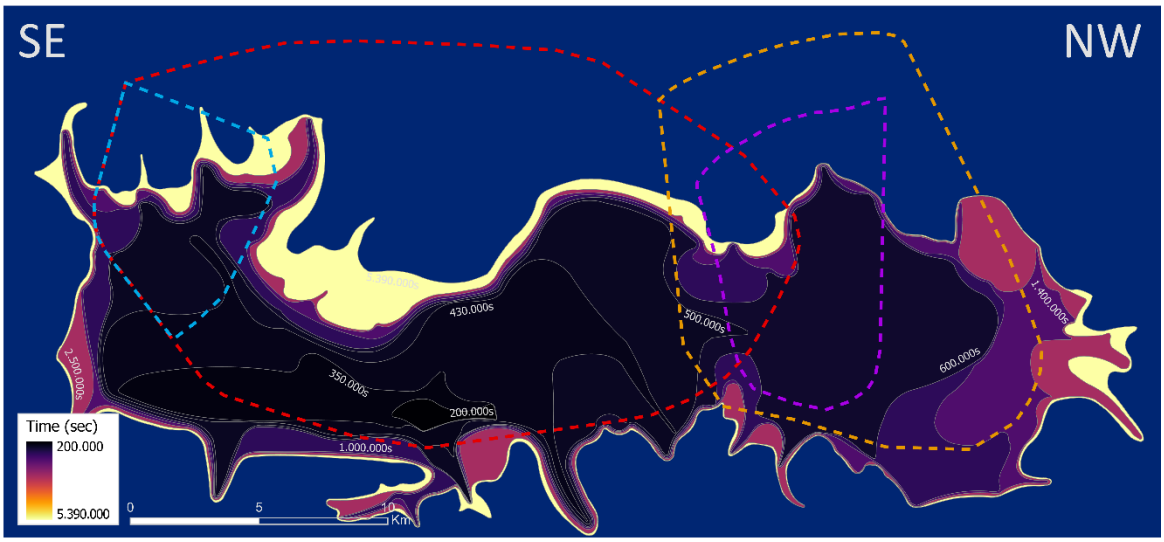

Figure 6.9 *Isochrone contour lines extracted based on the occurrence time of the hypocentres, projected on the best-fit rectangular plane. The dashed lines correspond to the boundaries of the 3d model's surfaces projected on the rectangular plane, respectively to their colours in Figures 6.4 and 6.7.*

6.3 Earthquake scaling and Crustal structure

It is rather obvious from the previous detailed description of the fault model that although the evolution of the earthquake events outlines its boundaries, it continues further beyond them. Analyzing the scaling properties of the earthquakes shall contribute to the understanding of their evolution in a wider space and time. These seismological tools are useful for reviewing our model in terms of physical and geological rationality. Thus, different aspects of the earthquake events' frequency in distribution with parameters such as magnitude, time and depth are examined in the Figures below.

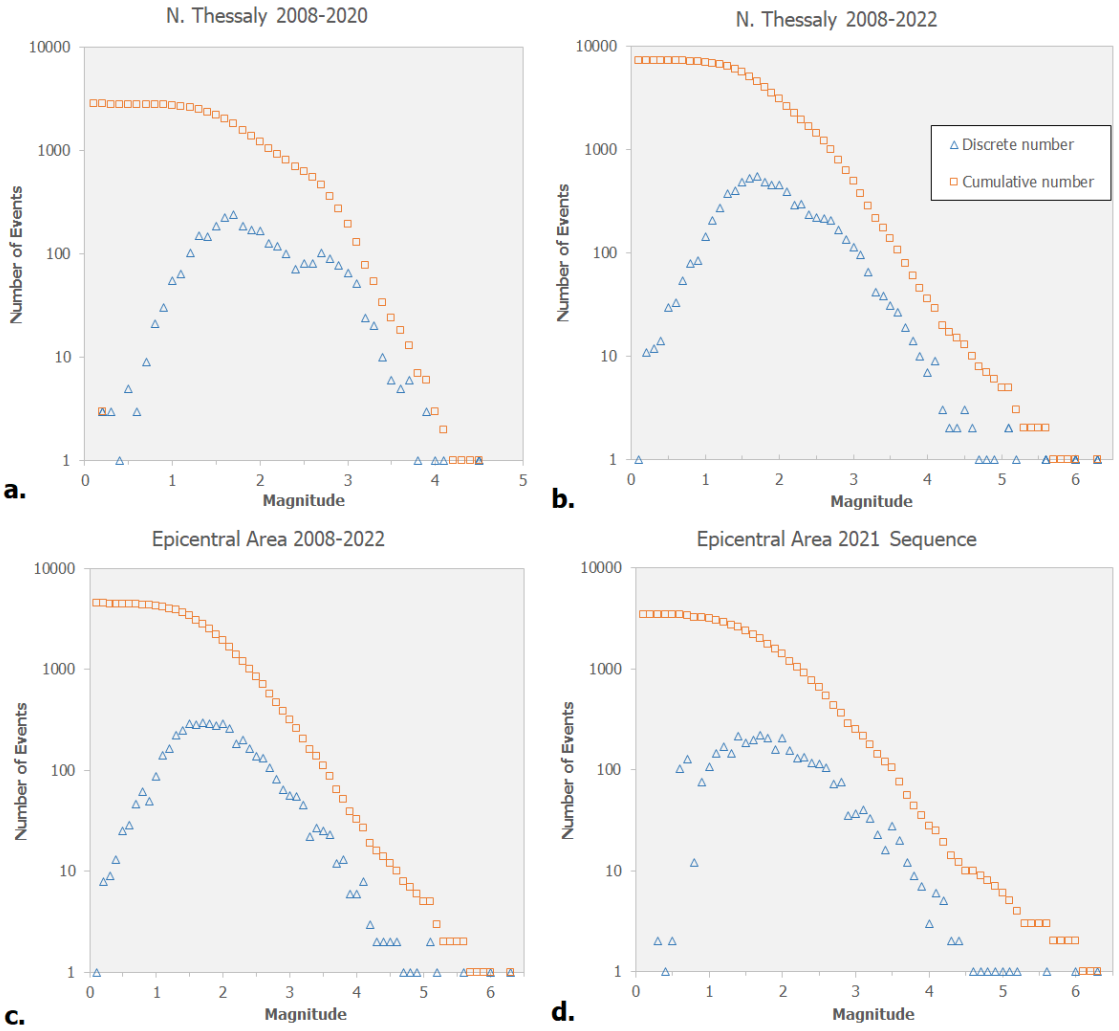

Figure 6.10 *Frequency-Magnitude distribution of the IG-NOA routine catalogue earthquake events of the N. Thessaly area: a) before the 2021 sequence (b≈1,08), b) from 2008 to 2022 (b≈0,99), and of the 2021 epicentral area for: c) the period 2008-2022 (b≈0,90) and d) the 2021 sequence Kassaras et al. (2022) relocated events (b≈0,91). The x-axis bin size is 0,1 in any case.*

The distribution of the earthquakes' magnitude frequency along with their accumulated frequency are correlated amongst the Kassaras et al. relocated catalogue used for this project's 3D model construction and variations of the NOA routine seismic catalogue. As shown in Figure 6.10, there is no significant divergence between the frequency distribution shapes of all conditions, while the 2021 earthquake sequence

seems to create a saturation in the seismicity of both the epicentral and the broader area of N. Thessaly. Notable here is that as the total events increase, their distribution becomes smoother. The approximate b-values extracted from the accumulated frequency distributions vary around 1, obeying the Gutenberg-Richter scaling law (1945).

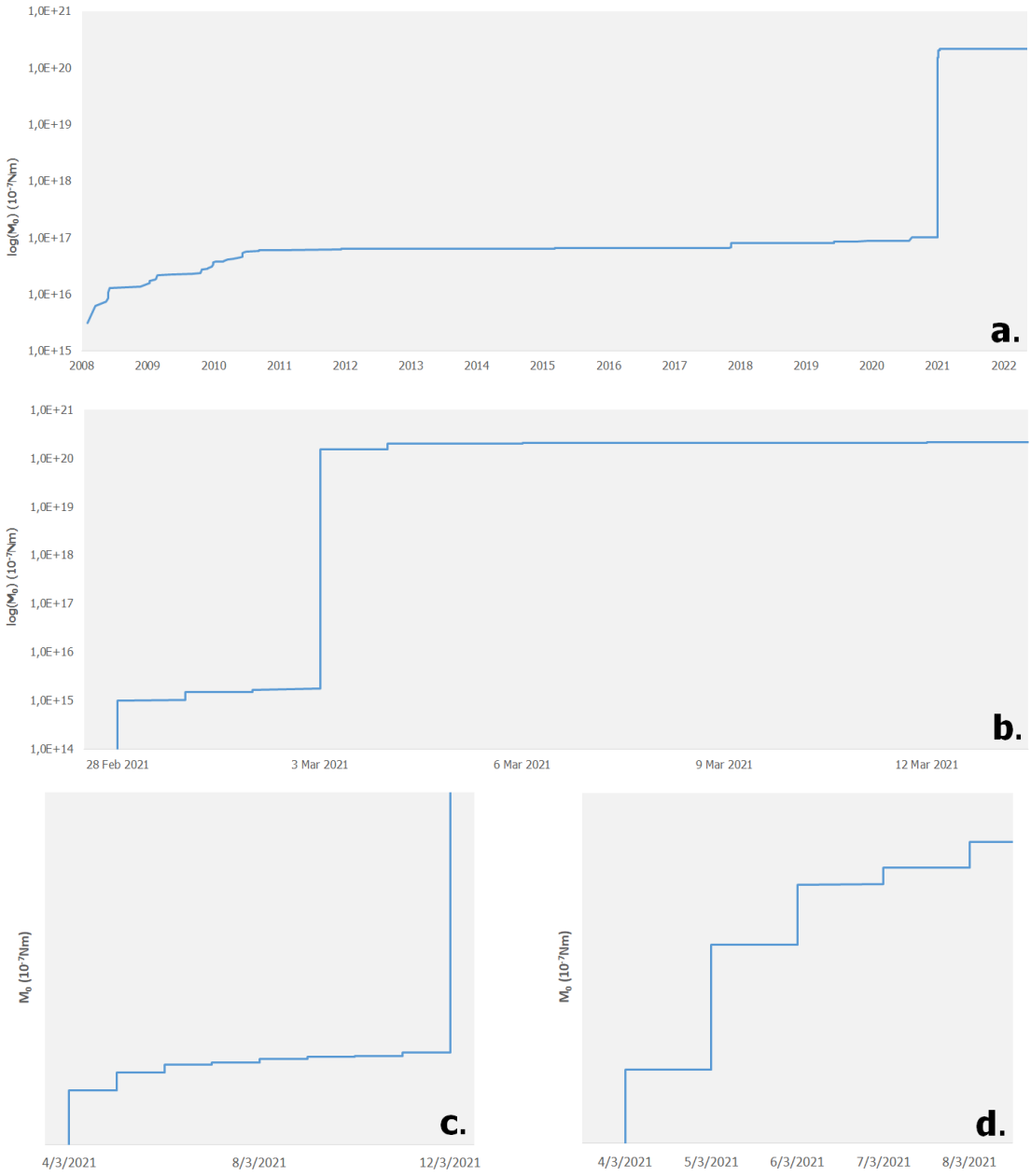

Figure 6.11 *Diagrams showing the accumulate Seismic Moment (M0) for: a) the broader N. Thessaly area from 2008 to 2022 in logarithmic scale, b) the whole relocated catalogue of Kassaras et al. (2022) in logarithmic scale and c),d) the relocated catalogue in smaller time-scales (not in logarithmic scale).*

The most significant and discrete of the changes the N. Thessaly 2021 earthquake sequence entrained to the area is the energy released. The simple distribution of the accumulated seismic moment (M_0) with time in two different scales perfectly displays the

energy stacking in the area's system, as shown in Figure 6.11. The step of the 2021 earthquake sequence corresponds to a major change in the system compared to the smaller steps that appear before and after it. As both axes get shortened zooming in on the 2021 sequence distribution, more steps reveal showing the evolution of the energy stacking during the sequence. A great resemblance of the seismic moment distribution in all scales is observed which is an essential characteristic of critical systems.

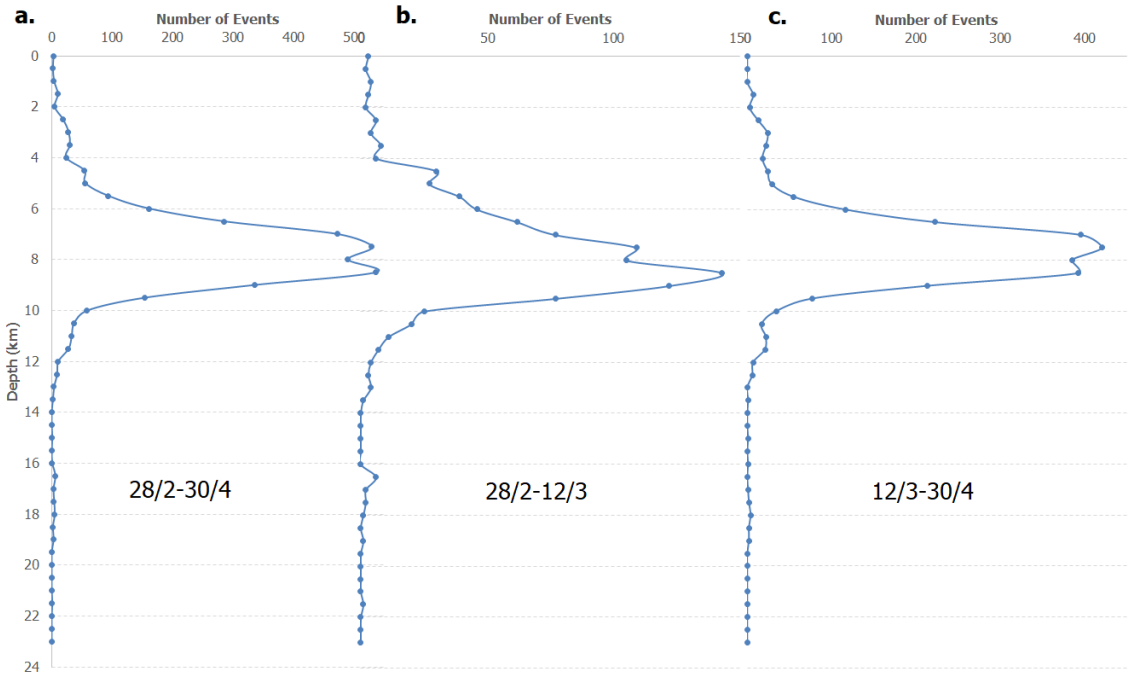

Figure 6.12 *Diagrams showing the frequency-depth earthquake distribution of Kassaras et al. (2022) relocated catalogue for: a) the whole period of the relocated catalogue, b) the main sequence of the N. Thessaly 2021 earthquake sequence, and c) the period of the 2021 aftershock sequence. The Depth bin size is 0,1km.*

The last relationship examined here, which is crucial in seismotectonic, is the distribution of earthquake frequency with depth. As shown in Figure 6.12, the earthquake events used for the 3-dimensional model are more frequent, between 6 and 10 kilometres, with a double peak around 8 km. However, observing the distribution of the main and the aftershock sequence separately, it turns out that the first one corresponds to the peak above 8 km and the second to the peak below it. These peaks are associated with the shear strength and moisture of the upper crust as long as with the transition zone between brittle and ductile deformation (Meissner & Strehlau, 1982).

7. DISCUSSION

7.1 3D model's rationality

The model of the Zarkos Fault Zone that is demonstrated and examined thoroughly in this thesis is proposed to be a complicated system of several surfaces, mainly synthetic. Our model's highlight is the major fault surface that hosted the two mainshocks of M_w 6.3 and M_w 6.0 of the 2021 earthquake sequence due to the geological rationality of its shape and its geometrical agreement with the previous models which is explained below.

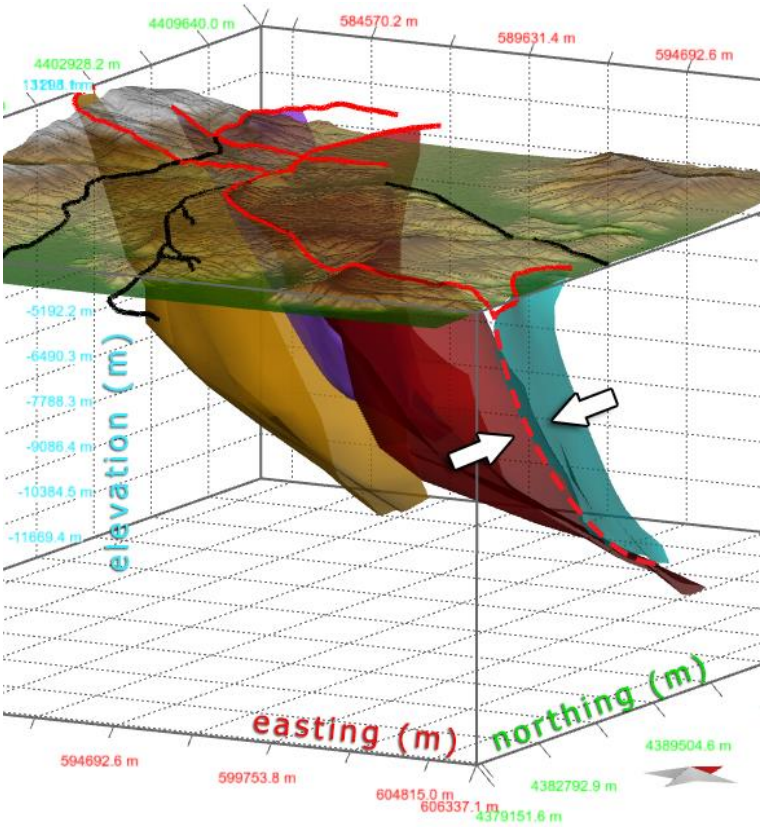

Figure 7.1 *Side view of the 3-dimensional model of the Zarkos Fault Zone's surfaces activated during the N. Thessaly 2021 earthquake sequence, and their connection with the earth-surface traces. The red dashed line highlighted by the two arrows represents the branch line between the fault surfaces of the first and second clusters. The earth's surface is represented from the SRTM 30m DEM by USGS.*

The geometrical characteristics of the major surface which result from a manual process, as explained in Chapter 6, denote the compatibility with the listric fault systems, as described and modelled in literature (McClay et al., 1991; Imber et al., 2003). Figure 6.6 highlights the transition from a low angle surface (~20^o), where the mainshocks and the majority of the events occur, to a steep surface of approximately 60^o. Moreover, the geometry of the other surfaces of the 3D model shows a possible connection with the major or master fault surface in depth (lower than 12km). A typical example of this connection is observed in the 3D model indicating the existence of the undivided surface

in depth. It is the clear branch line that has developed between the fault surfaces of Clusters 1 and 2 in a rather high position that seems to be the tip line of the system.

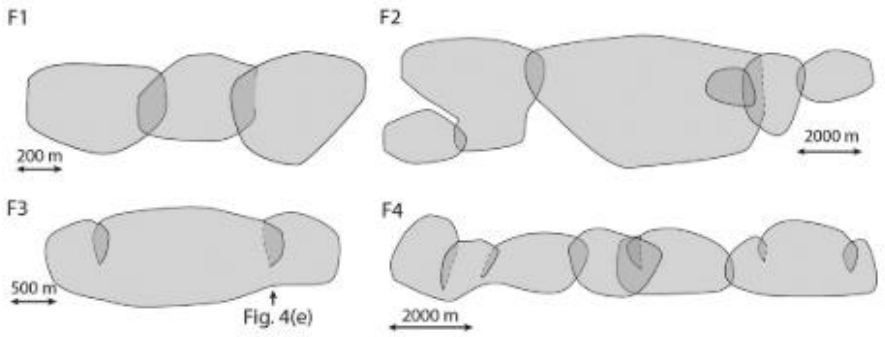

Figure 7.2 *Examples of studied fault zones with relatively simple relay distributions. F1: East African Rift; F2: Barents Sea; F3, F4: Porcupine Basin; All the faults are shown on strike projections at an approximate 1:1 vertical to horizontal scale. Thin black lines represent tip-lines and dotted lines represent branch-lines (Roche et al., 2021).*

Moreover, the shape of the major surface and the Zarkos Fault Zone in general maintain ellipsoidal geometry which is found in several examples of the literature. Figure 7.2 shows four rather simple fault array examples with obvious commonalities with our 3D model. F1 and F2 seem to associate the most with it, while F3 and F4 describe in a rather good way the undivided lower surface that probably continues to a basal detachment surface (Roche et al., 2021).

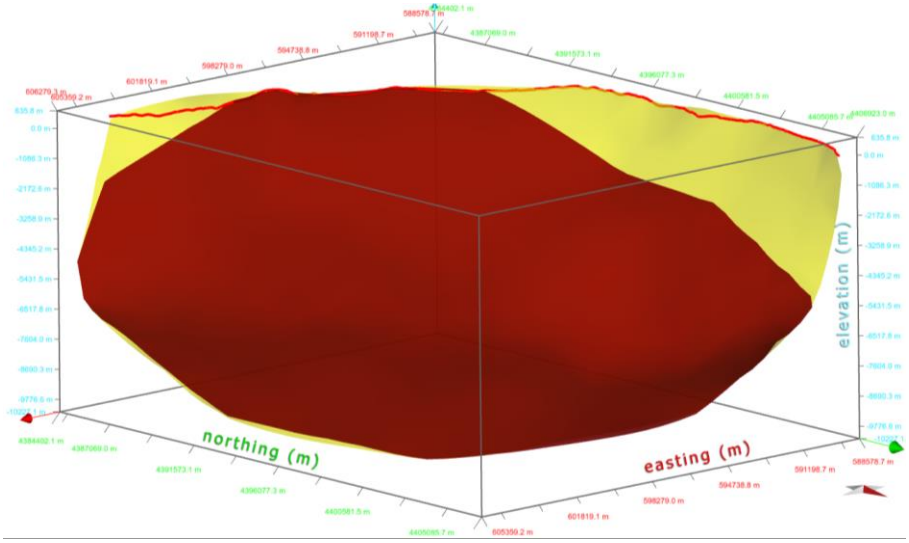

Figure 7.3 *Perspective view of the major fault surface of the Zarkos Fault Zone as a hidden fault with red colour. Yellow coloured parts represent the geometry of the surface according to the model of Figure 6.4.*

The other key feature of the Zarkos Fault Zone geometry is the absence of fault outcrops on the earth's surface, marking the fault as hidden or blind, according to recent literature (Chatzipetros et al., 2021; De Novellis et al., 2021; Galanakis et al., 2021; Ganas et al., 2021; Pavlides & Sboras, 2021; Kontoes et al., 2022; Sboras et al., 2022). However, our 3D model does not show a hidden or blind fault as stated in several publications about the Northern Thessaly 2021 earthquake sequence, mainly because our approach focuses on the correlation and connection of the in-depth major surface with the

corresponding fault trace by the InSAR images. In Figure 7.3, the seismic fault surface is reconstructed considering the geometry of hidden faults on the inclined surface with the fault trace's part where the primary effects are observed at the field.

Rather notable here, is the confirmation of the newly cropped surface's rationality from the seismological perspective by calculating the Seismic Moment (M_0) and Moment Magnitude (M_w) utilizing the different surfaces' dimensions. According to Karakostas et al. (2021), the average slip (D) for the first mainshock is 70cm and for the second 28.3cm, but since in our model these two occur on the same fault surface, the mean value is calculated and equals to 49.15. As shown in Table 7.1, the smaller surface of the hidden fault model combined with the new mean slip results in a Magnitude of M_w=6.42 approaching the M_w=6.3 which corresponds to the generally accepted focal mechanism for the 03/03/2021 mainshock.

A (m^2)	D (cm)	M_0 (dyn/cm^2)	M_w
$361*10^6$	70,00	$8,09*10^{25}$	6,57
$307*10^6$	70,00	$6,88*10^{25}$	6,53
$361*10^6$	49,15	$5,68*10^{25}$	6,47
$307*10^6$	49,15	$4,79*10^{25}$	6,42

Table 7.1 *Faulting parameters of the major or master fault surface as derived from the 3D model of the Zarkos Fault Zone presented in this thesis. The area of the fault surface (A) ranges from $361*10^6 m^2$ for the initial model's surface (yellow surface in Figure 7.3) to $307*10^6 m^2$ for the hidden fault surface (red surface in Figure 7.3), while average slip ranges from 70cm which corresponds to the first mainshock according to Karakostas et al. (2021) to 49.15cm which is the mean value of the two mainshocks. Seismic moment is calculated from the fault dimensions and the average displacement, $M_0=\mu*D*A$ (considering rigidity $\mu=3.3*10^{11}$ dyn/cm^2). The Moment Magnitude is calculated from the Seismic Moment, $Mw = ⅔ \log M_0 – 10.7$.*

7.2 Correlation with previous models

The fault modelling approach of this thesis is based on the seismic data, InSAR images and geotectonic data sources (geological maps, active fault databases etc.) that are interpreted separately and combined with analogue processes resulting to the final product. Therefore, several limitations reflect in it such as the difficulties faced when interpreting the NW part of the hypocentres or earthquake focuses' cloud which maintains a chaotic distribution. Moreover, there are not any surface traces derived either from the morphology or from fault databases to support an antithetic structure compatible with our in-depth clustering and earth-surface co-earthquake displacement. As a result, our model's interpretation is stronger for the major surface (Cluster 1) and its attached surface (Cluster 2) than for the array's NW extension and correlations of it should be made with models derived from the same data and considering the above.

Our final 3D model with the geometry described extensively in previous chapters corresponds with several kinematic and geodetic models proposed by literature. Despite the hidden or blind fault suggestion that was extensively analyzed above, another significant suggestion made by several researchers is the existence of a low-angle or detachment fault (Chatzipetros et al., 2021; Galanakis et al., 2021; Karakostas et al.,

2021; Koukouvelas et al., 2021; Pavlides & Sboras, 2021; Sboras et al., 2022). As described previously, the geometry of our 3D model indicates the merging of the fault surfaces in depth following the major one that transitions to a ~20^{o} angle and possibly continues to a basal detachment surface. This is also described rather good by the schematic profile of Figure 7.4 that shows it at 10km underlying all the major faults of the Thessaly area (Chatzipetros et al., 2021; Pavlides & Sboras, 2021; Sboras et al., 2022).

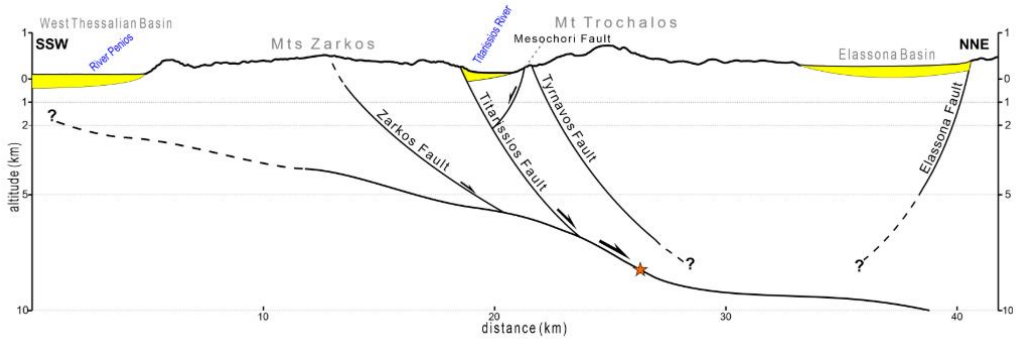

Figure 7.4 *Schematic profile showing the proposed tectonic model for the first mainshock (3 March, orange star indicates the hypocentre). Modified after Chatzipetros et al. (2021) and Pavlides & Sboras (2022) (Sboras et al., 2022).*

Examining the relevance of the model itself with the previous ones for the Zarkos Fault Zone, shows a general agreement with several studies, especially those utilizing the same relocated seismic catalogue (De Novellis et al., 2021; Kassaras et al., 2022; Michas et al., 2022; Yang et al., 2022; Li et al., 2023). These suggest the occurring of the earthquake sequence on a conjugate fault system, starting on two synthetic surfaces and crossing over to an antithetic one at the time of the third mainshock (12/03/2021, M_w5.6), as shown in Figure 7.5. On the other hand, our model proposes the merge of the two synthetic surfaces which maintain observable kinematic relationship. Our interpretation approach on the seismic data leads to a major or master fault surface that maintains an average dip of 50^{o} approximately, which is also observed in the clustering correlation with the primary one by Kassaras et al. (2022) in Figure 7.6.

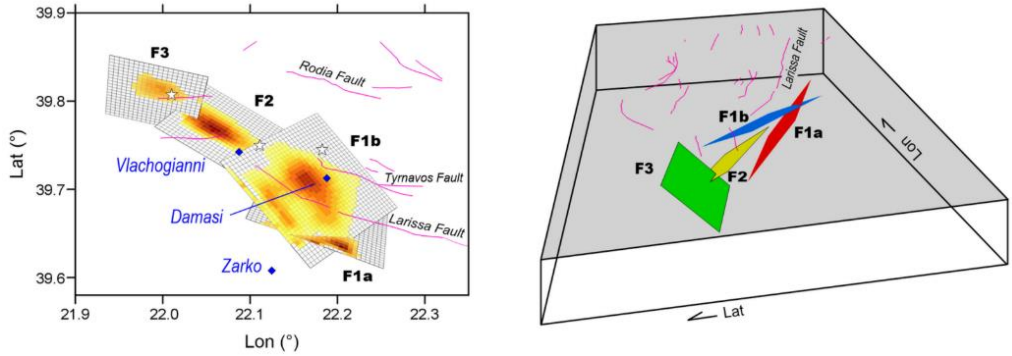

Figure 7.5 *Geodetic model of the Northern Thessaly 2021 earthquake sequence based on the Kassaras et al. (2022) relocated seismic catalogue (De Novellis et al., 2022).*

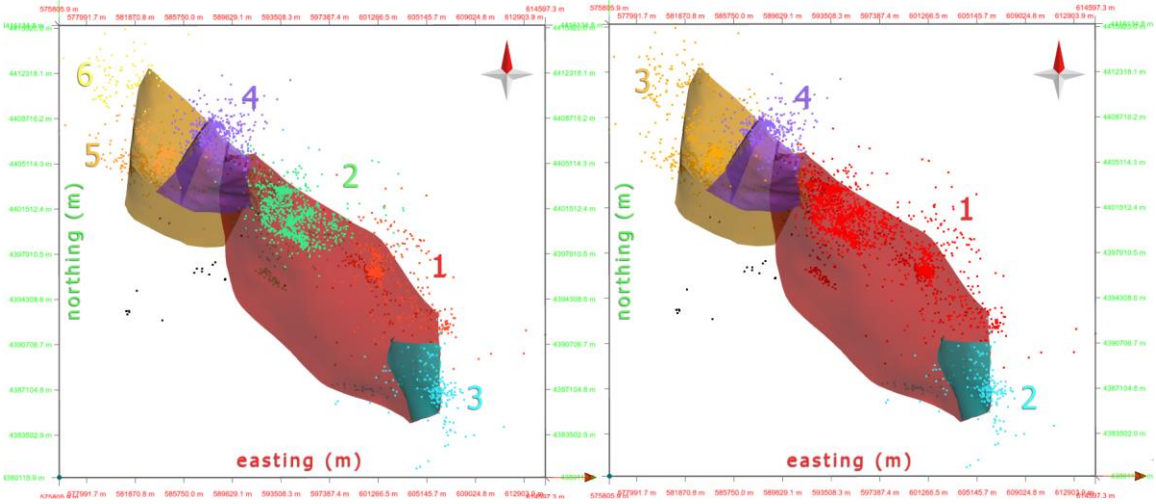

Figure 7.6 *Map view of the Zarkos Fault Zone 3-dimensional model with the scattered hypocentres, coloured according to Kassaras et al. (2022) who distinguishes 6 clusters on the left and this thesis' clustering on the right (4 clusters). This thesis' clustering seems to be a simplified version of the older one, with minor differences at the clusters' boundaries.*

The main argument that rises between the different approaches is focused on the fault surface that corresponds with the 3rd mainshock and its dip direction. Based on detailed InSAR data analysis, most of the model interpretations suggest a fault surface that dips towards SW (F3 in Figure 7.5), instead of a NE-dipping one, as demonstrated in our model (No4 in Figure 7.6). Nevertheless, the aspect of an absolute synthetic fault system is supported by the fault slip model of Figure 7.7 (Kontoes et al., 2022) which proposes a NE dipping surface for the third mainshock as preferable to an antithetic. It has to be mentioned here, that another approach, based on InSAR data analysis, suggests the activation of antithetic fault surfaces for both the 2nd and 3rd mainshocks as shown in Figure 7.8 (Ganas et al., 2021; Mouslopoulou et al., 2022). A possible explanation on this variation of the fault models may be associated with emphasis given to the data that the particular researcher is rather confident with or the data itself and the analysis methods used.

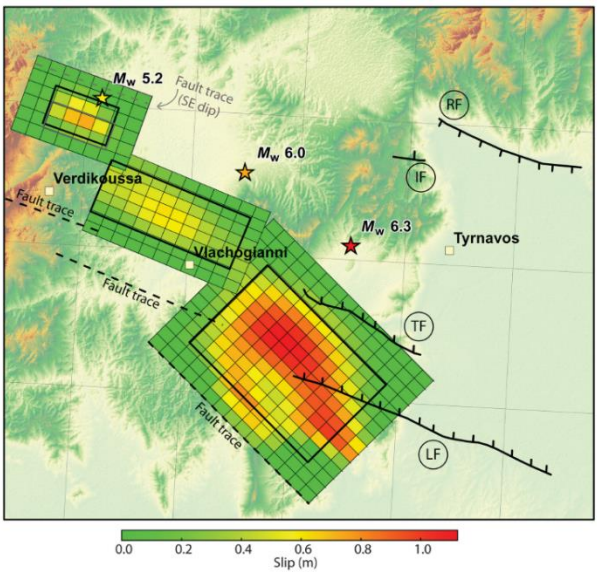

Figure 7.7 *Slip model distributions in geographic view, for the mainshock and the two aftershocks. The third source solutions for the two fault planes are reported in black for the preferred option (northeast dipping) and gray for the alternative solution (southwest dipping). The same scale bar applies to all the slip distributions. Fault patches are 1 × 1 km; slip distributions are completed with the vertical depths and focal. LF, TF, RF, and IF faults are added according to Caputo et al. (2004). The stars indicate the event epicenters (Kontoes et al., 2022).*

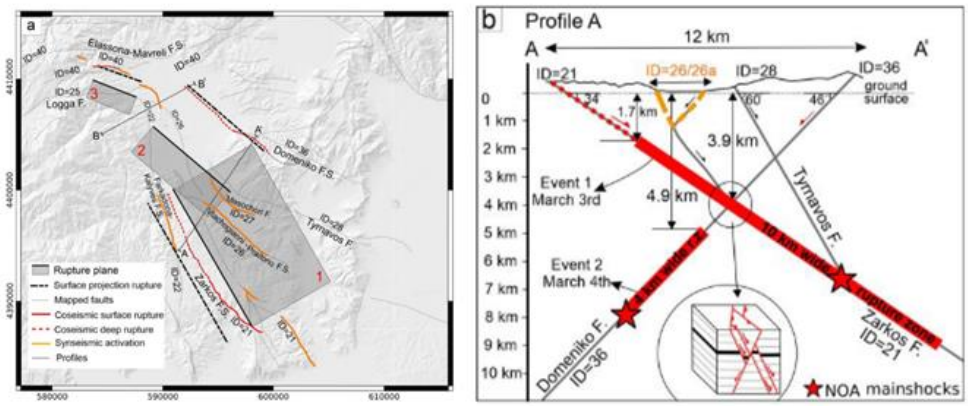

Figure 7.8 *(a) Map view of the kinematic rupture models of the three mainshocks (see 1-3 grey rectangles) superimposed onto a hillshade. Thick black line on each rectangle marks the uppermost extend of the rupture plane while its surface projection is indicated with a dashed black line. Fine black lines indicate mapped faults, while fault sections are colour-coded according to rupture style (coseismic, syn-seismic, etc). A-A' and B-B' mark the locations of depth profiles across key faults (and their intersections), schematically illustrating the geometric relationships of faults/ruptures associated with the first two mainshocks. (b) Schematic profile of A-A'. Fault and rupture plane geometries/dimensions are tailored to the values of the preferred kinematic models and to field measurements (i.e. for faults with IDs 28, 26, 26a, 22). Syn-seismic slip information on the Mesochori Fault (ID=26a) comes from Koukouvelas et al. (2021). Topography is derived from the DEM. Colour coding on faults of both profiles follow that of (a) (Mouslopoulou et al., 2022)*

7.3 Seismic catalogues' correlation

As mentioned before, the data utilized in each case determine the produced model and variations of the different data may lead to variations in the models. Moreover, variations emerge due to the analysis of the primary data, the software and the chosen parameters utilized for the catalogue's relocation. The Depth-Frequency distribution is chosen as the most suitable for correlating the different catalogues, as shown in Figure 7.9. Interesting is the fact that the Depth-Frequency distribution reveals small differences even among the catalogues that result from the same primary data. Furthermore, the chosen period of the main earthquake sequence is different in all the relocated catalogues (Figure 7.9-f.).

The most significant information that results from this correlation among the diagrams of Figure 7.9 is that all of them show a maximum of events at around 10km with minor differences. Therefore, this confirms the association of the seismicity with the Brittle to Ductile deformation boundary, which variates from 12 to 18 km for Central Greece according to the rheological profile curves constructed by Maggini & Caputo (2020) and Tolomei et al. (2021) (Figure 7.10). Moreover, the Northern Thessaly 2021 earthquake sequence relocated catalogues generally agree with the standards of medium heat-flow areas (Meissner & Strehlau, 1982; Blundell et al., 1992).

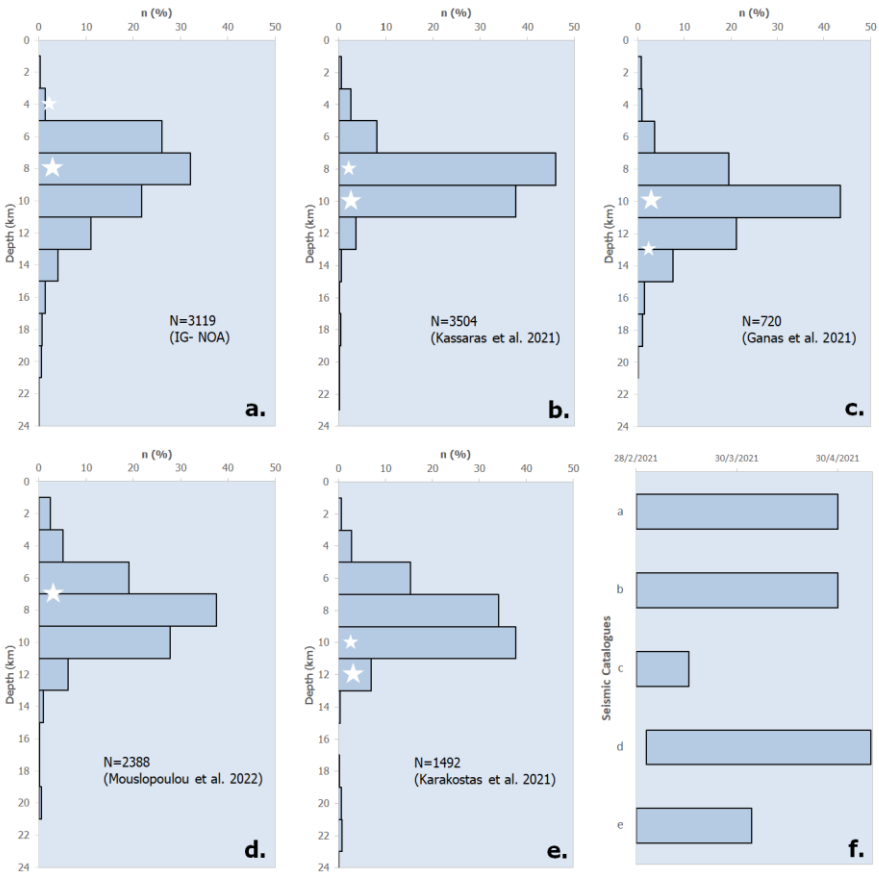

Figure 7.9 *Depth-frequency distribution of hypocentres for the N. Thessaly 2021 earthquake sequence with a bin size of 1km for the: a) IG-NOA routine catalogue, b)Kassaras et al. (2021) relocated catalogue, c) Ganas et al. (2021) relocated catalogue, d) Mouslopoulou et al. (2022) relocated catalogue and e) Karakostas et al. (2021) relocated catalogue. f) The time-period variation of the catalogues a)-e). White stars correspond to the two mainshocks of the 2021 sequence (Mw6.3 and Mw6.0).*

The question that rises from the above-mentioned correlations is whether these variations can be observed in a geospatial distribution of the events. In order to answer this question, the earthquake focuses or hypocentres of the Ganas et al. (2021) and Karakostas et al. (2021) relocated catalogues are distributed on the Kassaras et al. (2021) relocated catalogue that is used in this thesis. As shown in Figure 7.11, the events' distribution does not variate a lot, but the relevance of the Kassaras et al. (2021) catalogue with Ganas et al. (2021) due to the same primary data used is obvious. On the contrary, Karakostas et al. (2021) catalogue maintains a denser distribution than the others which is still aligned with them, but slightly offsets towards NE.

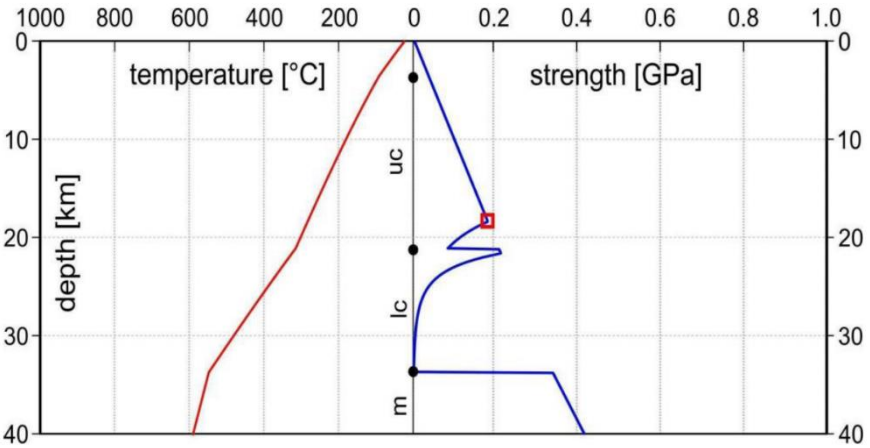

Figure 7.10 *Representative rheological profile for the epicentral area. The blue line represents the strength envelope, the red line the corresponding geothermal gradient, while the red square indicates the BDT. Abbreviations: uc—upper crust; lc—lower crust; m—mantle (Tolomei et al., 2021).*

The rather good correlation of the relocated seismic catalogues' 2D distribution indicates a correlation with the 3D model of the Zarkos Fault Zone that is demonstrated in this thesis. An attempt at the correlation in 3 dimensions between the relocated catalogue of Karakostas et al. (2021) and our 3D model is shown in Figure 7.12. The distributed earthquake hypocentres with black colour are generally aligned with our 3D model and seem to bound the fault surfaces, especially the major one and surface of the 2nd cluster. This cluster is also observed at the SE tail of the 2D distribution that is shown in Figure 7.11 supporting our interpretation of the corresponding fault surface (cyan surface in Figure 7.12) that is attached to the tip line of the major one.

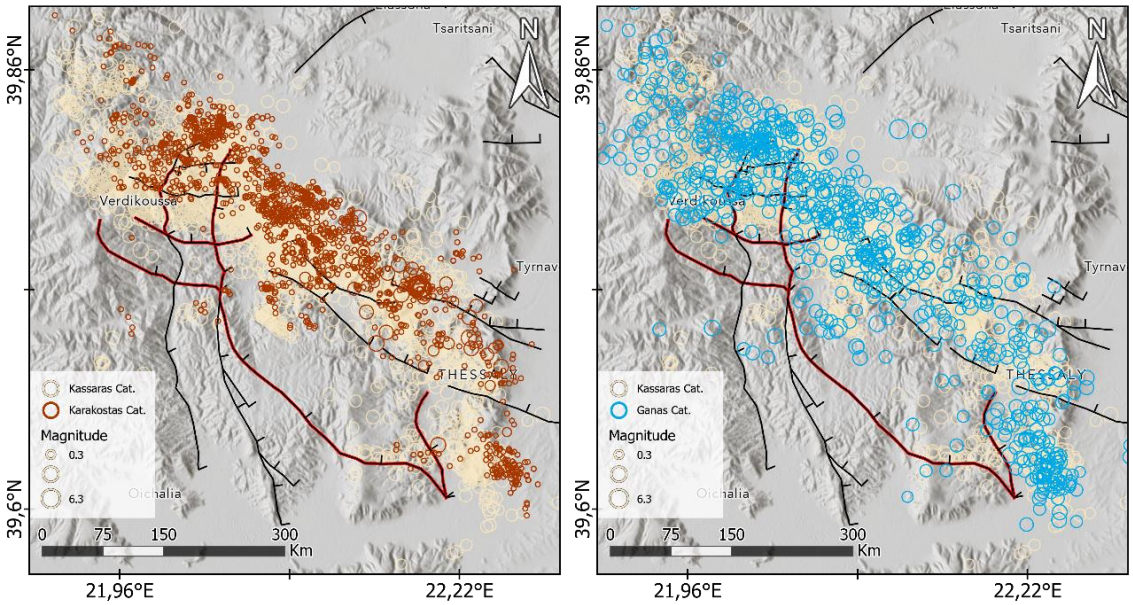

Figure 7.11 *Map view of the Northern Thessaly 2021 earthquake sequence epicentral area with the Zarkos Zarkos Fault Zone and the other faults of the area according to NOA active faults v.4.0 (Ganas, 2020), while the red stroked faults correspond to the traces of the 3D fault model of this thesis. In the left map, the epicentres of Karakostas et al. (2021) relocated catalogue (red circles) are distributed on the Kassaras et al. (2021) catalogue (pale yellow circles), while in the right map the epicentres of Ganas et al. (2021) relocated catalogue (cyan circles) are distributed on it.*

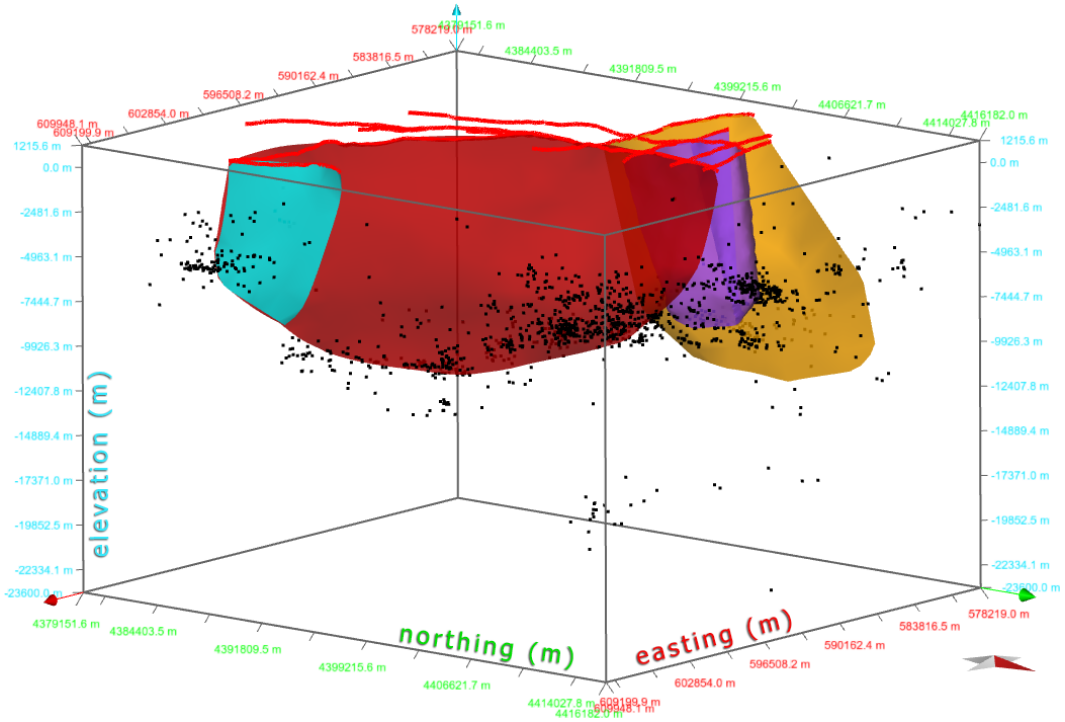

Figure 7.12 *Perspective view of the 3-dimensional model of the Zarkos Fault Zone's surfaces activated during the N. Thessaly 2021 earthquake sequence, and their connection with the earth-surface traces. Black points correspond to the hypocentres of earthquake focuses of Karakostas et al. (2021) relocated seismic catalogue.*

7.4 Stress transfer of Zarkos Fault Zone

According to the stress field models of the Northern Thessaly 2021 earthquake sequence, there is a stress load up towards NW and SE, as shown in Figure 7.13 (Chatzipetros et al., 2021) (Chatzipetros et al., 2021; Karakostas et al., 2021; Kassaras et al., 2021; Michas et al., 2022; Li et al., 2023). This transfer of stress raises questions about the general balance of stresses gathered in other areas' active faults. Since the SE stress load-up corresponds to the Larissa Plain which is a well-studied area for its neotectonics, the NW part should be investigated. The area NW of the Zarkos Fault Zone and West of the Elassona Basin is a mountainous area with no information about active faults. The fault model suggested by Mouslopoulou et al. (2022) points to that area interpreting a new fault zone as the extension of the Elassona Fault.

Figure 7.14 shows the new fault zone in correlation with the 2D model of the Zarkos Fault Zone presented in this thesis. The proposed extension of the Elassona Fault towards WSW with an approximate length of 30km is similar to the Zarkos Fault Zone in its shape and basinal margin position. According to the interpretation (Mouslopoulou et al., 2022), it was partially activated during the 2021 earthquake sequence, associated mainly with the third mainshock (M_w5.6) near Verdikoussa village.

Furthermore, according to the historical seismic record, a strong earthquake on November 17, 1901, caused damages to the villages of Verdikoussa with the collapse of

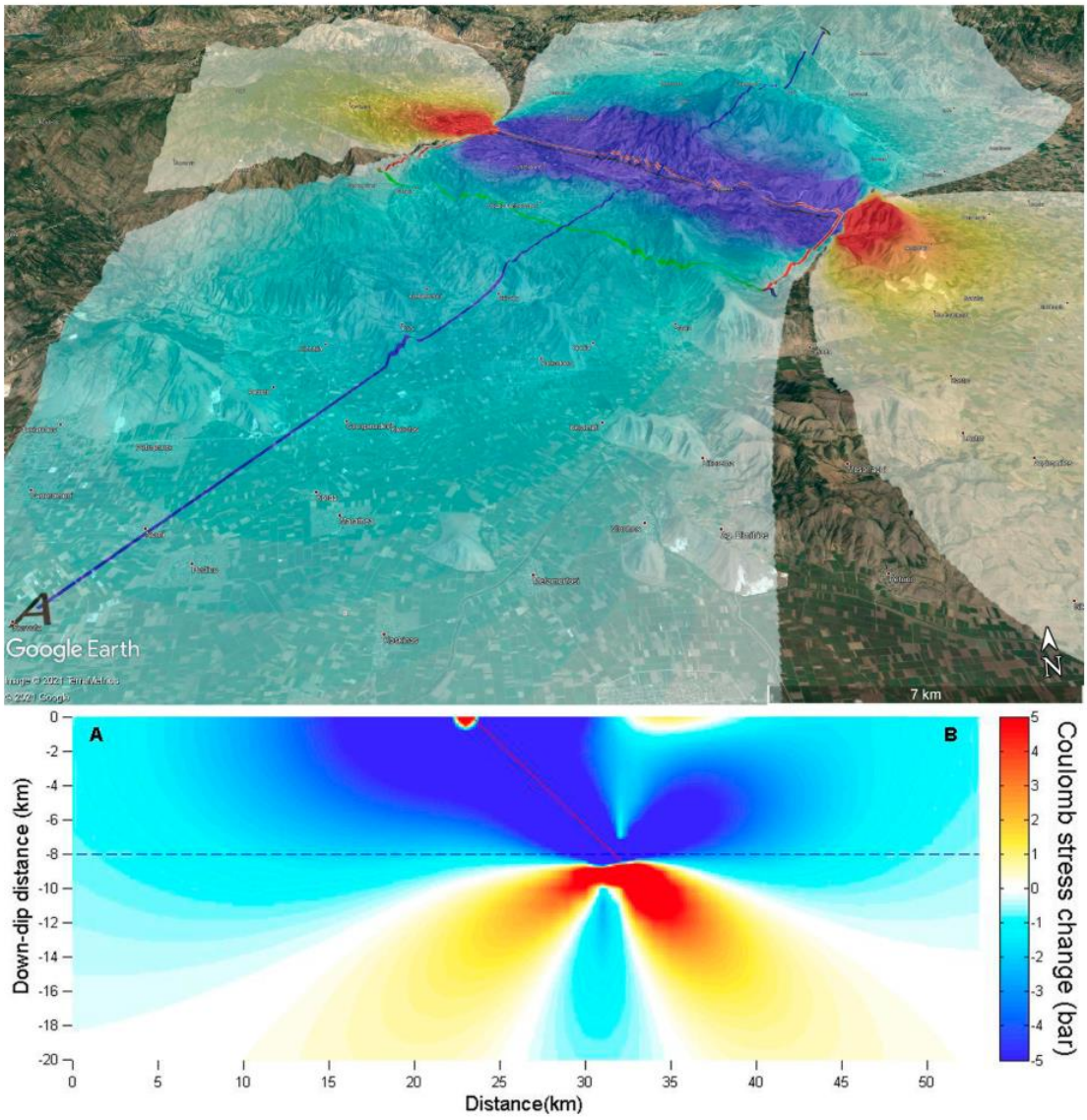

Figure 7.13 *The seismic fault model and the Coulomb static stress changes in horizontal (top) and vertical (bottom) sections that caused for receiver-faults similar to the first mainshock's source-fault at the depth of 8 km. Modified from Chatzipetros et al. (2021)(Sboras et al., 2022).*

several buildings and ground subsidence phenomena. This is a significant clue for the possible activation of the Elassona Fault's extension and the relationship between the two earthquake sequences of 1901 and 2021. Moreover, the village of Verdikoussa is situated on the footwall area of the Zarkos Fault (red-stroked line) and the footwall of the Elassona Fault extension (yellow-stroked lines). This fact may explain the significant damage difference the village received during the two earthquake sequences, indicating the need for geological research on the Elassona Fault Zone.

Nevertheless, this new fault is a suggestion indicated by satellite data analysis and therefore, may not support a solid theory about the stress transfer direction in any case. In order to make safe conclusions about the existence of a separate fault zone in the area NNW of the Zarkos Fault Zone, strong evidence is needed through detailed fieldwork.

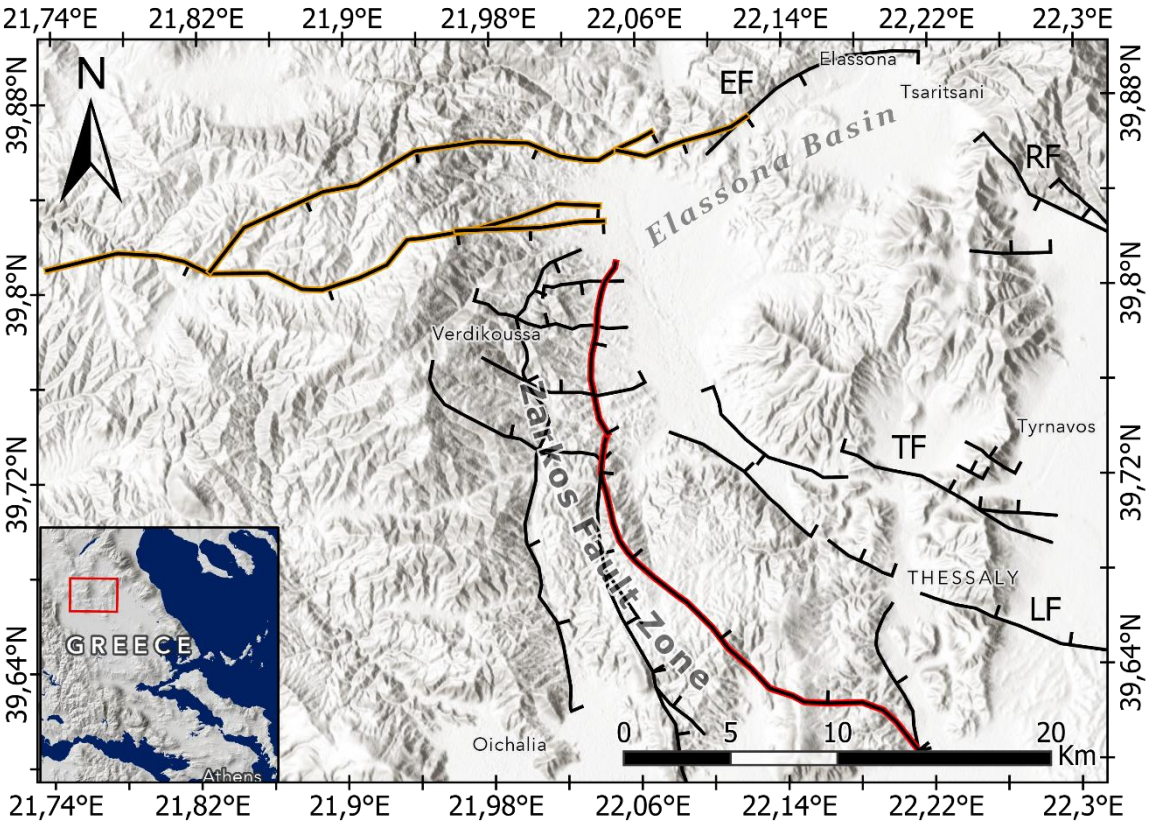

Figure 7.14 *Map of the broader epicentral area of the Northern Thessaly 2021 earthquake sequence distributing the Zarkos Fault Zone model proposed by this thesis (Red stroked line corresponds to its major fault trace) and the Extensive Elassona Fault Zone (yellow stroked lines), as it is suggested by Mouslopoulou et al. (2022). LF, TF, RF and EF faults are added according to Ganas et al. (2020).*

7.5 The Role of inherited structures

As shown in several maps presented in this thesis, the Zarkos Fault Zone which was activated during the Northern Thessaly 2021 earthquake sequence maintains an NW-SE trend, which corresponds to a NE-SW trend of extension. This fact is contrary to what is considered about the variations of the stress field due to the migration of the Hellenic orogen which has led to an N-S trending extension, active since the Middle Pleistocene, as described in Chapter 3. The Zarkos Fault Zone belongs to a former extensional field that was active during Oligocene-Miocene.

According to the literature, the NE-SW extensional field of Oligocene-Miocene corresponds to the first stages of post-orogenic collapse. This was a period of crustal thinning due to rheological softening and upraised domes that resulted in the formation of detachment faults and exhumation of lower units as tectonic windows (e.g. the tectonic windows of Kranea and Olympos) (Sfeikos et al., 1990; Kilias et al., 1991; Doutsos et al., 1993; Schermer, 1993). The structures that are related to this tectonic stage were considered inactive before the Northern Thessaly 2021 earthquake sequence, but now it seems that the previous practices about the characterization of a fault as active should be revised.

8. CONCLUSIONS

1. Our interpretation suggests a surface of 32km length and 50º NE-dipping, as the major surface of the Zarkos Fault Zone, where the M_w6.3 and M_w6.0 events occurred on 3 and 4 March, respectively. The surface is attached with a branch line at its SE tip with a smaller surface, while the 3D model comprises two more fault surfaces at the NW part of the major one possibly merging to an undivided surface below the depth of ~12km.

2. The Zarkos Fault Zone maintains a listric fault geometry with a lower part of ~20º that possibly extends to a basal detachment surface that lies underneath the area's major active faults. Moreover, the ellipsoidal shape of the major surface's elevation profile along with the also ellipsoidal shape of the 3D fault surfaces correspond with the literature examples of normal active fault zones and the fault growth theory.

3. Rather interesting is the absence of typical morphological expression of the Zarkos Fault Zone nor notable anomalies on the hydrographic network of the 2021 epicentral area, according to the attempted morphotectonic analysis presented in this thesis.

4. The Northern Thessaly 2021 earthquake sequence shows a bidirectional propagation on the 3D model of the Zarkos Fault Zone demonstrated in this thesis. The isochrone contour lines distributed on the average rectangular best-fit plane describe in detail the events' evolution propagating towards SE and NW along the main strike of the fault zone.

5. The density of the earthquake focuses or hypocentres distributed on the average rectangular best-fit plane are focused on the boundaries of our 3D model's fault surfaces, with all the hotspots to be situated inside them and less density at the areas around the possible branch lines between the surfaces.

6. The Depth-frequency distribution shows a double peak at 8km that seems to split to a peak below 8km and one above it as the event period is divided into a main and an aftershock sequence period, respectively. The seismicity cutoff at 10-12km corresponds to the rheological profiles of the area and with other examples of shallow-depth earthquakes in areas of extensional tectonic regime.

7. Our 3D model of the Zarkos Fault Zone is in general agreement with the previously proposed models, supporting the theory of a hidden low-angle fault. Furthermore, it shows a rather good correlation with the models that are based on the same relocated catalogue with the main argument to be the dip direction of the fault surface that corresponds to the 3rd mainshock of 12 March 2021 (M_w5.6).

8. Correlations between several seismic catalogues of different primary data and chosen periods show general agreement on the maximum peaks (~10km) and the seismicity cutoffs (~12-14km), supporting the association between seismicity and the

Brittle to Ductile deformation boundary which variates at 12-18km according to the literature.

9. The geospatial distribution of the relocated catalogues' epicentres provides another indication of their rather good agreement with each other and with our 2D model of the Zarkos Fault Zone confirming our clustering, especially for the first and second clusters.

10. The hypocentres or earthquake focuses of the relocated seismic catalogue that shows the best correlation with our 2D model of the Zarkos Fault Zone are distributed in the 3D environment showing a rather good correlation with the 3D model too.

11. The stress load-up towards NW along with the 1901 Verdikoussa earthquake, and geodetic analysis and interpretations of previous work may indicate the existence of another hidden active fault, a possible extension of the Elassona Fault towards the West maintaining similarities with the Zarkos Fault Zone. Nevertheless, without a detailed field survey, there are not any safe conclusions that can be made about this.

12. Zarkos Fault Zone is composed of both W-E, WNW-ESE, NW-SE and N-S trending faults highlighting the contribution of multiple deformational phases to the growth of an active fault system and the crucial role of inherited structures in active tectonics.

13. The major or master fault surface of the Zarkos Fault Zone 3D model on which the 1st and 2nd mainshocks occurred maintains a general NW-SE trend corresponding to the NE-SW extension of Pliocene-Early Pleistocene but is also related to structures inherit from Oligocene-Miocene exhumation with low-angle detachment faults to the development of several tectonic windows in the broader area (e.g. Olympos and Kranea areas).

14. Inherited faults from the so-called inactive stress fields that are situated near inhabited areas should be closely investigated since the example of the Northern Thessaly 2021 earthquake sequence highlights their potential activation with the occurrence of strong earthquake events.

REFERENCES

Aki, K. (1966). Generation and Propagation of G Waves from the Niigata Earthquake of June 16, 1964. In *Bulletin of the Earthquake Research Institute* (Vol. 44, pp. 73–88).

Anders, M. H., & Schlische, R. W. (1994). Overlapping faults, intrabasin highs, and the growth of normal faults. *Journal of Geology*, *102*(2), 165–180. https://doi.org/10.1086/629661

Baker, V. R. (1977). Stream-channel response to floods, with examples from central Texas. *Geological Society of America Bulletin*, *88*(8), 1057. https://doi.org/10.1130/0016-7606(1977)88<1057:SRTFWE>2.0.CO;2

Blundell, D. J., Freeman, R., Mueller, S., & Button, S. (1992). *A continent revealed: The European Geotraverse, structure and dynamic evolution*. Cambridge University Press.

Bormann, P., Wendt, S., & DiGiacomo, D. (2013). Seismic Sources and Source Parameters. In P. Bormann (Ed.), *New manual of seismological observatory practice 2* (pp. 1–259). https://doi.org/https://doi.org/10.2312/GFZ.NMSOP-2_ch3

Burbank, D. W., & Anderson, R. S. (2013). Tectonic Geomorphology, Second Edition. *Environmental & Engineering Geoscience*, *19*(2), 198–200. https://doi.org/10.2113/gseegeosci.19.2.198

Caputo, R. (1995). Inference of a seismic gap from geological data: Thessaly (Central Greece) as a case study. *Annals of Geophysics*, *XXXVIII*(1).

Caputo, R., Bravard, J.-P., & Helly, B. (1994). The Pliocene-Quaternary tecto-sedimentary evolution of the Larissa Plain (Eastern Thessaly, Greece). In *Geodinamica Acta* (Vol. 7, Issue 4, pp. 219–231). https://doi.org/10.1080/09853111.1994.11105267

Caputo, R., Chatzipetros, A., Pavlides, S., & Sboras, S. (2012). The greek database of seismogenic sources (GreDaSS): State-of-the-art for northern greece. *Annals of Geophysics*, *55*(5), 859–894. https://doi.org/10.4401/ag-5168

Caputo, R., Helly, B., Pavlides, S., & Papadopoulos, G. (2004). Palaeoseismological investigation of the Tyrnavos Fault (Thessaly, Central Greece). *Tectonophysics*, *394*(1–2), 1–20. https://doi.org/10.1016/j.tecto.2004.07.047

Caputo, R., Helly, B., Pavlides, S., & Papadopoulos, G. (2006). Archaeo- and palaeoseismological investigations in Northern Thessaly (Greece): Insights for the seismic potential of the region. *Handbook of Environmental Chemistry, Volume 5: Water Pollution*, *39*(2), 195–212. https://doi.org/10.1007/s11069-006-0023-9

Caputo, R., Helly, B., Rapti, D., & Valkaniotis, S. (2021). Late Quaternary hydrographic evolution in Thessaly (Central Greece): The crucial role of the Piniada Valley. *Quaternary International*. https://doi.org/10.1016/j.quaint.2021.02.013

Caputo, R., & Pavlides, S. (1991). Neotectonic setting and evolution of Thessaly. *Bull. Geol. Soc. Greece*, *XXV*(3), 120–133.

Caputo, R., & Pavlides, S. (1993). Late Cainozoic geodynamic evolution of Thessaly and surroundings (central-northern Greece). *Tectonophysics*, *223*(3–4), 339–362. https://doi.org/10.1016/0040-1951(93)90144-9

Caputo, R., Piscitelli, S., Oliveto, A., Rizzo, E., & Lapenna, V. (2003). The use of electrical resistivity tomographies in active tectonics: Examples from the Tyrnavos Basin, Greece. *Journal of Geodynamics*, *36*(1–2), 19–35. https://doi.org/10.1016/S0264-3707(03)00036-X

Cartwright, J. A., Mansfield, C., & Trudgill, B. (1996). The growth of normal faults by segment linkage. *Geological Society Special Publication*, *99*(99), 163–177. https://doi.org/10.1144/GSL.SP.1996.099.01.13

Chatzipetros, A., Pavlides, S., Foumelis, M., Sboras, S., Galanakis, D., Pikridas, C., Bitharis, S., Kremastas, E., Chatziioannou, A., & Papaioannou, I. (2021). The northern Thessaly strong earthquakes of March 3 and 4, 2021, and their neotectonic setting. *Bulletin of the Geological Society of Greece*, *58*, 222. https://doi.org/10.12681/bgsg.27225

Childs, C., Manzocchi, T., Walsh, J. J., Bonson, C. G., Nicol, A., & Schöpfer, M. P. J. (2009). A geometric model of fault zone and fault rock thickness variations. *Journal of Structural Geology*, *31*(2), 117–127. https://doi.org/10.1016/j.jsg.2008.08.009

Cowie, P. A., & Roberts, G. P. (2001). Constraining slip rates and spacings for active normal faults. *Journal of Structural Geology*, *23*(12), 1901–1915. https://doi.org/10.1016/S0191-8141(01)00036-0

De Novellis, V., Reale, D., Adinolfi, G. M., Sansosti, E., & Convertito, V. (2021). Geodetic model of the march 2021 thessaly seismic sequence inferred from seismological and insar data. *Remote Sensing*, *13*(17), 1–15. https://doi.org/10.3390/rs13173410

Dimitriou, D.; Giakoupis, P. (1998). *Mine Research of Coal Deposit in Elassona: Domeniko Sub-Area*.

Doutsos, T., Pe-Piper, G., Boronkay, K., & Koukouvelas, I. (1993). Kinematics of the Central Hellenides. *Tectonics*, *12*(4), 936–953.

Ferentinos, G., Georgiou, N., Christodoulou, D., Geraga, M., & Papatheodorou, G. (2018). Propagation and termination of a strike slip fault in an extensional domain: The westward growth of the North Anatolian Fault into the Aegean Sea. *Tectonophysics*, *745*(April), 183–195. https://doi.org/10.1016/j.tecto.2018.08.003

Floyd, M. A., Billiris, H., Paradissis, D., Veis, G., Avallone, A., Briole, P., McClusky, S., Nocquet, J. M., Palamartchouk, K., Parsons, B., & England, P. C. (2010). A new velocity field for Greece: Implications for the kinematics and dynamics of the

Aegean. *Journal of Geophysical Research: Solid Earth*, *115*(10), 1–25. https://doi.org/10.1029/2009JB007040

Galanakis, D., Sboras, S., Konstantopoulou, G., & Xenakis, M. (2021). Neogene-Quaternary tectonic regime and macroseismic observations in the Tyrnavos-Elassona broader epicentral area of the March 2021, intense earthquake sequence. *Bulletin of the Geological Society of Greece*, *58*(March), 200. https://doi.org/10.12681/bgsg.27196

Ganas, A., Valkaniotis, S., Briole, P., Serpetsidaki, A., Kapetanidis, V., Karasante, I., Kassaras, I., Papathanassiou, G., Karamitros, I., Tsironi, V., Elias, P., Sarhosis, V., Karakonstantis, A., Konstantakopoulou, E., Papadimitriou, P., & Sokos, E. (2021). Domino-style earthquakes along blind normal faults in Northern Thessaly (Greece): kinematic evidence from field observations, seismology, SAR interferometry and GNSS. *Bulletin of the Geological Society of Greece*, *58*(July), 37. https://doi.org/10.12681/bgsg.27102

Goldsworthy, M., Jackson, J., & Haines, J. (2002). The continuity of active fault systems in Greece. *Geophysical Journal International*, *148*(3), 596–618. https://doi.org/10.1046/j.1365-246X.2002.01609.x

Gutenberg, B., & Richter, C. F. (1945). Frequency of earthquakes in California. *Bulletin of the Geological Society of America*, *34*(4), 185–188. https://doi.org/10.1038/156371a0

Hack, J. T. (1973). Stream-profile analysis and Stream-gradient Index. *J.Res.Us Geol.Surv.*, *1*(4), 421–429.

Hack, J. T., & Young, R. S. (1959). Intreched Meanders of the North Fork of the Shenandoah River, Virginia. *United States Geological Survey Professional Paper*, *354*(A), 1–10.

Hanks, T. C., & Kanamori, H. (1979). A moment magnitude scale. *Journal of Geophysical Research*, *84*(B5), 2348. https://doi.org/10.1029/JB084iB05p02348

IG-NOA. (n.d.). *Earthquake catalogue archive*. Retrieved October 10, 2022, from http://bbnet.gein.noa.gr/HL/databases/database

Imber, J., Childs, C., Nell, P. A. R., Walsh, J. J., Hodgetts, D., & Flint, S. (2003). Hanging wall fault kinematics and footwall collapse in listric growth fault systems. *Journal of Structural Geology*, *25*(2), 197–208. https://doi.org/10.1016/S0191-8141(02)00034-2

Institute of Geology and Mineral Exploration. (1985a). *Geological Map of Greece, "Gonni" sheet, 1:50.000 scale*. IGME: Athens, Greece.

Institute of Geology and Mineral Exploration. (1985b). *Geological Map of Greece, "Larissa" sheet, 1:50.000 scale*. IGME: Athens, Greece.

Institute of Geology and Mineral Exploration. (1987). *Geological Map of Greece,*

"Elasson" sheet, 1:50.000 scale. IGME: Athens, Greece.

Institute of Geology and Mineral Exploration. (1998). *Geological Map of Greece, "Farkadon" sheet, 1:50.000 scale*. IGME: Athens, Greece.

Jolivet, L., & Brun, J. P. (2010). Cenozoic geodynamic evolution of the Aegean. *International Journal of Earth Sciences*, *99*(1), 109–138. https://doi.org/10.1007/s00531-008-0366-4

Karakostas, V., Papazachos, C., Papadimitriou, E., Foumelis, M., Kiratzi, A., Pikridas, C., Kostoglou, A., Kkallas, C., Chatzis, N., Bitharis, S., Chatzipetros, A., Fotiou, A., Ventouzi, C., Karagianni, E., Bonatis, P., Kourouklas, C., Paradisopoulou, P., Scordilis, E., Vamvakaris, D., … Galanis, O. (2021). The March 2021 Tyrnavos, central Greece, doublet (Mw6.3 and Mw6.0): Aftershock relocation, faulting details, coseismic slip and deformation. *Bulletin of the Geological Society of Greece*, *58*(March), 131. https://doi.org/10.12681/bgsg.27237

Kassaras, I., Kapetanidis, V., Ganas, A., Karakonstantis, A., Papadimitriou, P., Kaviris, G., Kouskouna, V., & Voulgaris, N. (2022). Seismotectonic analysis of the 2021 Damasi-Tyrnavos (Thessaly, Central Greece) earthquake sequence and implications on the stress field rotations. *Journal of Geodynamics*, *150*(January), 101898. https://doi.org/10.1016/j.jog.2022.101898

Kilias, A., Falalakis, G., Sfeikos, A., Papadimitriou, E., Vamvaka, A., & Gkarlaouni, C. (2013). The Thrace basin in the Rhodope province of NE Greece - A tertiary supradetachment basin and its geodynamic implications. *Tectonophysics*, *595–596*, 90–105. https://doi.org/10.1016/j.tecto.2012.05.008

Kilias, A., Fasoulas, C., Priniotakis, M., Sfeikos, A., & Frisch, W. (1991). Deformation and HP/LT Metamorphic Conditions at the Tectonic Window of Kranea (W -- Thessaly, Northern Greece). *Zeitschrift Der Deutschen Geologischen Gesellschaft*, *142*(1), 87–96. https://doi.org/10.1127/zdgg/142/1991/87

Kilias, A., Vamvaka, A., Falalakis, G., Sfeikos, A., Papadimitriou, E., Gkarlaouni, C., & Karakostas, B. (2017). The Mesohellenic trough and the Thrace Basin. Two Tertiary molassic Basins in Hellenides: do they really correlate? *Bulletin of the Geological Society of Greece*, *47*(2), 551. https://doi.org/10.12681/bgsg.11082

Kontoes, C. H., Alatza, S., Chousianitis, K., Svigkas, N., Loupasakis, C., Atzori, S., & Apostolakis, A. (2022). Coseismic Surface Deformation, Fault Modeling, and Coulomb Stress Changes of the March 2021 Thessaly, Greece, Earthquake Sequence Based on InSAR and GPS Data. *Seismological Research Letters*, *March 2021*. https://doi.org/10.1785/0220210112

Koukouvelas, I. K., Nikolakopoulos, K. G., Kyriou, A., Caputo, R., Belesis, A., Zygouri, V., Verroios, S., Apostolopoulos, D., & Tsentzos, I. (2021). The March 2021 damasi earthquake sequence, central Greece: reactivation evidence across the westward propagating tyrnavos graben. *Geosciences (Switzerland)*, *11*(8). https://doi.org/10.3390/geosciences11080328

Kourouklas, C., Console, R., Papadimitriou, E., Murru, M., & Karakostas, V. (2021). Strong Earthquakes Recurrence Times of the Southern Thessaly, Greece, Fault System: Insights from a Physics-Based Simulator Application. *Frontiers in Earth Science*, *9*(February), 1–17. https://doi.org/10.3389/feart.2021.596854

Lazos, I., Sboras, S., Chousianitis, K., Bitharis, S., Mouzakiotis, E., Karastathis, V., Pikridas, C., Fotiou, A., & Galanakis, D. (2021). Crustal deformation analysis of thessaly (Central greece) before the march 2021 earthquake sequence near elassona-tyrnavos (northern thessaly). *Acta Geodynamica et Geomaterialia*, *18*(3), 379–385. https://doi.org/10.13168/AGG.2021.0026

Legal Entity of Public Law Hellenic Cadastre. (2014). *Digital Elevation Model 2m Operational Programme Competitiveness 2007-13*. Entrepreneurship and Innovation 2014-2020 (EPAnEK). https://www.ktimanet.gr/

Li, Z., Xu, S.-S., & Ma, Z.-F. (2023). Space Geodetic Views on the 2021 Central Greece Earthquake Sequence: 2D Deformation Maps Decomposed from Multi-track and Multi-temporal Sentinel-1 InSAR Data. *IEEE Journal of Selected Topics in Applied Earth Observations and Remote Sensing*, *16*, 1–12. https://doi.org/10.1109/jstars.2023.3257234

Lifton, N. A., & Chase, C. G. (1992). Tectonic, climatic and lithologic influences on landscape fractal dimension and hypsometry: implications for landscape evolution in the San Gabriel Mountains, California. *Geomorphology*, *5*(1–2), 77–114. https://doi.org/10.1016/0169-555X(92)90059-W

Maggini, M., & Caputo, R. (2020). Sensitivity analysis for crustal rheological profiles: Examples from the Aegean region. *Annals of Geophysics*, *63*(3), 1–29. https://doi.org/10.4401/ag-8244

Makris, J., Papoulia, J., & Yegorova, T. (2013). A 3-D density model of greece constrained by gravity and seismic data. *Geophysical Journal International*, *194*(1), 1–17. https://doi.org/10.1093/gji/ggt059

McClay, K. R., Waltham, D. A., Scott, A. D., & Abousetta, A. (1991). Physical and seismic modelling of listric normal fault geometries. *Geological Society, London, Special Publications*, *56*(1), 231–239. https://doi.org/10.1144/GSL.SP.1991.056.01.16

Meissner, R., & Strehlau, J. (1982). Limits of stresses in continental crusts and their relation to the Depth-Frequency distribution of shallow earthquakes. *Tectonics*, *1*(1), 73–89.

Mercier, J. L., Sorel, D., Vergely, P., & Simeakis, K. (1989). Extensional tectonic regimes in the Aegean basins during the Cenozoic. *Basin Research*, *2*(1), 49–71. https://doi.org/10.1111/j.1365-2117.1989.tb00026.x

Michas, G., Pavlou, K., Avgerinou, S. E., Anyfadi, E. A., & Vallianatos, F. (2022). Aftershock patterns of the 2021 M w 6.3 Northern Thessaly (Greece) earthquake.

Journal of Seismology, *26*(2), 201–225. https://doi.org/10.1007/s10950-021-10070-9

Migiros, G., Bathrellos, G. D., Skilodimou, H. D., & Karamousalis, T. (2011). Pinios (Peneus) River (Central Greece): Hydrological - Geomorphological elements and changes during the quaternary. *Central European Journal of Geosciences*, *3*(2), 215–228. https://doi.org/10.2478/s13533-011-0019-1

Mountrakis, D. (1986). The Pelagonian zone in Greece: a polyphase-deformed fragment of the Cimmerian continent and its role in the geotectonic evolution of the eastern Mediterranean. *Journal of Geology*, *94*(3), 335–347. https://doi.org/10.1086/629033

Mouslopoulou, V., Sudhaus, H., Konstantinou, K. I., Begg, J., Saltogianni, V., Männel, B., Andinisari, R., & Oncken, O. (2022). A deeper look into the 2021 Tyrnavos Earthquake Sequence (TES) reveals coseismic breaching of an unrecognised large-scale fault relay zone in continental Greece. *Tectonics*. https://doi.org/10.1029/2022TC007453

Nicol, A., Walsh, J., Childs, C., & Manzocchi, T. (2020). The growth of faults. In *Understanding Faults* (pp. 221–255). Elsevier. https://doi.org/10.1016/B978-0-12-815985-9.00006-0

Papaioannou, I. (2021). 1735 and 1901: Two strong earthquakes from the same seismogenic area. *Eleftheria [In Greek]*.

Papathanassiou, G., Valkaniotis, S., Ganas, A., Stampolidis, A., Rapti, D., & Caputo, R. (2022). Floodplain evolution and its influence on liquefaction clustering : The case study of March 2021 Thessaly , Greece , seismic sequence. *Engineering Geology*, *298*(January), 106542. https://doi.org/10.1016/j.enggeo.2022.106542

Papazachos, B. C., & Papazachou, C. (2003). *The earthquakes of Greece*. Ziti publications [In Greek].

Papazachos, C. (1993). Determination of crustal thickness by inversion of travel times: An application in the Aegean area. *2nd Cong. Hell. Geophys. Union*, 483–491.

Pavlides, S., & Caputo, R. (2004). Magnitude versus faults' surface parameters: Quantitative relationships from the Aegean Region. *Tectonophysics*, *380*(3–4), 159–188. https://doi.org/10.1016/j.tecto.2003.09.019

Pavlides, S., Chatzipetros, A., Sboras, S., Kremastas, E., & Chatziioannou, A. (2021). *The northern Thessaly strong earthquakes of March 3 and 4 and their neotectonic setting*. https://doi.org/10.5281/ZENODO.4618188

Pavlides, S., & Sboras, S. (2021). Recent earthquake activity of March 2021 in northern Thessaly unlocks new scepticism on Faults. *TURKISH JOURNAL OF EARTH SCIENCES*, *30*(SI-1), 851–861. https://doi.org/10.3906/yer-2110-6

Pazzaglia, F. L., Gardner, T. W., & Merritts, D. J. (1998). Bedrock fluvial incision and longitudinal profile development over geologic time scales determined by fluvial terraces. In K. J. Tinkler & E. E. Wohl (Eds.), *Rivers over rock: Fluvial processes in*

bedrock channels (p. 323). American Geophysical Union.

Peacock, D. C. P., Knipe, R. J., & Sanderson, D. J. (2000). Glossary of normal faults. *Journal of Structural Geology*, *22*(3), 291–305. https://doi.org/10.1016/S0191-8141(00)80102-9

Pérouse, E., Chamot-Rooke, N., Rabaute, A., Briole, P., Jouanne, F., Georgiev, I., & Dimitrov, D. (2012). Bridging onshore and offshore present-day kinematics of central and eastern Mediterranean: Implications for crustal dynamics and mantle flow. In *Geochemistry, Geophysics, Geosystems* (Vol. 13, Issue 9). https://doi.org/10.1029/2012GC004289

Psilovikos, A., Mountrakis, D., & Pavlides, S. (1989). Morphological and structural correlations in the area of Pelagonian block. *Bull. Geol. Soc. Greece*, *XXIII*(1), 271–278.

Roche, V., Bouchot, V., Beccaletto, L., Jolivet, L., Guillou-Frottier, L., Tuduri, J., Bozkurt, E., Oguz, K., & Tokay, B. (2019). Structural, lithological, and geodynamic controls on geothermal activity in the Menderes geothermal Province (Western Anatolia, Turkey). *International Journal of Earth Sciences*, *108*(1), 301–328. https://doi.org/10.1007/s00531-018-1655-1

Roche, V., Camanni, G., Childs, C., Manzocchi, T., Walsh, J., Conneally, J., Saqab, M. M., & Delogkos, E. (2021). Variability in the three-dimensional geometry of segmented normal fault surfaces. *Earth-Science Reviews*, *216*(January), 103523. https://doi.org/10.1016/j.earscirev.2021.103523

Sboras, S., Chatzipetros, A., & Pavlides, S. B. (2017). *North Aegean Active Fault Pattern and the 24 May 2014, M w 6.9 Earthquake . May 2014*, 239–272. https://doi.org/10.1002/9781118944998.ch9

Sboras, S., Pavlides, S., Kilias, A., Galanakis, D., Chatziioannou, A., & Chatzipetros, A. (2022). The Geological Structure and Tectonic Complexity of Northern Thessaly That Hosted the March 2021 Seismic Crisis. *Geotechnics*, *2*(4), 935–960. https://doi.org/10.3390/geotechnics2040044

Schermer, E. R. (1993). Geometry and kinematics of continental basement deformation during the Alpine orogeny, Mt. Olympos region, Greece. *Journal of Structural Geology*, *15*(3–5), 571–591. https://doi.org/10.1016/0191-8141(93)90149-5

Schwartz, D. P., & Coppersmith, K. J. (1984). Fault behavior and characteristic earthquakes: examples from the Wasatch and San Andreas fault zones (USA). *Journal of Geophysical Research*, *89*(B7), 5681–5698. https://doi.org/10.1029/JB089iB07p05681

Sfeikos, A., Bohringer, C., Frisch, W., Kilias, A., & Ratschbacher, L. (1990). Kinematics of Pelagonian nappes in the Kranea area (North Thessaly, Greece). *Bulletin of the Geological Society of Greece*, *XXV*(1), 101–114.

Stucchi, M., Rovida, A., Gomez Capera, A. A., Alexandre, P., Camelbeeck, T., Demircioglu, M. B., Gasperini, P., Kouskouna, V., Musson, R. M. W., Radulian, M., Sesetyan, K., Vilanova, S., Baumont, D., Bungum, H., Fäh, D., Lenhardt, W., Makropoulos, K., Martinez Solares, J. M., Scotti, O., … Giardini, D. (2013). The SHARE European Earthquake Catalogue (SHEEC) 1000–1899. *Journal of Seismology*, *17*(2), 523–544. https://doi.org/10.1007/s10950-012-9335-2

Tolomei, C., Caputo, R., Polcari, M., Famiglietti, N. A., Maggini, M., & Stramondo, S. (2021). The use of interferometric synthetic aperture radar for isolating the contribution of major shocks: The case of the march 2021 thessaly, greece, seismic sequence. *Geosciences (Switzerland)*, *11*(5). https://doi.org/10.3390/geosciences11050191

Troiani, F., & Della Seta, M. (2008). The use of the Stream Length–Gradient index in morphotectonic analysis of small catchments: A case study from Central Italy. *Geomorphology*, *102*(1), 159–168. https://doi.org/10.1016/j.geomorph.2007.06.020

Valkaniotis, S., Papathanassiou, G., Ganas, A., Kremastas, E., & Caputo, R. (2021). *Preliminary report of liquefaction phenomena triggered by the March 2021 earthquakes in Central Thessaly , Greece*. *March*. https://doi.org/10.5281/zenodo.4608365

Vamvaka A, K. A. (2015). The Mesohellenic Trough and the Paleogene Thrace Basin on the Rhodope Massif, their Structural Evolution and Geotectonic Significance in the Hellenides. *Journal of Geology & Geosciences*, *04*(02). https://doi.org/10.4172/2329-6755.1000198

Walcott, C. (1998). The alpine evolution of Thessaly (NW Greece) and late Tertiary Aegean kinematics. In *Geologica Ultraiectina*. http://igitur-archive.library.uu.nl/geo/2013-0417-200717/UUindex.html

Walsh, J. J., Bailey, W. R., Childs, C., Nicol, A., & Bonson, C. G. (2003). Formation of segmented normal faults: A 3-D perspective. *Journal of Structural Geology*, *25*(8), 1251–1262. https://doi.org/10.1016/S0191-8141(02)00161-X

Williams, G., & Vann, I. (1987). The geometry of listric normal faults and deformation in their hangingwalls. *Journal of Structural Geology*, *9*(7), 789–795. https://doi.org/10.1016/0191-8141(87)90080-0

Wortel, M. J. R., & Spakman, W. (2000). Subduction and slab detachment in the Mediterranean-Carpathian region. *Science*, *290*(5498), 1910–1917. https://doi.org/10.1126/science.290.5498.1910

Yang, J., Xu, C., Wen, Y., & Xu, G. (2022). Complex Coseismic and Postseismic Faulting During the 2021 Northern Thessaly (Greece) Earthquake Sequence Illuminated by InSAR Observations. *Geophysical Research Letters*, *49*(8), 1–10. https://doi.org/10.1029/2022gl098545

Εκτεταμένη περίληψη (Extended abstract in Greek)

Η σεισμική ακολουθία της Βόρειας Θεσσαλίας του 2021 άλλαξε τον τρόπο που αντιμετωπίζουμε τα «κρυφά» ή «τυφλά» ρήγματα ως προς την επικινδυνότητά τους. Η ακολουθία αποτελείται από τρεις κύριους σεισμούς μεγέθους M_w6.3, M_w6.0 και M_w5.6 που έλαβαν χώρα στις 3, 4 και 12 Μαρτίου, αντίστοιχα. Σοβαρές καταστροφές καταγράφηκαν στα χωριά της περιοχής γύρω από τα επίκεντρα, καθώς και μία έμμεση απώλεια ζωής. Παρόλα αυτά, η ακολουθία είναι εξαιρετικής σημασίας διότι αναδεικνύει ιδιαίτερα χαρακτηριστικά της γεωλογίας και τεκτονικής της ευρύτερης περιοχής.

Η παρούσα εργασία στοχεύει στην προσομοίωση της ρηξιγενούς ζώνης του Ζάρκου, του «κρυφού» ρήγματος που ενεργοποιήθηκε το Μάρτιο του 2021. Βάσει των InSAR εικόνων, το ίχνος του ρήγματος τοποθετείται στα βουνά του Ζάρκου, εντός του Πελαγονικού καλύμματος, το οποίο αποτελείται από Τριαδικοϊουρασικούς ανακρυσταλλωμένους ασβεστολίθους και εναλλαγές Παλαιοζωικών γνευσίων-σχιστολίθων με εμφανή σημάδια των Αλπικών παραμορφωτικών φάσεων. Με την κατάρρευση του ορογενούς ξεκινά ο εφελκυσμός με διεύθυνση ΒΑ-ΝΔ κατά το Πλειόκαινο-Κ. Πλειστόκαινο ο οποίος σχετίζεται μεταξύ άλλων με ρήγματα της ρηξιγενούς ζώνης του Ζάρκου, ενώ η σημερινή ενεργός διεύθυνσή του είναι Β-Ν και σχετίζεται με τη δημιουργία των δομών παράταξης Α-Δ. Στο άνω τέμαχος του ρήγματος του Ζάρκου, εξαιτίας της δράσης μικρών κανονικών ρηγμάτων, έχει αναπτυχθεί η στενή κοιλάδα του Τιταρίσιου ποταμού στην οποία έχουν αποτεθεί ιζήματα Νεογενούς-Τεταρτογενούς ηλικίας.

Το τριδιάστατο μοντέλο που παρουσιάζεται στην παρούσα εργασία αποτελείται από 4 συνθετικές επιφάνειες με συνολικό μήκος 33.5χλμ, μέγιστο βάθος περί τα 13χλμ και μέση κλίση ~55^o προς ΒΑ, ενώ η κλίση της κύριας επιφάνειας υπολογίζεται σε ~50^o. Η προσομοίωση είναι προϊόν συνδιαστικής ανάλυσης των σεισμικών εστιών του σεισμικού καταλόγου από την εργασία Kassaras et al. (2022) και τους δισδιάστατου μοντέλου που επίσης παρουσιάζεται στην εργασία. Το μοντέλο αυτό βασίζεται κατά κύριο λόγο στις InSAR εικόνες, οι οποίες συσχετίζονται με τη γεωλογία και γεωμορφολογία της περιοχής μελέτης.

Η σεισμική ακολουθία χαρακτηρίζεται από αμφίδρομη εξάπλωση των εστιών πάνω στη ρηξιγενή ζώνη του Ζάρκου, με τους δύο κύριος να λαμβάνουν χώρα πάνω στην «κύρια» επιφάνεια, ενώ 3 ακόμα συνθετικές επιφάνειες ενεργοποιούνται στα άκρα της, ΒΔ και ΝΑ. Για τη βέλτιστη μελέτη της χωροχρονικής εξέλιξης της ακολουθίας και τη συσχέτισή της με το τρισδιάστατο μοντέλο, οι σεισμικές εστίες προβάλλονται πάνω στη μέση ορθογώνια επιφάνεια της ρηξιγενούς ζώνης και κατασκευάζονται ισόχρονες καμπύλες.

Σημαντικό μέρος της εργασίας αποτελεί η ανάλυση του τρισδιάστατου μοντέλου της ρηξιγενούς ζώνης του Ζάρκου ως προς την ορθότητά του, συγκρίνοντάς του με παραδείγματα από τη βιβλιογραφία, καθώς και με τα άλλα μοντέλα που έχουν προταθεί για την ίδια ακολουθία. Το μοντέλο που παρουσιάζεται σε αυτήν την εργασία φαίνεται

να επιβεβαιώνει τις θεωρίες για την ενεργοποίηση «τυφλού» ή «κρυφού» χαμηλής γωνίας ρήγματος, το οποίο υπόκειται των κύριων ενεργών ρηγμάτων της περιοχής τα οποία και ενεργοποιήθηκαν δευτερευόντως το Μάρτιο του 2021. Ακόμη, βρίσκεται σε γενική συμφωνία με τα υπόλοιπα μοντέλα και κυρίως αυτά που βασίζονται στον ίδιο σεισμικό κατάλογο, με βασική διαφοροποίηση τη διεύθυνση κλίσης της επιφάνειας που αντιστοιχεί στον 3ο σεισμό της 12ης Μαρτίου (M_w5.6) και στα περισσότερα παρουσιάζεται ως αντιθετική.

Παρά την πολυπλοκότητα και τις συνεχείς απότομες αλληλεπιδράσεις των επιφανειών της ρηξιγενούς ζώνης του Ζάρκου, η σεισμική ακολουθία της Βόρειας Θεσσαλίας του 2021 επισημαίνει τον σημαντικό ρόλο των κληροδοτούμενων από παλαιότερα τεκτονικά καθεστώτα δομών, τα οποία θεωρούνται ανενεργά. Η ανάπτυξη των ρηγμάτων αποτελεί μία διαρκή φυσική διαδικασία, η οποία μπορεί να οδηγήσει στη δημιουργία πολύπλοκων ρηξιγενών συστημάτων. Αυτά μπορεί να αποτελούνται από ρήγματα διαφορετικών παραμορφωτικών φάσεων που όμως είναι ικανά να προκαλέσουν ισχυρούς σεισμούς, όπως συνέβη το Μάρτιου του 2021 στη Βόρεια Θεσσαλία. Η καλύτερη κατανόηση αυτών των συστημάτων, τα οποία ενδεχομένως να είναι «τυφλά», «κρυφά» ή αχαρτογράφητα είναι εξαιρετικά σημαντική για τη μελέτη της σεισμικής επικινδυνότητας.